UNIVERSITY OF CALIFORNIA,
IRVINE

Advancing our Molecular Level Understanding of SOA Particle Growth through Incorporation of Molecular Probes

DISSERTATION

submitted in partial satisfaction of the requirements
for the degree of

DOCTOR OF PHILOSOPHY

in Chemistry

by

Allison Claire Vander Wall

Dissertation Committee:
Professor Barbara J. Finlayson-Pitts, Chair
Professor Sergey A. Nizkorodov
Associate Professor Craig Murray

2020

DEDICATION

To my husband, Will, for his continued support and love.

To my parents, grandparents, brothers, and sisters, for setting great examples and always pushing me to work harder.

TABLE OF CONTENTS

LIST OF FIGURES

LIST OF TABLES

ACKNOWLEDGMENTS

To my husband, Will, thank you for your patience and support through all the hurdles life has thrown our way. I couldn't have asked for a better partner.

To my parents, Eric and Jackie, thank you for instilling in me the value of education and for always pushing me reach higher. To my grandfather, Ben, thank you for always having words of encouragement no matter the situation.

Professor Finlayson-Pitts, thank you for being a wonderful mentor and role model. I've learned so much from you both inside and outside the lab, and I will always appreciate the time and energy you've invested in helping me grow as a researcher, as a chemist, and as a person.

Thank you to my committee members, Professor Nizkorodov and Professor Murray. Over the years you've provided helpful and fun discussions about both research and life.

To the Finlayson-Pitts group both past and present, it's been wonderful to spend my graduate school years with you! Mike Ezell and Dr. Weihong Wang, thank you for your helpful input and fun conversations over lunch, at group meeting, and in the office. Thank you especially to Dr. Véronique Perraud and Dr. Lisa Wingen for always making time for me whether it be for research discussions, experiments, or paper drafts. To Dr. Kristine Arquero, Dr. Michelle Fairhurst, and Andrea Rohrbacher, thank you for sharing the graduate student experience with me; it was an honor sharing the office with such stellar women in science!

I've made many friends at UC Irvine who have shared the experience with and encouraged me. Thank you especially to Dr. Kara Kapnas for always listening and laughing with me throughout the process.

CURRICULUM VITAE

Education

Ph.D., Chemistry, University of California, Irvine 2020
Advisor: Professor Barbara J. Finlayson-Pitts

M.S., Chemistry, University of California, Irvine 2016
GPA: 3.81

B.S., Chemistry, Westmont College, 2013
GPA: 3.78
Major Honors, Magna Cum Laude
Adam's Music Scholar, Provost's Scholar

Research Experience

University of California, Irvine 2014-2020
Advisor: Barbara Finlayson-Pitts
Researched and quantified kinetic and thermodynamic parameters for the interactions of gaseous species with secondary organic aerosol particles to probe mechanisms of particle growth in the atmosphere.

Westmont College 2011-2013
Advisor: Michael Everest
Studied the spatial sensitivity and time dependence of Evanescent-Wave Cavity Ring-Down Spectroscopy and Ellipsometry as a tool for examining chemical kinetics.

Teaching Experience

University of California, Irvine 2014-2020
General Chemistry Lab Teaching Assistant, General Chemistry Lecture Discussion Teaching Assistant, Environmental Chemistry Lecture Teaching Assistant

Westmont College 2012-2013
Student Grader and Teaching Assistant, Physical Chemistry Lab Teaching Assistant

Publications

A. C. Vander Wall, L. M. Wingen, V. Perraud, Y. Zhao, B. J. Finlayson-Pitts. "Further Evidence for an Additional Kinetically-Controlled Mechanism for Secondary Organic Aerosol Particle Growth". *Publication in preparation*

A. C. Vander Wall, L. M. Wingen, V. Perraud, B. J. Finlayson-Pitts. "Evidence for a Kinetically Controlled Burying Mechanism for Growth of High Viscosity Secondary Organic Aerosol". *Environmental Science: Processes and Impacts,* 2020, 22, 66-83. DOI: 10.1039/C9EM00379G
Issue cover art, and designated 'hot article' by the journal

A. C. Vander Wall, P. S. J. Lakey, E. Rossich-Molina, V. Perraud, L. M. Wingen, J. Xu, D. Soulsby, R. B. Gerber, M. Shiraiwa, and B. J. Finlayson-Pitts. "Understanding Interactions of Organic Nitrates with the Surface and Bulk of Organic Films: Implications for Particle Growth in the Atmosphere". *Environmental Science: Processes and Impacts,* 2018, 20, 1593-1610. DOI: 10.1039/C8EM00348C
Part of a themed collection: Atmospheric Surfaces

Oral Presentations

A. C. Vander Wall and B. J. Finlayson-Pitts. "Advancing our Understanding of SOA Particles through the Incorporation of Organic Nitrates as Molecular Probes"

- November 2019 – AirUCI Seminar, Irvine, CA
- November 2019 – Westmont College Research Seminar, Santa Barbara, CA

A. C. Vander Wall, P. S. J. Lakey, E. R. Molina, V. Perraud, J. Xu, L. M. Wingen, D. Soulsby, M. Shiraiwa, R. B. Gerber, B. J. Finlayson-Pitts. "Understanding Interactions of Organic Nitrates with the Surface and Bulk of Organic Films: Implications for Particle Growth in the Atmosphere"

- September 2018 – AirUCI Research Workshop, Lake Arrowhead, CA

A. C. Vander Wall, V. Perraud, J. Xu, L. M. Wingen, P. S. J. Lakey, E. R. Molina, M. Shiraiwa, R. B. Gerber, D. Soulsby, B. J. Finlayson-Pitts. "Mechanisms Governing the Incorporation of Organic Nitrates into Secondary Organic Aerosol Particles: Atmospheric Implications"

- March 2018 – University of California Chemical Symposium, Lake Arrowhead, CA

A. C. Vander Wall, V. Perraud, L. M. Wingen, J. Xu, R. B. Gerber, B. J. Finlayson-Pitts. "Laboratory Studies of the Uptake and Incorporation of Tracer Compounds into Secondary Organic Aerosol Particles as a Mechanistic Probe for Particle Growth"

- December 2017 – American Geophysical Union Fall Meeting, New Orleans, LA

Poster Presentations

A. C. Vander Wall, V. Perraud, L. M. Wingen, B. J. Finlayson-Pitts. "Incorporation of Tracers into Secondary Organic Aerosol Indicates a Kinetically Controlled Burying Mechanism"

- December 2019 – American Geophysical Union Fall Meeting, San Francisco, CA

A. C. Vander Wall, V. Perraud, L. M. Wingen, B. J. Finlayson-Pitts. "Investigating particle growth and organic nitrate uptake into secondary organic aerosol particles from the ozonolysis of α-pinene"

- August 2019 – American Chemical Society Fall Meeting, San Diego, CA

A. C. Vander Wall, V. Perraud, L. M. Wingen, B. J. Finlayson-Pitts. "Organic Nitrate Uptake into Secondary Organic Aerosol Particles from the Ozonolysis of α-pinene and Implications for Particle Growth"

- May 2019 – 36th Informal Symposium on Kinetics and Photochemical Processes in the Atmosphere, Pasadena, CA

A. C. Vander Wall, P. S. J. Lakey, E. Rossich-Molina, V. Perraud, L. M. Wingen, J. Xu, D. Soulsby, R. B. Gerber, M. Shiraiwa, and B. J. Finlayson-Pitts. "Understanding Particle Growth by Examining the Interactions of Organic Nitrates with Organic Substrates"

- December 2018 – American Geophysical Union Fall Meeting, Washington, D.C.

A. C. Vander Wall, V. Perraud, J. Xu, L. M. Wingen, P. S. J. Lakey, E. R. Molina, M. Shiraiwa, R. B. Gerber, D. Soulsby, B. J. Finlayson-Pitts. "Mechanisms Governing the Incorporation of Organic Nitrates into Secondary Organic Aerosol Particles"

- March 2018 – 35th Informal Symposium on Kinetics and Photochemical Processes in the Atmosphere, Pasadena, CA

A. C. Vander Wall, V. Perraud, L. M. Wingen, J. Xu, R. B. Gerber, B. J. Finlayson-Pitts. "Experimental Approaches to Elucidating Mechanisms of SOA Particle Growth"

- May 2017 – 34th Informal Symposium on Kinetics and Photochemical Processes in the

Atmosphere, San Diego, CA

A. C. Vander Wall, V. Perraud, B. J. Finlayson-Pitts. "Uptake of Tracer Compounds into SOA formed by the Ozonolysis of α-Pinene"

- March 2016 – American Chemical Society National Meeting, San Diego, CA
- March 2016 – 33rd Informal Symposium on Kinetics and Photochemical Processes in the Atmosphere, Irvine, CA

A. C. Vander Wall, V. Perraud, B. J. Finlayson-Pitts. "Incorporation of 2-Ethylhexyl Nitrate into SOA from the Ozonolysis of α-Pinene – Examining Mechanisms of Particle Growth"

- April 2015 – 32rd Informal Symposium on Kinetics and Photochemical Processes in the Atmosphere, Northridge, CA

A. C. Vander Wall, C. Berchiolli, M. A. Everest. "Spatial Sensitivity and Time Dependence of Evanescent-Wave Cavity Ring-Down Spectroscopy"

- November 2012 – Southern California Conferences for Undergraduate Research. Camarillo, CA

Community Outreach

University High School, Irvine, CA 2019

- Developed and presented atmospheric chemistry demonstrations to local high school chemistry and environmental science students.

United Cerebral Palsy of Orange County 2017-2018

- Developed age-appropriate activities with members of Iota Sigma Pi to teach children about chemistry using hands-on experiments and demonstrations during hour-long classes, each class and the corresponding activities themed for a specific topic related to chemistry.

Tech Trek UCI 2016-2019

- Coordinated and led tours of the research lab and chemistry demonstrations during the annual Tech Trek summer science and math camp at UCI, aimed at encouraging young women entering 8th grade to pursue their interests in STEM.

American Chemical Society Science Day 2014-2017

- Organized "Science Day" at the Santa Ana Zoo with members of Iota Sigma Pi during National Chemistry Week, performing hands-on science activities and demonstrations geared towards K-12 children.

Lab Tour Guide 2017

- Presented lab tours for high school teachers and their students as part of an NSF-funded 'Teacher-in-Residence' program through the group of Professor Craig Murray at UCI.

Professional Memberships and Activities

Iota Sigma Pi – National Honors Society for Women in Chemistry 2015-present
Vice President, Iota Sigma Pi, Calcium Chapter June 2016-June 2017
American Chemical Society 2015-present
American Geophysical Union 2017-present

PUBLICATIONS

A. C. Vander Wall, P. S. J. Lakey, E. Rossich-Molina, V. Perraud, L. M. Wingen, J. Xu, D. Soulsby, R. B. Gerber, M. Shiraiwa, and B. J. Finlayson-Pitts. "Understanding Interactions of Organic Nitrates with the Surface and Bulk of Organic Films: Implications for Particle Growth in the Atmosphere". *Environmental Science: Processes and Impacts,* 2018, 20, 1593-1610.
DOI: 10.1039/C8EM00348C

A. C. Vander Wall, V. Perraud, L. M. Wingen, and B. J. Finlayson-Pitts. "Evidence for a Kinetically Controlled Burying Mechanism for Growth of High Viscosity Secondary Organic Aerosol ". *Environmental Science: Processes and Impacts,* 2020, 22, 66-83.
DOI: 10.1039/C9EM00379G

ABSTRACT OF THE DISSERTATION

Advancing our Molecular Level Understanding of SOA Growth through Incorporation of Organic Nitrates

By

Allison Claire Vander Wall

Doctor of Philosophy in Chemistry

University of California, Irvine, 2018

Professor Barbara J. Finlayson-Pitts, Chair

Secondary organic aerosol (SOA) makes up a substantial portion of airborne particles. SOA particles are known to significantly impact air quality and climate, and to severely and negatively impact health. A comprehensive understanding of physical and chemical processes governing particle formation and growth is needed to accurately predict particle effects.

This thesis examines growth processes of organic particles by quantifying the incorporation of molecular probes (or tracers) into SOA particles from the ozonolysis of α-pinene, prepared both with and without cyclohexane as an OH radical scavenger. The incorporation into model organic solids with varying polarity and functionalities is also examined. The tracers serve to probe properties such as (1) initial surface interactions occurring between the gas and solid phase, (2) magnitude of the partitioning of gases into particles or solid films, and (3) diffusivity changes during uptake and evaporation. This work focuses predominantly on three gaseous organic nitrates ($RONO_2$, 2-ethylhexyl nitrate, β-hydroxyhexyl

nitrate, and β-hydroxypropyl nitrate) as tracers, with some experiments using two gas phase organic nitriles (nonanenitrile and valeronitrile) for comparison.

The first approach used attenuated total reflectance (ATR) FTIR to quantify initial uptake coefficients and bulk partition coefficients into thin films of triacontane (TC), cis-pinonic acid (PA), poly(ethylene adipate) di-hydroxy terminated (PEA), and impacted SOA particles both with and without an OH scavenger. The gas phase tracer was introduced over the thin films in a flow of clean dry air. The characteristic IR peaks of the organic nitrates were followed over time until equilibrium was established. There was no measurable uptake onto TC for all of the organic nitrates, but uptake into films of PA, PEA and SOA was significant. The subsequent desorption by flowing clean air over the film showed the uptake was reversible and non-reactive. Quantum chemical calculations provided binding energies and insight into the intermolecular interactions involved in uptake. Kinetic modeling of the diffusion throughout the films showed that the $RONO_2$ acted as a plasticizer, with the diffusion coefficients increasing as more $RONO_2$ was taken up. Upon desorption of the $RONO_2$ from the surface layer, a 'crusting' effect was observed, hindering the diffusion from the underlying layers. These studies demonstrate how uptake and evaporation of gases can lead to varying viscosity throughout particles.

The second approach followed the incorporation of the tracers in the flow reactor *during* particle formation and growth. The incorporation was quantified using ATR-FTIR and high resolution time-of-flight aerosol mass spectrometry. The precursor concentrations were varied to examine how the particle diameter and organic mass loading affect the incorporation of the organic nitrates. The amount of a given $RONO_2$ taken up into the particles relative to its gas

phase concentration within the flow reactor was larger than the amount taken up into the thin films. The results of these studies indicate that simultaneous incorporation of $RONO_2$ and low volatility ozonolysis products into highly viscous particles may result in gas partitioning that is in excess of that expected for equilibrium partitioning. This supports a new mechanism of particle growth in the atmosphere, an irreversible "burying mechanism". These two systems show that growth of organic particles in air may not always be predicted via equilibrium considerations.

Chapter 1: Introduction

1.1 Organic Aerosol Particles in the Atmosphere

Atmospheric aerosols are comprised of a suspension of solid or liquid particulate matter in the surrounding gas in the atmosphere. Aerosol particles are divided into categories based on their size: 1) coarse particles, defined as particles with an aerodynamic diameter greater than 2.5 μm, 2) fine particles, with an aerodynamic less than or equal to 2.5 μm, and 3) ultrafine particles, typically defined as particles with an aerodynamic diameter less than 0.1 μm.[1-4] These particles are of great importance as they have been shown to have adverse effects on human health. Inhalation of these particles has been linked to negative cardiovascular, respiratory, and pulmonary health outcomes.[3-9]

Atmospheric particles have also been shown to impact climate. Once these particles achieve a sufficient size (~50-100 nm diameter), they can reduce visibility and affect climate through their ability to absorb and scatter solar radiation, directly altering the radiative balance of Earth's atmosphere.[1, 10-11] Depending on their chemical composition and thus their hygroscopicity, these particles can also affect climate indirectly by acting as nuclei onto which water can condense to form cloud droplets.[12-13] Both of these effects result in a net cooling of the Earth's surface through negative radiative forcing, although the uncertainties are large due to the lack of understanding of these processes and their link to particle size, composition, and concentrations (Figure 1.1).[14]

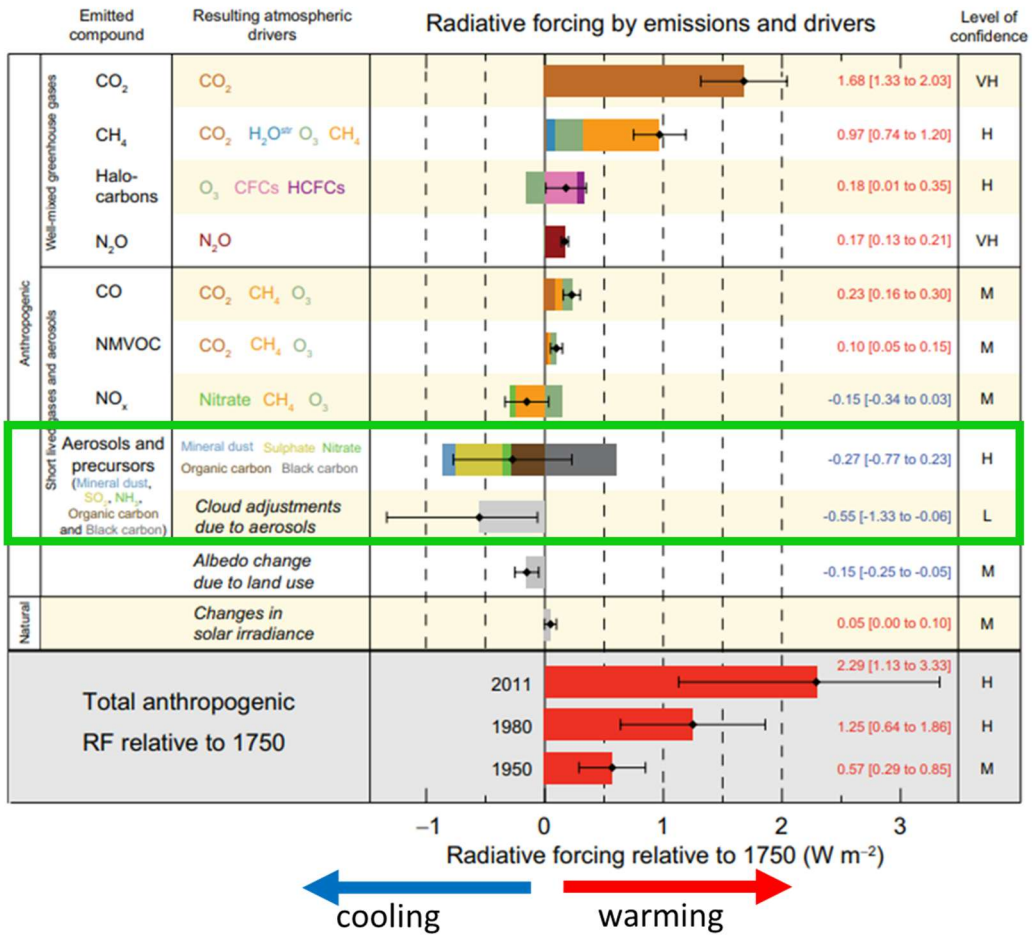

Figure 1.1: Radiative forcing (W•m^{-2}) for atmospheric species, relative to the year 1750. The green box highlights the contribution from aerosols. Figure adapted from Figure SPM.5 in IPCC, 2013: Summary for Policymakers.[14]

Inorganic species are a major component of atmospheric particulate matter. However, the particle composition can be dominated by organics in some regions, leading to organic mass contributing between 20-90% of the total mass of submicron aerosol particles.[15-20] Ambient organic aerosols can be divided into two categories based on their sources. Primary organic aerosol (POA) particles are emitted directly into the atmosphere from various sources including both anthropogenic such as mechanical processes or biomass burning, as well as biogenic sources which can be emitted from processes in Earth's biosphere.[21-26] Secondary organic

aerosol (SOA) particles are formed in the atmosphere from gas-phase or multi-phase chemistry. Volatile organic compounds (VOCs) emitted into the atmosphere from either anthropogenic or biogenic sources are oxidized by atmospheric oxidants such as OH radical, O_3, and oxides of nitrogen. This oxidation results in lower volatility products that can then contribute to SOA particles by either nucleating new particles or condensing onto existing particles to contribute to the particle growth process.[27-30]

The VOC precursors for SOA have many sources, the majority of which are biogenic.[31] A large fraction of these biogenic VOCs belong to a class of compounds called terpenes, consisting of unsaturated hydrocarbons whose structures are comprised of isoprene units.[32-34] Figure 1.2 shows the structure of α-pinene, one of the most abundant monoterpenes.[35-36] Other monoterpenes have the same formula ($C_{10}H_{16}$) and include *β*-pinene, Δ^3-carene, *d*-limonene, camphene, myrcene, and others.[35, 37-38]

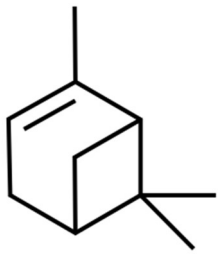

Figure 1.2: The structure of α-pinene.

1.2 Particle Phase State and Mechanisms of Particle Growth

The incorporation of gases into a particle or droplet (in the absence of any chemical reaction) involves several steps including diffusion through the gas phase to the surface, adsorption at the surface and mass accommodation, and diffusion through and incorporation into the bulk.[39-41] Figure 1.3 shows a simple schematic of these steps.

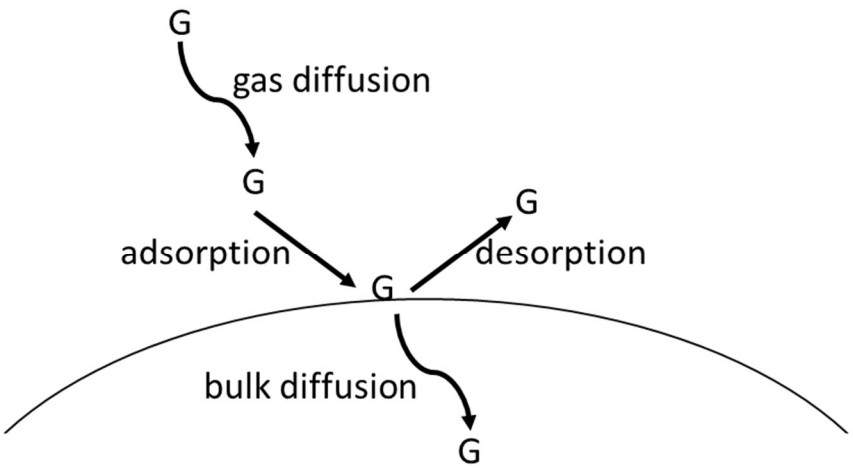

Figure 1.3: A simple schematic of the steps involved in how a gaseous species (G) interacts with a particle or droplet in the absence of any chemical reaction.

The phase of atmospheric particles has important implications for the mechanisms by which gases interact with the particles and contribute to the particle growth process. For a liquid droplet, a thermodynamically-driven quasi-equilibrium can rapidly be established between the particle phase and the surrounding gas phase.[30, 42-47] In this scenario, diffusion throughout a liquid droplet can be rapid, and thus mixing times will be fast (on the order of seconds or less), and these droplets can be well-mixed or homogeneous in nature.

Many studies have shown that under some conditions, SOA can exist not as a low viscosity liquid but rather as a high viscosity semi-solid or glassy state.[48-70] A study by Shiraiwa *et al.*[71] showed that the majority of SOA particles in the troposphere around the globe will exist in a semi-solid or solid phase state. In this case, the interactions of gases with the particle phase will occur on a slower timescale and will instead be driven by a kinetically limited, diffusion-controlled mechanism. Zaveri *et al.*[72] showed that both the growth and evaporation kinetics of

bimodal SOA particles were best reproduced by a semi-solid scenario. A study by Riipinen *et al*.[73] was able to reproduce particle formation and growth measured in Hyytiälä, Finland when the model included a kinetic condensation mechanism. Additionally, when modelling the dynamics of SOA formation and growth, Wang *et al.*[74] found that a number of kinetic processes that occur simultaneously should be taken into account, rather than assuming a quasi-equilibrium approach.

For highly viscous organic particles, these diffusion limitations can potentially result in a non-uniform or heterogeneous composition. Different molecules or functionalities at the surface of the particle compared to the bulk will affect the interactions of gases with the surface of the particles, and thus particle growth.[75-78] A study by Denjean *et al*.[75] used a combination of aerosol mass spectrometry and X-ray photoelectron spectroscopy to show that for particles formed by the ozonolysis of α-pinene, the surface O:C ratio (outermost <10 nm) was lower than that of the bulk. Although less directly atmospherically relevant, McIntire *et al*.[76] found that aggregates formed from the ozonolysis of a self-assembled monolayer had a smaller O:C ratio at the surface compared to the bulk, suggesting they had a polar core with a less polar hydrophobic shell. These studies highlight the importance of understanding the nature of the particle surface and characterizing not only the specific functionalities found at the interface but also the overall average composition of atmospheric particles.

Some studies have shown that diffusion limitations in viscous particles can also hinder re-evaporation of species into the gas phase. Pfrang *et al*.[79] showed that the chemical aging of particles resulted in the formation of a solid 'crust' at the surface, which reduced diffusivity

within the particle and inhibited the transport of molecules from the bulk to the surface. A study using a particle core of limonene SOA coated with β-pinene SOA observed that the outer surface layer of the particles preferentially evaporates over the inner, observed in the hindered evaporation of the limonene core by the β-pinene SOA coating. [80] Additionally, Zelenyuk *et al*.[81] showed that when polycyclic aromatic hydrocarbons (PAHs) are present during SOA formation, they are trapped within the SOA particle with limited evaporation observed, whereas when particles are formed and subsequently exposed to PAHs, the PAHs remain on the surface and evaporation is relatively fast. Hindering re-evaporation into the gas phase can aid in the transport of pollutants across long distances.

1.3 Organic Nitrates and Nitriles in the Atmosphere

The predominant sources of nitrogen oxides (NO and NO_2, referred to as NO_x) in the atmosphere are anthropogenic, such as motor vehicle emissions and industrial combustion processes.[82-83] NO_x can subsequently react with ozone to form nitrate radical (NO_3), an important oxidant controlling oxidation processes during night time.[84-86] In ambient air, organic nitrates are formed from two main chemical pathways: the reaction of alkenes with NO_3 radicals ,[87-92] or from radical-initiated oxidation processes in the presence of NO_x through the pathways of the alkoxy and peroxy radicals,[87-88, 93-96] including those shown in equations 1.1 and 1.2. In equation 1.2, pathway 1.2a is the dominant pathway, resulting in production of an alkoxy radical, while pathway 1.2b forms an organic nitrate.[97]

$$RH + OH + O_2 \longrightarrow RO_2 + H_2O \quad (1.1)$$

$$RO_2 + NO \xrightarrow{M} [RO_2NO] \longrightarrow RO + NO_2 \quad (1.2a)$$

$$RO_2 + NO \xrightarrow{M} [RO_2NO] \longrightarrow RONO_2 \quad (1.2b)$$

Organic nitrates encompass a large group of molecules including alkyl and hydroxy nitrates that can exist in either the gas[98-108] or the particle phases.[104-105, 107, 109-113] Figure 1.4 shows the observed distribution of measured organic nitrates during the Southern Oxidant and Aerosol Study (SOAS) in the Southern United States during summer 2013.[114] Overall, the aerosol-phase organic nitrates contributed about 40% of the total measured organic nitrates. Many other field studies have shown that organic nitrates can comprise up to ~44% of the total organic aerosol particle mass.[111-112, 115-117]

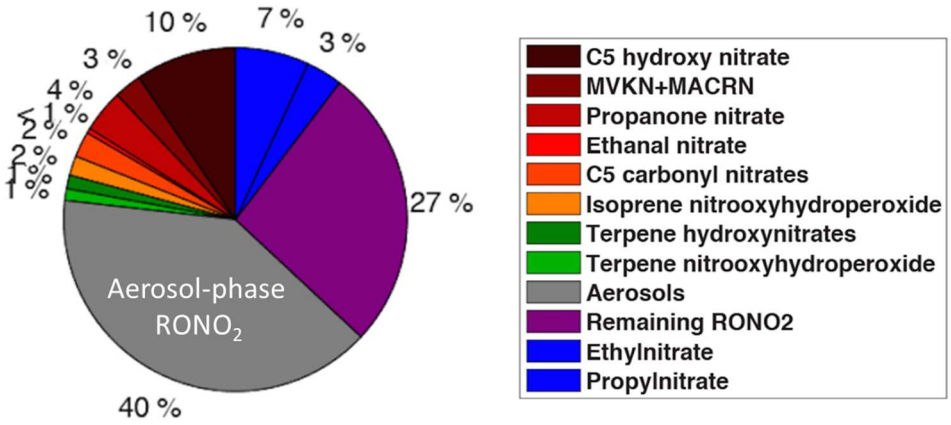

Figure 1.4: Distribution of measured organic nitrates during the Southern Oxidant and Aerosol Study (SOAS) in the Southern United States during summer 2013. Figured adapted from Zare *et al.*[114]

While organic nitrates are known to be prevalent species in polluted environments, organic nitriles have also been measured in the atmosphere.[118-119] A study by Booyens *et al.*[120] found that organic nitrile compounds were the second most abundant organic nitrogen species measured at a site in South Africa, comprising about 20% of the measured organic nitrogen-containing species. These species can form during the pyrolysis or combustion of a variety of nitrogen-containing molecules, and are often used as a marker for biomass burning.[121-122] Due to

their characteristic functional groups and relevance to the chemistry of the Earth's atmosphere, organic nitrates and nitriles were chosen as the molecular probes or tracers in the experiments studied here.

1.4 Project Goals

The goal of this project is to examine the kinetics and mechanisms that govern how gases are taken up into the particle phase on a molecular level, which will expand understanding of the mechanisms by which particles grow in the atmosphere. To probe this, this thesis follows the incorporation of three gaseous organic nitrates (2-ethylhexyl nitrate, β-hydroxyhexyl nitrate, and β-hydroxypropyl nitrate) and two organic nitriles (nonanenitrile and valeronitrile) into SOA particles formed from the ozonolysis of α-pinene under a variety of conditions. A comparison is made between experiments where the organic nitrates were incorporated *during* particle growth in a large-volume aerosol flow reactor, and experiments where they were incorporated into impacted particles *after* growth. The organic nitrates and nitriles serve as molecular probes (or tracers) to provide insight into initial surface interactions occurring between the gas and particle phases, magnitude of the partitioning of gases into particles, and diffusivity changes during incorporation.

Chapter 2: Experimental Methods

2.1 Organic Nitrate Properties and β-Hydroxynitrate Synthesis

Four organic nitrates (Figure 2.1) were used as molecular probes or "tracer" compounds because of their ability to be detected via both FTIR and mass spectrometry. Two alkyl nitrates, 2-ethylhexyl nitrate (2EHN, Sigma Aldrich, 97%) and isobutyl nitrate (IBN, Sigma Aldrich, 96%) were used as purchased. Two multifunctional nitrates, β-hydroxyhexyl nitrate (HHN) and β-hydroxypropyl nitrate (HPN), were synthesized by scaling up the method of Cavdar and Saracoglu.[123]

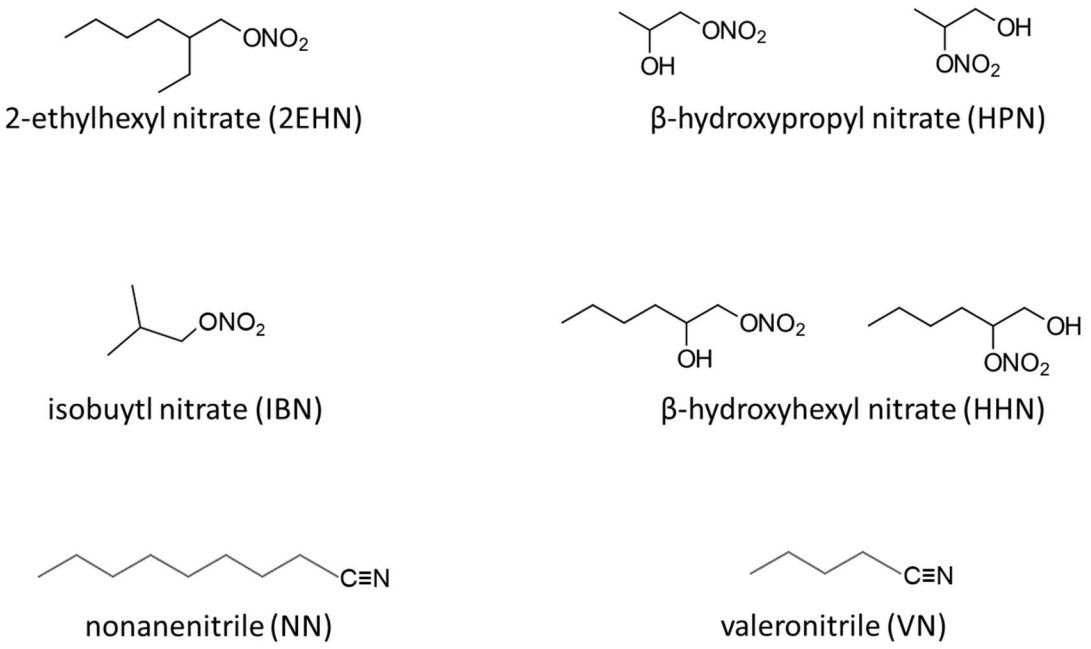

Figure 2.1: Structures of the gas phase organic nitrates and organic nitriles used in this study. The synthesis of the hydroxynitrates resulted in the presence of the two isomers.

In brief, epoxyhexane or epoxypropane were reacted with bismuth (III) nitrate•5 H_2O in a 1:2 mole ratio (typical amounts were on the order of 10^{-2} moles) in dichloromethane as the solvent. The reaction was carried out with constant stirring for 16-24 hours at room temperature under N_2 (g), after which the solvent was evaporated off *in vacuo* (Wheaton, SPIN-VAP). The

liquid product was then purified using a silica gel column, with a solvent system of 2:1 ethyl acetate:hexanes, and again the solvent was evaporated off. The resulting liquid product was characterized using FTIR (Nicolet 6700, Figure 2.2), GC-MS (Agilent 7890a GC system with a 5975C MS detector, in positive ion mode, Figure 2.3), and ^{1}H NMR (Bruker DRX500, 500 MHz, in $CDCl_3$ with 0.05% tetramethylsilane, Figure 2.4), with final purities of ~83-92% for both HPN and HHN estimated from the NMR data. Impurities were identified by comparison to pure standards as residual solvent and the corresponding di-alcohol. The isomeric ratios of the hydroxy-terminated to nitrate-terminated isomer of the pure liquid estimated by ^{1}H NMR was ~2:1 for HPN and ~4:3 for HHN.

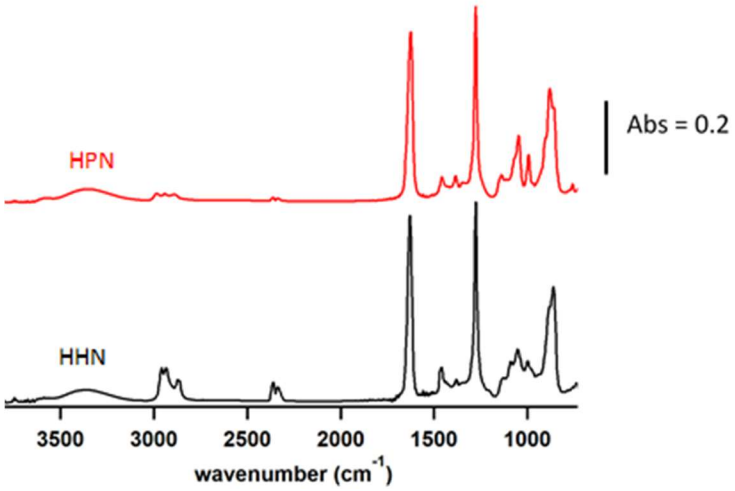

Figure 2.2: ATR-FTIR spectra of the pure liquid synthesized HPN (red) and HHN (black).

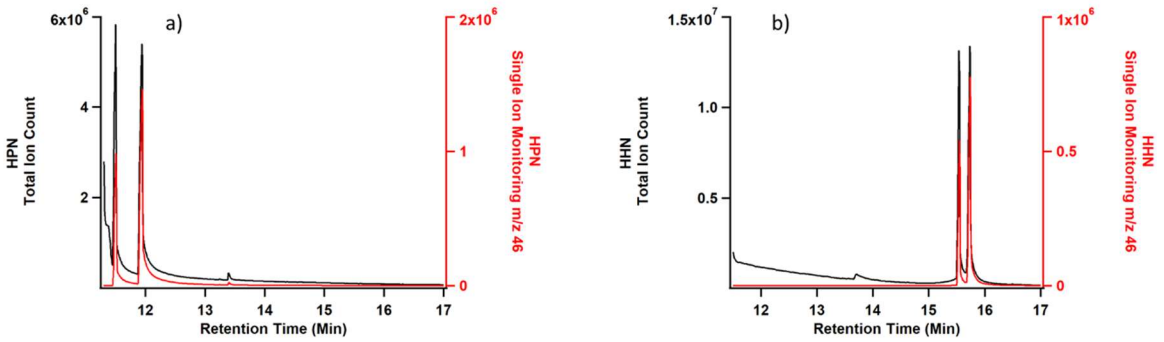

Figure 2.3: GC-MS data for the pure liquid HPN and HHN. a) Total ion chromatogram (black) and single ion monitoring *m/z* 46^+ (red) for HPN, and b) total ion chromatogram (black) and single ion monitoring *m/z* 46^+ (red) for HHN solutions (approximately 100 mM in dichloromethane). The two peaks indicate the two isomers (hydroxy-terminated and nitrate-terminated) present in the solution.

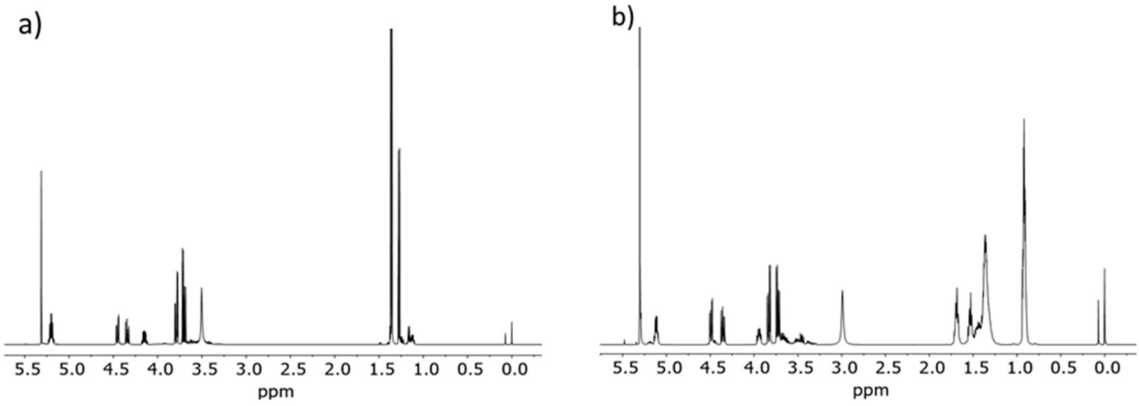

Figure 2.4: ^{1}H NMR (500 MHz, in $CDCl_3$ with 0.05% tetramethylsilane) of a) HPN and b) HHN.

In addition, the purity of the gas-phase organic hydroxynitrates (HHN and HPN) from the headspace of the trap was examined by direct analysis in real-time mass spectrometry (DART-MS) using a triple quadrupole mass spectrometer (Waters, Xevo TQ-S) with a DART ionization source (Ion-Sense, DART SVP with Vapur® Interface). Since DART is an ambient ionization method, quantification is difficult, but identification of the nitrates and some impurities using this method is reliable. Conditions used were as follows: helium gas flow, 3.1 L min^{-1}; grid

electrode voltage, 350 V; DART temperature, 25 °C. DART-MS measurements were performed at low temperature to minimize thermal decomposition of the organic nitrates.[124-125] All mass spectra were recorded in the positive ion mode for *m/z* ranging from 25 to 400. The mass spectra for both HPN and HHN, as well as the mass spectra for the corresponding di-alcohols, are shown in Figure 2.5. The predominant peaks in the DART spectra are due to $[2M+H-NO_2]^+$ at *m/z* 197 and 281 for HPN and HHN, respectively. There was little to no evidence for the corresponding di-alcohol in the gas-phase above the liquid.

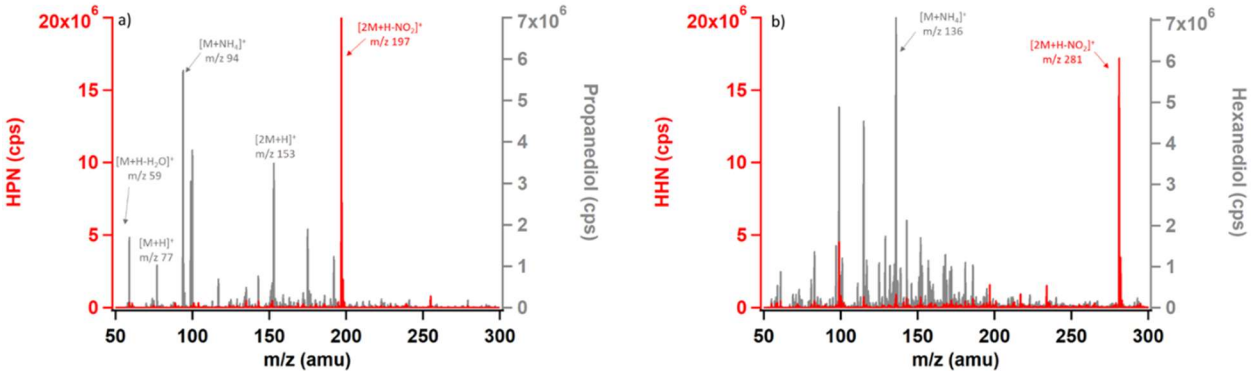

Figure 2.5: DART-MS spectra for the vapors from the headspace of a) pure HPN in the glass trap (red) and pure propanediol (grey), and b) pure HHN in the glass trap (red) and pure hexanediol (grey).

These organic nitrates were chosen due to their similarities in either functional group/structure or physical properties. The vapor pressures were estimated using two group contribution methods,[126-128] and are listed in Table 2.2. The estimated vapor pressures for 2EHN and HPN are very similar. Although HPN has a much shorter hydrocarbon tail, it compensates for it with additional hydrogen-bonding capacity through the hydroxyl group. HHN has a lower vapor pressure than 2EHN, but it has the same hydrogen-bonding capacity as HPN through the additional OH group, and it also has a long hydrocarbon tail similar to 2EHN. IBN was chosen

as another representative alkyl nitrate comparable to 2EHN but with a short hydrocarbon tail for comparison to HPN.

Table 2.1: Molecular properties of the organic nitrates at 25 ° C.

Organic Nitrates	MW (g mol^{-1})	ρ (g mL^{-1})	Vapor Pressure using Moller[127-128] (atm)	Vapor Pressure[d] using SIMPOL.1[126] (atm)	Measured Gas Phase Concentration (atm)
2EHN	175	0.96	1.4×10^{-4}	1.8×10^{-4}	$(1.9 \pm 0.1) \times 10^{-4}$
IBN	119	1.0	1.6×10^{-2}	9.1×10^{-3}	n/a[e]
HPN	121	1.2	1.2×10^{-4} [a] 3.5×10^{-4} [b] Average[c] = $(2.5 \pm 1.8) \times 10^{-4}$	1.6×10^{-4}	$(1.6 \pm 0.1) \times 10^{-4}$
HHN	163	1.1	3.5×10^{-6} [a] 6.4×10^{-6} [b] Average[c] = $(5.0 \pm 2.1) \times 10^{-6}$	8.4×10^{-6}	$(7.1 \pm 2.1) \times 10^{-6}$

[a]Hydroxy-terminated isomer
[b]Nitrate-terminated isomer
[c] Error bars are $\pm 1\sigma$.
[d]SIMPOL.1 does not distinguish between isomers
[e]The gas phase concentration for IBN was not measured directly from a trap of the pure liquid

2.2 Organic Nitrile Properties

In addition to the organic nitrates, two organic alkyl nitriles were also used as molecular probes: nonanenitrile (NN, Sigma Aldrich, 98%) and valeronitrile (VN, Sigma Aldrich, 99.5%). The structures of NN and VN are also shown in Figure 2.1. These nitriles were chosen due to their respective vapor pressures, which were estimated using a group contribution method.[127-128] NN has a very similar vapor pressure to 2EHN and HPN, while VN has a similar vapor pressure

to IBN. The vapor pressures are listed in Table 2.2, along with their molecular weights and densities.

Table 2.2: Molecular properties of organic nitriles.

Organic Nitrile	MW (g mol^{-1})	ρ (g mL^{-1})	Vapor Pressure using Moller[127-128] (atm)	Vapor Pressure[a] using SIMPOL.1[126] (atm)
NN	139	0.79	1.3×10^{-4}	n/a
VN	83	0.80	9.2×10^{-3}	n/a

[a]SIMPOL.1 does not have organic nitrile functional groups included

2.3 Gas Phase Measurements for Molecular Probes

The gas phase concentrations for 2EHN, HPN, and HHN were measured by flowing air at 1 L min^{-1} through the trap containing each nitrate into a 1 mL sampling loop on the GC-MS and comparing to a calibration using the synthesized liquid standards. Figure 2.6 shows the GC-MS calibration curves for each organic nitrate using the *m/z* 46^{+} peak area and the measured concentrations coming out of the trap. These measured concentrations are also listed in Table 2.1 and are in good agreement with the estimated vapor pressures for these species.

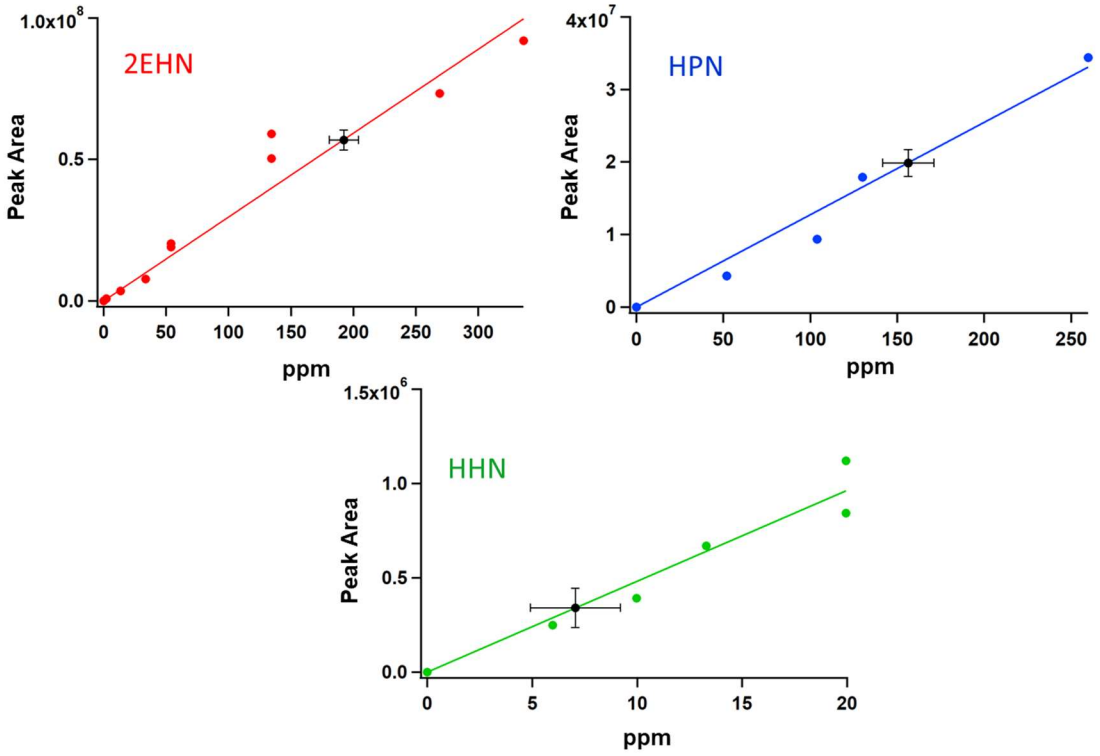

Figure 2.6: GC-MS calibration curves using liquid standards for 2EHN, HPN and HHN. Black markers show the measured gas-phase concentrations directly out of the trap. Error bars are ± 1σ from the average of three measurements.

Gas phase HHN, HPN, and in some experiments 2EHN were introduced into the flow reactor by flowing one L min^{-1} clean, dry air through a trap containing the pure liquid and subsequently diluting into a total flow of 34 L min^{-1} into the flow reactor. Hereafter, the concentration measured by GC-MS of 2EHN, HPN or HHN exiting the trap is used in all calculations, factoring in any additional dilution factors, except in the case of 2EHN at variable 2EHN (g) concentrations as described below. For example, after the dilution factor of 34 in the flow reactor, the final gas phase concentrations are 1.4×10^{14} (2EHN), 1.2×10^{14} (HPN), and 5.0×10^{12} (HHN) molecules cm^{-3} (corresponding to 5.7 ppm 2EHN, 4.9 ppm HPN, and 0.2 ppm HHN, respectively). The concentration of 2EHN measured by GC-MS directly from the flow reactor ($1.4 \pm 0.2 \times 10^{14}$ molecules cm^{-3}, 1σ) was in good agreement with this value. However,

this comparison was not possible for HPN and HHN due to greater losses in the sampling line. Although some organic nitrate is expected to be lost to the walls of the flow reactor, for some experiments the walls were conditioned with a flow of the organic nitrate overnight, and there was no statistical difference found between these experiments and those without overnight conditioning.

Some experiments examined variable gas phase concentrations of the molecular probes, and in these experiments the gas phase species was introduced by injection of the pure liquid from an automated syringe pump (New Era Pump System Inc., Model NE-1000) into a 9-10 L min^{-1} flow of clean, dry air, and subsequently diluting to 34 L min^{-1} total flow as described below. The concentrations of 2EHN, IBN, NN, and VN were measured by GC-MS directly from the flow reactor and calibrated by comparison to liquid standards.

2.4 Additional Molecular Probes

Some experiments were done using either heptafluorobutyric acid (HFBA, Sigma Aldrich, 98%), 1-dodecyne (DC, Sigma Aldrich, 98%), perfluorosebaconitrile (PFN, Synquest Labs, 97%), or ethyl cyanoacetate (ECN, Sigma Aldrich, ≥ 98%) as the molecular probe. PFN was used for a preliminary experiment as a probe that is more inert to oxidation by OH compared to other probes, since fluorinated nitriles have much slower rate constants for reaction with OH than other species.[129-131] However, there was no evidence by ATR-FTIR of particulate-phase PFN, and PFN's structure and properties were different from the common organic aerosol compounds. Thus, further experiments with PFN were not performed. Additionally, some preliminary experiments were done with ECN as the molecular probe. There was no

experimental evidence for particle-phase ECN. A previous study showed that ECN can interact strongly with metal surfaces such as ZnO (s), which may indicate an affinity of the ECN for metal surfaces such as that of the stainless steel flow reactor.[132] Cyanoacetates are also known to react with aldehydes in the condensed phase to produce the acrylate derivative.[133] Due to these uncertainties, further studies with ECN were not performed.

The HFBA exhibited a prominent color change upon exposure to stainless steel surfaces, as shown in Figure 2.7. A vibrant pink color was seen at the end of experiments after injection of the HFBA liquid into an air stream using a stainless steel tee for introduction into the flow reactor (Figure 2.7a), and after a separate experiment where the pure liquid was mixed with a stainless steel hardware component overnight (Figure 2.7b). This reaction occurs upon injection into the stainless steel reactor and likely occurs on the walls of the flow reactor interior, and thus further experiments with HFBA were not done.

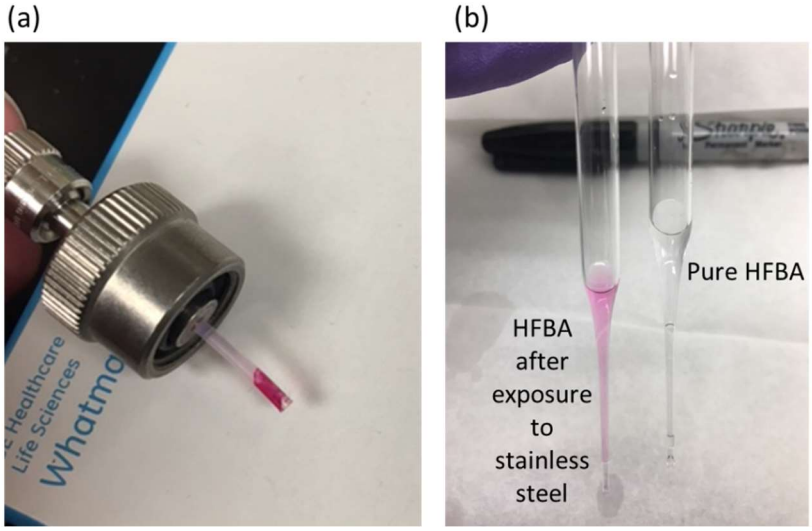

Figure 2.7: a) The pure HFBA liquid at the end of the syringe pump tip at the end of an experiment, after the tip was connected to a stainless steel tee for ~8 hours. b) Pure HFBA liquid in a syringe (right), and the HFBA liquid after mixing overnight with a piece of stainless steel hardware (left).

DC is an alkyne with a long 12-carbon tail and an estimated vapor pressure of 2.4×10^{-4} atm.[127-128] This vapor pressure is similar to that of 2EHN and would make it a good candidate for a molecular probe. However, a preliminary experiment with DC showed a ~10% increase in the total particle number upon addition of the DC to the flow reactor system. The reactions of alkynes with ozone have rate constants smaller than that of ozone with α-pinene (AP).[1, 131, 134] Assuming a rate constant of $\sim 10^{-20}$ cm^3 $molecule^{-1}$ s^{-1} for the reaction of DC with ozone, the initial rate of loss with respect to ozone is found by $k_{O3}[X]$, where X is DC or AP. This initial rate of loss for 3 ppm of DC to ozone is $\sim 7 \times 10^{-7}$ s^{-1}, whereas for 250 ppb AP it is $\sim 1 \times 10^{-4}$ s^{-1}, indicating that the reaction of DC with ozone is negligible. However, the rate constant with OH radical estimated for DC is $\sim 10^{-11}$ cm^3 $molecule^{-1}$ s^{-1}, similar to that of AP.[131, 135] The reaction of OH with the hydrocarbon tail of DC likely creates species of much lower volatility, some of which may be able to nucleate particles themselves, thus contributing to the total particle number. For this reason, DC was not used in further experiments.

2.5 SOA Generation

SOA from the ozonolysis of AP was generated in the stainless steel flow reactor with a total flow rate of 34 L min^{-1}, and all reactants were introduced in the initial mixing section of the reactor. Gas-phase AP (100 ppb to ~1.5 ppm) was generated by injection of the pure liquid (Sigma Aldrich, >99%) from an automated syringe pump (New Era Pump System Inc., Model NE-1000) into a 9-10 L min^{-1} flow of clean, dry air. Ozone was generated by flowing 0.4 L min^{-1} O_2 gas (Praxair, 99.993%) through a Pen-Ray® mercury lamp (UVP, LLC), and was subsequently diluted with 9.6 L min^{-1} of air before being added to the system. An additional 14

L min^{-1} of air was introduced to create a total flow rate of 34 L min^{-1}, and the resulting reactor concentrations were 250-300 ppb O_3 measured using an ozone monitor (Teledyne Photometric O_3 Analyzer 400E; Advanced Pollution Instrumentation, Inc. Photometric O_3 Analyzer 400). The reaction of AP with O_3 produces OH radicals which, unless scavenged, will react with the organic nitrates.[136] Thus, in some experiments cyclohexane (CH, Fisher Scientific, 99.9%), used as an OH scavenger, was evaporated into the flow of air to give a concentration of 2.5×10^{15} molecules cm^{-3} (100 ppm). When molecular probes were used, they were injected simultaneously with AP and CH into the flow reactor using either 1 L min^{-1} of air through a trap containing the pure liquid, or by injection of the pure liquid into the air stream using a syringe pump as described previously. When the trap was used, the air flow for the AP air stream was reduced to 9 L min^{-1} to maintain a total flow of 34 L min^{-1} in the flow reactor.

Gas phase concentrations of AP and CH were measured using EI GC-MS (Agilent 7890A GC system with a 5975C MS detector, in positive ion mode) in a dual total ion/single ion monitoring (SIM) system with the particles and ozone filtered out using a quartz filter (Whatman™) and a potassium iodide (100.0%, Fisher Chemical) ozone scrubber, respectively. Total ion monitoring was used for CH, while *m/z* 93^+ was followed in SIM mode for AP. At the higher concentrations of AP ($[AP]_0 > 500$ ppb), the measured concentration in the flow reactor was slightly higher than expected, likely due to puddling of the AP at the injection site. The initial concentration of AP for these conditions was estimated using a kinetics model (described below) and Kintecus®,[137] which was run until the output concentrations matched the concentrations of AP measured from the flow reactor by GC-MS (within ~30 ppb). Modeling the reaction conditions for the 100 ppb and 250 ppb AP concentrations produced AP

concentrations that agreed with the GC-MS measured values within ~50%, and ozone concentrations that agreed within ~7%.

Particle size distributions were monitored using a scanning mobility particle sizer (SMPS, TSI), equipped with either a model 3071A classifier and 3022A CPC or with a model 3080 classifier and 3776 CPC, and an aerodynamic particle sizer (APS, TSI Model 3321). The size distributions were combined using the SMPS data below 500 nm and APS data above 700 nm mobility diameter assuming a particle density of 1.2 g cm^{-3},[138] and fit with a Weibull 5-parameter distribution as described by Perraud *et al.*[52]

To check the validity of the Weibull fit, an Aerodynamic Aerosol Classifier (AAC, Cambustion Ltd., UK) was used with a CPC (TSI, model 3776) to scan the entirety of the range covered by the SMPS and the APS. The AAC measures aerodynamic diameter, and these diameters were converted to mobility diameters using a particle density, ρ_p, of 1.2 g cm^{-3} for α-pinene SOA and the Cunningham slip correction factors as a function of diameter, $C_c(d)$, as in Equation 2.1[10]

$$d_a = d_m \left[\frac{C_c(d_m)}{C_c(d_a)}\right]^{1/2} \left[\frac{\rho_p}{\rho_0}\right]^{1/2} \qquad \text{Equation 2.1}$$

where ρ_0 is the standard density (1.0 g cm^{-3}).

Figure 2.8a shows an example data set of the SMPS, APS, and Weibull fit for a representative particle number distribution, and Figure 2.8b shows the comparison of the Weibull fit with the AAC+CPC data for the same particle distribution. Excellent agreement is observed between the two traces, validating the Weibull fit.

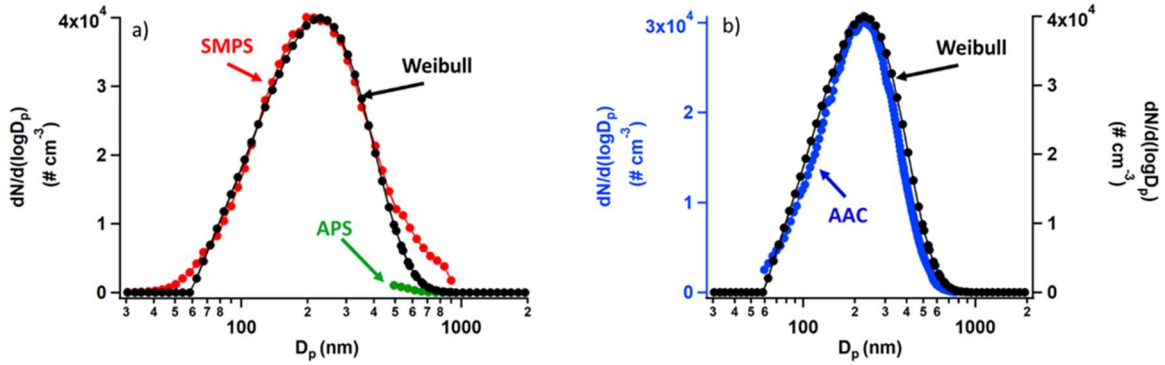

Figure 2.8: a) The SMPS, APS, and Weibull fit data for a representative particle number distribution, and b) the Weibull fit and AAC data for the same SOA.

2.6 Overview of Experimental Setup for Incorporation *During* Growth and *After* Growth

Figure 2.9 shows a schematic of the four experimental configurations used in these studies. In the first study for incorporation *after* growth (series A), nitrate-free SOA particles formed from AP ozonolysis were generated in a large volume, slow flow stainless steel aerosol flow reactor[139] and impacted on an attenuated total reflectance (ATR) crystal to generate a thin film of SOA particles, over which gas phase tracer was flowed and uptake was measured until equilibrium was reached. Thin films of various model substrates were also studied in series A, described in section 2.7. This method was limited to higher concentrations of the gas phase (approaching saturation vapor pressure) in order to detect -ONO_2 or -CN peaks by ATR-FTIR. A benefit of this method over in situ production of organic nitrates or other tracer species is that it avoids oxidation of the gas phase compounds from gas phase OH generated during ozonolysis in the reactor.

In series B, SOA particles (also from the large flow reactor) were first passed through a monolith carbon denuder (NovaCarb™; MAST Carbon, Ltd.) to remove gas phase species and

then flowed into a smaller glass flow tube, where they were exposed to gaseous $RONO_2$. This series was carried out to ensure that the observations were in agreement with series A results on impacted particles, and as a second method of incorporation *after* growth for comparison to the following series probing incorporation *during* growth.

In series C and D, the tracers were introduced into the stainless steel flow reactor and incorporated into SOA particles as the particles formed and grew in the reactor (*during* growth). Smaller concentrations of the tracers than those in series A were used here due to the much larger volumes of air and hence higher dilution factors that are associated with the large flow reactor. In series C, the organic nitrate in the particles was quantified *on-the-fly* by high resolution time-of-flight aerosol mass spectrometry (HR-ToF-AMS). In series D, the same particles as in series C were simultaneously impacted on an ATR crystal, and quantification of each organic nitrate ($RONO_2$) was carried out by FTIR.

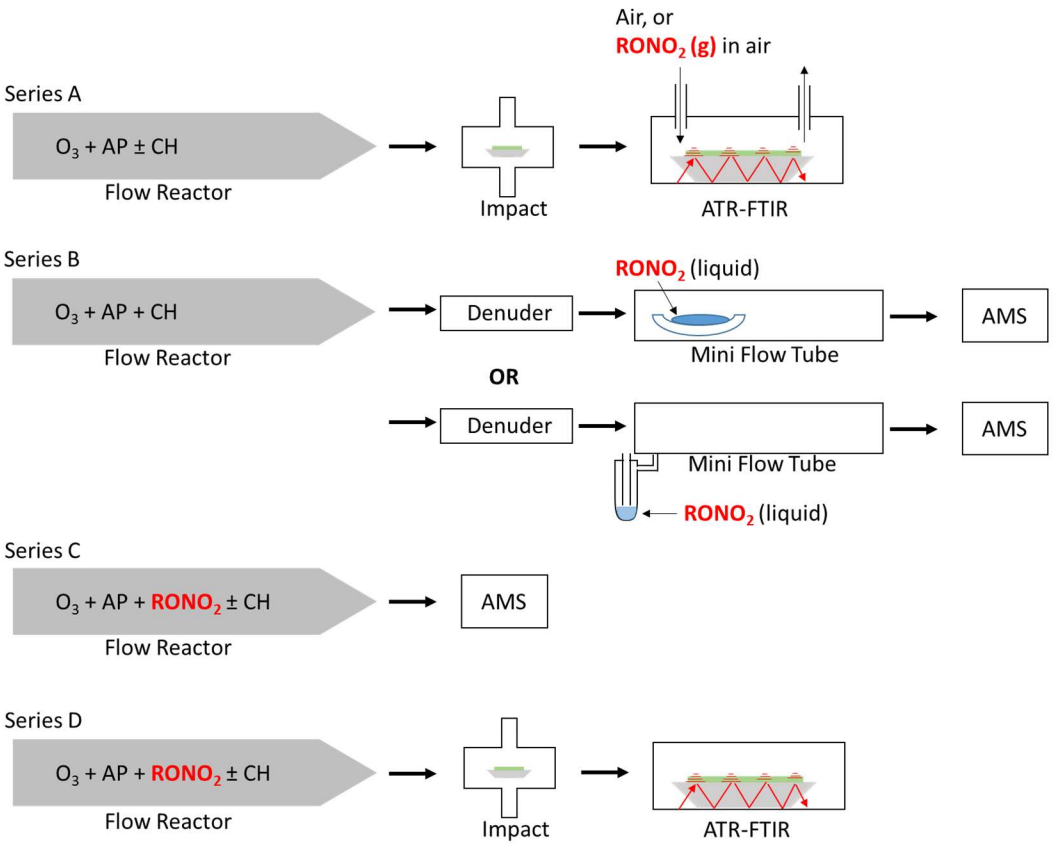

Figure 2.9: Schematic of the four experiment types. In series A, SOA particles are formed in the absence of the tracer in the stainless steel flow reactor and impacted on an ATR crystal to generate a thin film of particles, over which gas phase tracers at near saturation vapor pressures were flowed, and the uptake was measured by ATR-FTIR. In series B, SOA particles were generated in the stainless steel flow reactor and then passed through a charcoal denuder before subsequently being flowed into a 1-m long glass flow tube and exposed to $RONO_2$ through either a reservoir with a pure liquid or a trap flowing air over the pure liquid, and were then analyzed by HR-ToF-AMS. In series C, gas phase tracers at lower concentrations than those used in series A were incorporated into SOA particles as they formed and grew in the stainless steel flow reactor. These particles were quantified by HR-ToF-AMS. In series D, the same particles as in Series C were impacted on an ATR crystal, and partition coefficients were determined from the quantification of the tracer by ATR-FTIR.

For series A experiments, each individual organic nitrate was introduced by flowing air through the glass trap to yield high gas-phase concentrations approaching the saturation vapor pressure before being introduced into the ATR-FTIR cell described in section 2.9. For the limited series B experiments, a reservoir of liquid $RONO_2$ was placed inside the mini flow tube

in order to expose particles *on-the-fly* to the saturation vapor pressure of the $RONO_2$ in a total flow of air of 0.4 – 1.5 L min^{-1}. In a separate experiment for series B, a glass trap containing the pure $RONO_2$ liquid was used in place of the reservoir to flow 0.04-0.15 L min^{-1} into the mini flow tube to provide more dilute gas phase concentrations. For series C and D experiments, each tracer was introduced either by flowing 1 L min^{-1} air through the glass trap containing the pure liquid or by injection of the pure liquid using a syringe pump into a stream of air totaling 10 L min^{-1} simultaneously with AP, either with or without CH. The gas phase concentrations of the tracers used in each experiment type are summarized in Table 2.3.

Table 2.3: Gas phase concentrations for all tracers used in each experiment type.

	2EHN	**HPN**	**HHN**	**NN**	**IBN**	**VN**
Series A	190 ppm	160 ppm	7 ppm	100 ppm	n/a	n/a
Series B	120 ppm/12 ppm	80 ppm/6.6 ppm	n/a	n/a	n/a	n/a
Series C/D	0.05-5.6 ppm	4.7 ppm	0.21 ppm	0.26-3.1 ppm	1.0-8.0 ppm	8.0 ppm

2.7 Organic Thin Film Preparation

The substrates used in series A for incorporation after growth include a non-polar long chain alkane (triacontane, TC), an amorphous ester oligomer (poly(ethylene adipate) di-hydroxy terminated, PEA), a keto-acid (pinonic acid, PA), and SOA from AP ozonolysis formed either with or without an OH scavenger (Figure 2.10). The alkane might be considered a model for

primary organic aerosol,[140] while the keto-acid and ester are representative of functionalities found in SOA.[141-146]

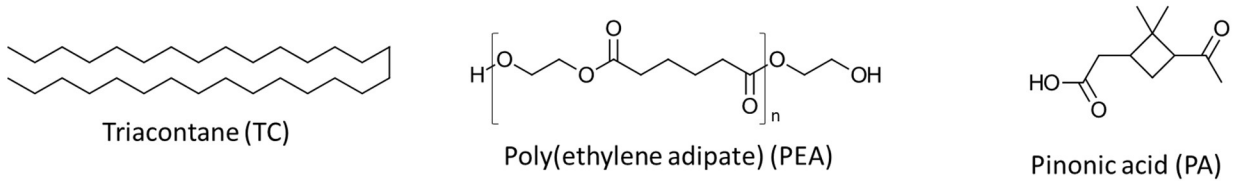

Figure 2.10: Not including SOA, structures of the organic thin film substrates triacontane (TC), poly(ethylene adipate) (PEA), and pinonic acid (PA).

To create thin films of the SOA particles, the polydisperse particles formed in the flow reactor were collected onto a Ge ATR crystal using a custom-designed impactor with a 50% cut-off diameter of 240 nm.[70] Figure 2.11 shows a schematic of the impactor. The particles were sampled at a total flow of 30 L min^{-1} for 10-30 min at the end of the reactor (~20-60 μg total impacted mass), corresponding to a reaction time of 31 min.

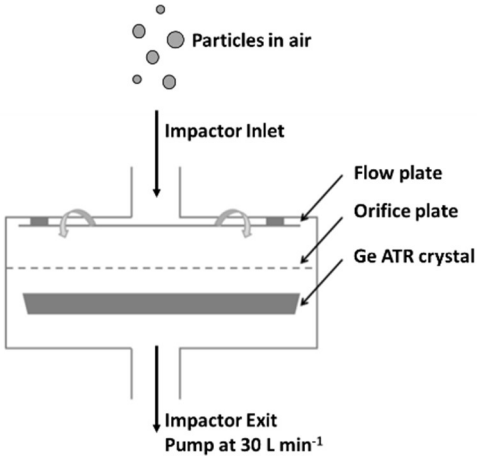

Figure 2.11: A schematic of the impactor. Figure adapted from Kidd *et al.*[70]

Thin films of model organic compounds were created by dissolving the pure solid in solvent (hexanes, dichloromethane, methanol, or acetonitrile) and spreading a known volume (5-20 μL) of the solution onto the exposed face of the ATR crystal. The solvent was removed using a flow of dry N_2 (g) until only the dry solid remained. The amount of organic substrate or impacted particles on the crystal was varied to ensure the film thickness was smaller than the depth of penetration (d_p) of the infrared evanescent wave, and thus ensured that the entire film was probed by the IR beam. The depth of penetration was calculated from the wavelength of the peak of interest and the refractive indices of the Ge crystal and air to be 0.35 μm at 1730 cm^{-1}, 0.37 μm at 1630 cm^{-1}, and 0.47 μm at 1280 cm^{-1}.[138, 147-148] For a sufficiently thin film, the effective path length (l) of the infrared beam through the organic film can be estimated using d_p and factoring in the 10 bounces of the beam within the ATR crystal, giving total path lengths of 3.5 μm at 1730 cm^{-1}, 3.7 μm at 1630 cm^{-1}, and 4.7 μm at 1280 cm^{-1}.[147] The 1280 cm^{-1} peak was used for analysis of the organic nitrates, since there was some overlap of the substrate carbonyl peaks with the 1630 cm^{-1} peak of the $–ONO_2$ group. Substrate films were prepared to allow penetration of the IR beam throughout the entire film if evenly spread over the crystal, but due to inhomogeneity in the distribution of the films over the crystal surfaces (Figure 2.12), this may not be the case in some regions of the film.

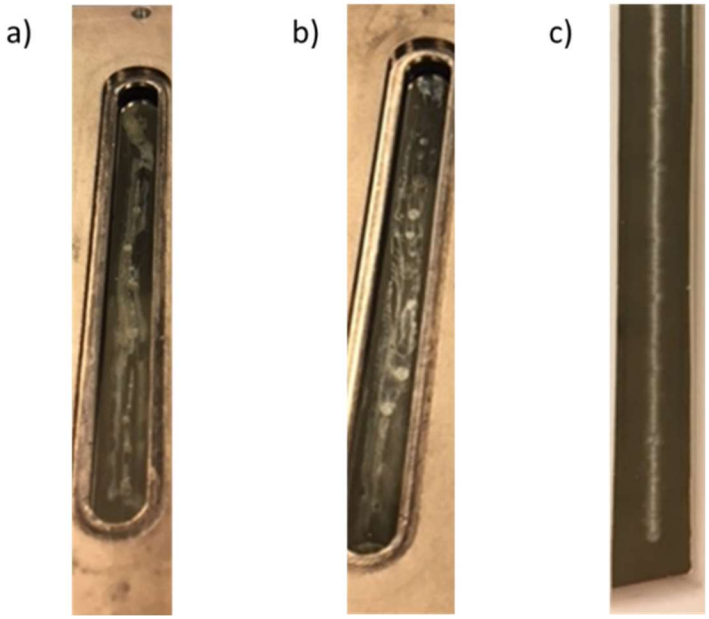

Figure 2.12: Typical films of a) PEA, b) PA, and c) SOA. The white regions on the crystal face show the deposited substrate scattering the overhead light.

2.8 FTIR Absorption Cross Section Measurements

Absorption cross sections for each tracer and substrate were obtained using transmission through a 0.5 mm pathlength KBr cell or by filling the ATR cell with a solution of known concentrations ranging from 1.0 to 1.0×10^{-3} M and covering the cell with a glass lid to prevent evaporation. Solutions for FTIR cross section measurements were made in either dodecane, methanol, or acetonitrile.

To calculate the pathlength within the ATR cell through a thick film such as the case when the cell is filled with solution, the effective thickness (d_e) of the solution in the cell was calculated using the wavelength of interest and the refractive indices of the Ge crystal and the solvent.[147] Accounting for the 10 bounces within the crystal, the effective pathlength (l_{eff}) through an acetonitrile solution was 2.3 μm at 2250 cm^{-1}, 3.0 μm at 1730 cm^{-1}, 3.2 μm at 1630 cm^{-1}, and 4.0 μm at 1280 cm^{-1} respectively. The measured cross sections from the two methods

agreed within 5%, and averages are provided in Table 2.4, which includes the cross section at 1280 cm^{-1} for each organic nitrate, the cross section at 2250 cm^{-1} for organic nitriles, and the carbonyl cross section for PA, PEA and a proxy cross section for SOA comprised of the average of the cross sections of PA, tartaric acid, valeric acid and 2-nonanone.

Table 2.4*:* FTIR cross sections (in cm^2 $mole^{-1}$, base 10) of the $–ONO_2$, C≡N, or C=O for the organic nitrates, nitriles, PA, PEA, and a proxy SOA at a resolution of 8 cm^{-1}.

Compound	$\sigma^{a,b}$ (Units of 10^5 cm^2 $mole^{-1}$ $–ONO_2$, C≡N, or C=O, base 10)
2EHN	4.4 ± 0.1
HHN	3.2 ± 0.1
HPN	3.6 ± 0.1
IBN	3.9 ± 0.1
NN	0.26 ± 0.01
VN	0.11 ± 0.01
PEA	3.5 ± 0.1
PA (1704 cm^{-1})	3.6 ± 0.1
Tartaric Acid	3.3 ± 0.1
Valeric Acid	1.7 ± 0.1
Nonanone	2.7 ± 0.2
SOA	2.8 ± 0.8

[a]Error bars are ± 1σ.
[b] Cross sections were determined from the height of the characteristic peaks for each compound (1280 cm^{-1} for organic nitrates, 2250 cm^{-1} for organic nitriles, and 1700-1730 cm^{-1} for C=O) using standard solutions, and for carbonyl-containing compounds normalized to the number of carbonyls on the molecule. For PEA, six subunits of the polymer were assumed, resulting in a total of 12 C=O for every PEA molecule. Carbonyl cross section for SOA was estimated as the average of the cross sections for pinonic acid, tartaric acid, valeric acid, and nonanone.

The ATR-FTIR spectra for a solid PA film and a standard solution are shown in Figure 2.13. The presence of hydrogen bonding in the solid caused overlap of the acid and ketone

carbonyl peaks, whereas in solution these are two distinct peaks. Due to this overlap in the solid phase, the peak cross section at 1704 cm^{-1} for the liquid solution was used to quantify the thickness of solid PA films. For all nitrates and substrates, the quantification was made based on the cross section determined from the liquid solutions.

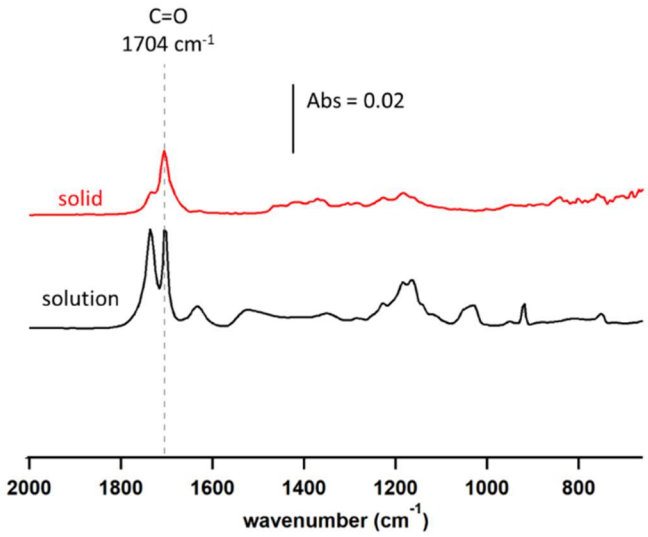

Figure 2.13: ATR-FTIR spectra for a solid PA film (red), and a liquid PA solution in acetonitrile (black, 56 mM). The absorbances in the black trace have been multiplied by 0.03.

2.9 Uptake onto Thin Films

Figure 2.14 shows a schematic diagram of the ATR-FTIR cell used in series A for uptake into thin films. For each uptake experiment, a Ge crystal coated with the target substrate was placed in the cell (total volume ~2 cm^3) in the sampling compartment of an FTIR spectrometer (Nicolet 6700). The spectrum of each sample was acquired using 4 co-added scans with a resolution of 8 cm^{-1}, yielding a time resolution of 1 data point approximately every 3 seconds. The film alone was first exposed to 60 ± 5 cm^3 min^{-1} clean, dry air from a purge air generator (Parker-Balston, model 75-62) for 15-300 seconds to dry the film and to bring any spreading that might occur under a gas flow to a steady-state before the addition of the nitrate. The organic

nitrates were then introduced into the ATR cell by flowing clean, dry air at a flow rate of 60 ± 5 cm^3 min^{-1} over the pure liquid of each organic nitrate contained in a glass trap at room temperature. The gas-phase concentrations were assumed to be equivalent to the saturation vapor pressure of the organic nitrate. The trap was replenished daily with fresh organic nitrate (synthesized hydroxynitrates were stored in a freezer under N_2 (g)). In some cases, the organic nitrate signal in the IR decreased over the course of a day, indicating there may have been some decomposition in the trap. When decomposition was observed, only data from the first run of the day were used. Additional experiments where the time during which the film was exposed to the organic nitrate was doubled also showed stability of the organic nitrate signal, indicating decomposition was minimal over the length of the experiments. A set of additional experiments were done using NN for comparison, where the NN (g) was introduced using a syringe pump to inject the pure liquid into an air stream of ~3 L min^{-1}, from which 75 cm^3 min^{-1} of the air containing NN (g) was diverted into the ATR cell.

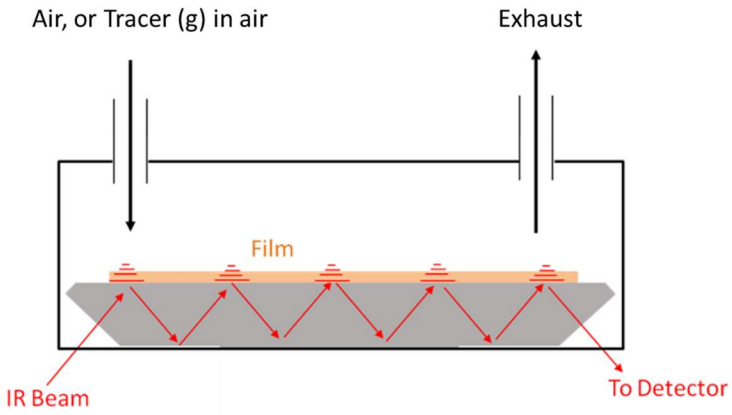

Figure 2.14: Schematic of the ATR uptake apparatus for series A (incorporation *after* growth).

The characteristic peaks of the nitrate (1280 and 1630 cm^{-1}) or nitrile (2250 cm^{-1}) were monitored over time along with the carbonyl peaks of the organic film (1700-1730 cm^{-1}) while the gas-phase nitrate flowed over the film. For TC, which has no carbonyl functional group, the

C-H peak at 2915 cm^{-1} was followed. After the organic nitrate signal reached steady-state, the flow was replaced with 60 ± 5 cm^3 min^{-1} clean, dry air to follow the desorption of the tracer as a function of time. To quantify the amount of nitrate taken up into the film in units of molecules cm^{-2}, FTIR cross-sections for the organic nitrate tracers (1280 cm^{-1}) and the organic substrates C=O stretch (1700-1730 cm^{-1}) were obtained as described in section 2.8.

To calculate the mole ratio of nitrate to carbonyl groups for each substrate, Equation 2.2 was used:

$$\frac{A_{nit}}{A_{C=O}} \times \frac{l_{C=O} \times \sigma_{C=O}}{l_{nit} \times \sigma_{nit}} = \frac{[-ONO_2]}{[C=O]} \qquad \text{Equation 2.2}$$

In Equation 2.2, A_{nit} and $A_{C=O}$ are the IR absorbances for the organic nitrate and the carbonyl of the substrate, respectively, σ is the absorption cross-section (cm^2 $mole^{-1}$, base 10), and l is the pathlength (cm) probed in the film at the selected wavenumbers for the carbonyl and the organic nitrate. The concentrations of nitrate and substrate, [$-ONO_2$] and [C=O], are in moles $-ONO_2$ cm^{-3} and moles C=O cm^{-3}, respectively. The depth of penetration was calculated from the wavelength of the peak of interest and the refractive indices of the Ge crystal and air to be 0.28 μm at 2250 cm^{-1}, 0.35 μm at 1730 cm^{-1}, 0.37 μm at 1630 cm^{-1}, and 0.47 μm at 1280 cm^{-1}.[147-148] For a sufficiently thin film, the path length (l) of the infrared beam through the organic film can be estimated using d_p and factoring in the 10 bounces of the beam within the ATR crystal, giving total path lengths of 2.8 μm at 2250 cm^{-1}, 3.5 μm at 1730 cm^{-1}, 3.7 μm at 1630 cm^{-1}, and 4.7 μm at 1280 cm^{-1}.[147] Substrate films were prepared to allow penetration of the IR beam throughout the entire film if evenly spread over the crystal, but due to inhomogeneity in the distribution of the films over the crystal surfaces (Figure 2.12), this may not be the case in some

regions of the film. This is particularly the case for the impacted SOA particles, which were concentrated along the center of the crystal. If the entirety of the film is not probed, initial uptake coefficients will be underestimated, since some of the signal from the tracers adsorbed on the surface will be missed. However, the measurement of the partition coefficient, which relies on a ratio of the tracer and the film IR signals as discussed below, will not be affected.

For uptake coefficients, the amount of nitrate taken up was determined from the organic nitrate peak height using Equation 2.3:

$$\frac{A_{nit}}{\sigma_{nit}} \times N_A = \{\text{-}ONO_2\} \qquad \text{Equation 2.3}$$

where A is the absorbance of the organic nitrate, σ is the cross section of the organic nitrate in cm^2 $mole^{-1}$ (base 10), N_A is Avogadro's number, and $\{\text{-}ONO_2\}$ is the amount of nitrate in the film. Although expressed as the number of $–ONO_2$ per cm^2, it is the column integrated nitrate and includes both surface and bulk contributions. By plotting the concentration over time as the film is exposed to the organic nitrate and subsequently taking the initial slope of the initial data points ($t < 20$ s), the net uptake coefficient (γ) was quantified by Equation 2.4:

$$\gamma = \frac{R_0}{[Gas] \times \sqrt{\frac{RT}{2\pi M}}} \qquad \text{Equation 2.4}$$

where R_0 is defined as the initial rate of uptake. Lastly, partition coefficients K were calculated using Equation 2.5:

$$K = \frac{[-ONO_2]_{film}}{[-ONO_2]_{air}} \qquad \text{Equation 2.5}$$

where $[\text{-}ONO_2]_{film}$ and $[\text{-}ONO_2]_{air}$ are the concentrations of organic nitrate in the film and in air, respectively, in units of moles L^{-1}. The concentration in air was estimated using the saturation vapor pressure. The $[\text{-}ONO_2]_{air}$ is the gas phase concentration measured from the trap by GC-

MS. The number of moles of $-ONO_2$ per L in the substrate film ($[\text{-}ONO_2]_{film}$) was calculated using Equation 2.6-Equation 2.8:

$$\frac{\frac{A_{nit}}{l_{nit} \times \sigma_{nit}}}{\frac{A_{C=O}}{l_{C=O} \times \sigma_{C=O}} + \frac{A_{nit}}{l_{nit} \times \sigma_{nit}}} = \frac{n_{nit}}{n_{c=o} + n_{nit}} \quad \text{Equation 2.6}$$

$$n_{C=O} \times \frac{N_{sub}}{N_{C=O}} = n_{sub} \quad \text{Equation 2.7}$$

$$\frac{n_{nit}}{n_{sub} \times M_{sub}/\rho_{sub} + n_{nit} \times M_{nit}/\rho_{nit}} = [-ONO_2]_{film} \quad \text{Equation 2.8}$$

In Equation 2.6, A_{nit} and $A_{C=O}$ are the IR absorbances for the organic nitrate and the carbonyl of the substrate, respectively, σ is the absorption cross-section (cm^2 $mole^{-1}$, base 10), l is the pathlength (cm) probed in the film at the selected wavenumbers for the carbonyl and the organic nitrate, and n_{nit} and $n_{c=o}$ are in moles $-ONO_2$ cm^{-3} and moles C=O cm^{-3}, respectively. In Equation 2.7, the $n_{c=o}$ (moles C=O cm^{-3}) is converted into n_{sub} (moles substrate cm^{-3}) using the number of carbonyl groups on each substrate molecule. This includes any carbonyl, acid, anhydride, or ester functional groups that may be present in α-pinene SOA products. The value of $N_{C=O}/N_{sub}$ is taken to be 2 for this SOA based on the literature.[141-142] In Equation 2.8, moles of substrate and moles nitrate are converted to volume (in units of L) using the molecular weight (M, assuming 200 g $mole^{-1}$ for SOA),[141-143] and the densities in units of g L^{-1} (using 1.2×10^3 g L^{-1} for SOA).[138] A similar analysis can be done for organic nitriles, replacing the $\text{-}ONO_2$ functional group with the measurement of the -CN functional group at 2250 cm^{-1}.

2.10 Aerosol Mass Spectrometer Measurements

For series B (incorporation *after* growth) and series C (incorporation *during* growth), a high resolution time-of-flight aerosol mass spectrometer (HR-ToF-AMS, Aerodyne)[149-151] was used to characterize the particles formed in the absence or presence of the gas-phase tracers and in the absence or presence of the OH scavenger. Particles were sampled at a flow rate of ~0.082 L min^{-1} into the AMS and focused with an aerodynamic lens, vaporized at 600°C, and ionized via electron impact (EI, 70 eV) ionization. The data presented were acquired in V-mode without HEPA-filter dilution. Measurements were taken with a particle filter at the beginning and end of each experiment to adjust the isotope ratio of $^{15}N^{14}N$ that interferes with the CHO^+ fragment using the "Improved-Ambient" method of Canagaratna *et al*.[152] Data were analyzed using Igor Pro v. 6.3 and 6.37 (Wavemetrics, Inc.) with SQUIRREL (v. 1.57I and 1.62A) and PIKA (v. 1.16I and 1.22A). Elemental analysis was carried out using the default calibration factors for O:C and H:C.

Previous studies have shown that organic nitrates fragment in EI ionization to yield NO^+ and NO_2^+ as major fragments,[153-157] with small $CHNO^+$ or CHN^+ fragments.[154, 156] The ratio of NO^+/NO_2^+ can be used to differentiate organic nitrates in the particles from inorganic nitrates or nitric acid.[154, 156, 158] Because of extensive fragmentation of the parent ions in the AMS, organic nitrates were measured using the peak intensities of the NO^+ and NO_2^+ fragments. However, these fragments can also be generated from inorganic nitrates and nitric acid, which could be formed by decomposition of the organic nitrates. Since these experiments were carried out at low relative humidity, hydrolysis is unlikely, and thermal decomposition at room temperature is also not expected to be significant. However, to establish that the signals are consistent with

organic nitrates, the ratio of NO^+ to NO_2^+ for all three organic nitrates, either with or without CH, was measured. Table 2.5 shows this ratio was between 3.1 and 5.4 for all of the organic nitrates used here (there was no statistical difference between 7 and 31 min reaction time). These values are consistent with the ratios for organic nitrates measured in other systems,[154-155, 159] and they differ significantly from that of nitric acid (Table 2.5).[160-161]

Table 2.5: HR-ToF-AMS ratio of NO^+ to NO_2^+ for particles formed in the presence of 1.4 x 10^{14} 2EHN molecules cm^{-3}, 1.2 x 10^{14} HPN molecules cm^{-3}, and 5.0 x 10^{12} HHN molecules cm^{-3}, either with or without the OH scavenger CH (Series C). For comparison, that of nitric acid is also given.

		Ratio[a] of NO^+ to NO_2^+	
		No CH	With CH
Organic Nitrate	2EHN	5.4 ± 0.3	4.9 ± 1.6
	HPN	3.4 ± 0.3	3.1 ± 0.2
	HHN	4.6 ± 0.2	3.6 ± 0.4
	Nitric Acid [160-161]	0.33 - 0.86	

[a]Error bars are ± 2σ from the average of three experiments for the organic nitrates.

The ratios in Table 2.5 indicate that the organic nitrate functional group remains unreacted once taken up into the particles. One possible fate of organic nitrates in particles is hydrolysis to inorganic nitrate (NO_3^-). However, the FTIR data does not show detectable peaks due to inorganic NO_3^- (Figure 2.15) by comparison to $NaNO_3$ (Fisher Scientific, 99.9%). This supports that the organic nitrate functional group remains unreacted.

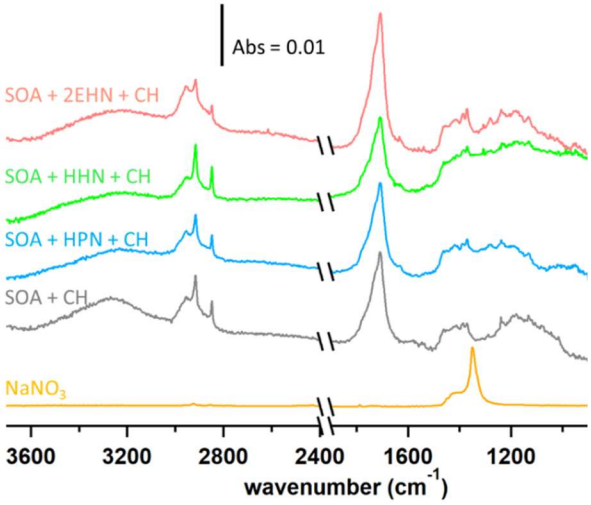

Figure 2.15: ATR-FTIR spectra for impacted particles alone, and particles formed in the presence of 2EHN, HPN or HHN in the flow reactor with CH as an OH scavenger (series D). Also shown is the spectrum for 10 μL of a 0.52 M solution of $NaNO_3$ deposited on the crystal with the solvent subsequently evaporated. The $NaNO_3$ spectrum has been multiplied by a factor of 0.1. The region between 2500 – 2000 cm^{-1} is not shown due to variations in the CO_2 (g) in the sampling compartment.

To quantify the amount of organic nitrate in the particles and to compare to the FTIR data, the AMS mass concentrations of NO^+ and NO_2^+ were expressed as moles -ONO_2 per liter of SOA. Thus, the mass loading (μg m^{-3}) of NO^+ and NO_2^+ were converted using eq. (2.9) into moles m^{-3} air of organic nitrate using the molecular weights of NO^+ and NO_2^+ (30 and 46 g $mole^{-1}$, respectively), assuming that each organic nitrate has only one nitrate group which will give either an NO^+ or an NO_2^+ fragment. The mass concentration of SOA (μg m^{-3} air), represented by HROrg, is converted to volume concentration of SOA (L m^{-3} air) using its density ($\rho = 1.2 \times 10^3$ g L^{-1})[138] as shown in Equation 2.9:

$$\frac{\left[NO^+ \times \frac{1}{MW_{NO^+}}\right] + \left[NO_2^+ \times \frac{1}{MW_{NO_2^+}}\right]}{HROrg} \times \rho_{SOA} \times \frac{RIE_{Org}}{RIE_{Nit}} = \frac{\text{moles} - ONO_2}{\text{Volume SOA}} \qquad \text{Equation 2.9}$$

The default value for the relative ionization efficiency (RIE) of organics (1.4) was used for SOA, while an RIE of 1.0 was used for all organic nitrates, assuming their respective ionization efficiency is similar to that of inorganic nitrate as assumed by other researchers.[89] To calculate the partition coefficient, K, the moles $RONO_2$ per liter of SOA from Equation 2.9 was divided by the gas phase concentration in the flow reactor in moles $-ONO_2$ L^{-1} air (Equation 2.5). These concentrations were determined by measuring the concentration exiting the trap and factoring in the dilution into the flow reactor.

To examine changes in composition as a function of particle diameter, the high-resolution particle time-of-flight (HR-PToF) feature was used, which allows size-dependent composition analysis of specific fragments. The particle size distribution was separated into 12 evenly spaced bins between 157 and 822 nm vacuum aerodynamic diameter (D_{va}), and the high-resolution mass spectrum were collected up to *m/z* 120. The data for diameters < 157 nm and diameters >822 nm D_{va} were omitted due to the very small mass loading which caused large contributions from noise, and due to decreased lens transmission efficiency in these diameter ranges.[162]

2.11 FTIR Quantification for Incorporation During Growth

For Series D (incorporation *during growth*), the polydisperse particles were impacted at a total flow of 30 L min^{-1} for 10-30 min at the end of the reactor. The partition coefficient was then quantified using the $-ONO_2$ or -CN and carbonyl stretches as described above in Equation 2.6-Equation 2.8. Note that for this Series D, $[-ONO_2]_{SOA}$ and $[-CN]_{SOA}$ can include both the parent organic nitrate/nitrile and products from oxidation by OH when CH is not present.

2.12 Kinetics Modeling

A simplified mechanism for the ozonolysis of AP (Table 2.6) was run using Kintecus®[137] to evaluate the extent of OH chemistry in the experiments, as well as to determine the total concentration of AP oxidation products (hereafter referred to as product 1 (P1, a proxy for all low volatility ozonolysis products). In addition, the gas-phase product distribution was modeled for each reaction condition with OH scavenger using the Master Chemical Mechanism (MCM, http://mcm.york.ac.uk/) v3.3.1[163-165] and the AtChem box model web-based interface.[166] For further analysis into the distribution of dimers across the reaction conditions studied here, the mechanism was updated to include highly oxidized multifunctional organic compounds (HOM) and dimer formation, as well as RO_2 autoxidation, as described by Zhao *et al*.[167] The amount of AP and ozone reacted that was predicted by the MCM and the simplified mechanism run using Kintecus® agreed within 2%.

Table 2.6: A simplified reaction mechanism for the ozonolysis reaction in the presence of CH and the tracers, with the corresponding rate constants.

Reaction	k (cm^3 $molecule^{-1}$ s^{-1})[1, 131]
$AP + O_3 \rightarrow OH + RO_2$[a]	7.0×10^{-17}
$AP + O_3 \rightarrow Product1$[a]	1.7×10^{-17}
$AP + OH \rightarrow RO_2$	5.4×10^{-11}
$CH + OH \rightarrow Products$	7.2×10^{-12}
	Calculated from Group Contribution[135,b]
2EHN + OH → Products	6.3×10^{-12}
IBN + OH → Products	$(1.6 \pm 0.2) \times 10^{-12}$
NN + OH → Products	7.3×10^{-12}
VN + OH → Products	1.7×10^{-12}
HPN + OH → Products	$1.3^{c} \times 10^{-12}$ $2.1^{d} \times 10^{-12}$ Average[e] $= (1.6 \pm 0.5) \times 10^{-12}$
HHN + OH → Products	$4.2^{c} \times 10^{-12}$ $6.4^{d} \times 10^{-12}$ Average[e] $= (5.1 \pm 1.3) \times 10^{-12}$

[a] 80% of $AP + O_3$ gives OH radicals,[168-170] and 20% of $AP + O_3$ gives low volatility products capable of forming particles (all products lumped together as Product1). The total $AP + O_3$ rate constant is 8.7×10^{-17}.[1, 131]

[b]The OH rate constant for IBN is taken from Becker and Wirtz.[171]

[c]Hydroxy-terminated isomer

[d]Nitrate-terminated isomer

[e]Rate constants for HPN and HHN are weighted averages using the relative amounts of the two isomers. The ratio of the hydroxy-terminated to nitrate-terminated isomers in the pure liquid was ~2:1 for HPN and ~4:3 for HHN. Error bars are ±1σ.

2.13 Effective Net Uptake Coefficients

The relative number of collisions of a gas phase oxidized organic molecule relative to a gas phase organic nitrate molecule with the particle surface can lend insight into the burying mechanism as a function of changing gas phase concentrations and particle surface area using Equation 2.10:

$$\frac{N_{RONO2}}{N_{PSOA}} = \frac{\gamma_{RONO2} \times [RONO_2]_{gas} \times \sqrt{\frac{RT}{2\pi M_{RONO2}}} \times A_{SOA}}{\gamma_{PSOA} \times [P_{SOA}]_{gas} \times \sqrt{\frac{RT}{2\pi M_{PSOA}}} \times A_{SOA}} \qquad \text{Equation 2.10}$$

where N_{RONO2} and N_{PSOA} are the number of molecules of organic nitrate and molecules of P_{SOA} taken up per cm^3 air per second, respectively; γ is the effective uptake coefficient for each species; M is their respective molar mass; and A_{SOA} is the surface area concentration of the SOA from the size distribution measurements. The $\gamma_{PSOA} \times [P_{SOA}]_{gas}$ (molecules cm^{-3}) in Equation 2.10 represents the product molecules from AP ozonolysis taken up to form the SOA and is determined using the measured SOA mass loadings, following the conversion in Equation 2.11:

$$\gamma_{PSOA} \times [P_{SOA}]_{gas} = \frac{\mu g\ SOA}{m^3\ air} \times \frac{mole\ SOA}{200 \times 10^6\ \mu g} \times N_A \times \frac{m^3}{10^6\ cm^3} \qquad \text{Equation 2.11}$$

where N_A is Avogadro's number, and the SOA mass loading in $\mu g\ m^{-3}$ is measured as described above.

The ratio N_{RONO2}/N_{PSOA} can be determined as:

$$\frac{N_{RONO2}}{N_{PSOA}} = \frac{N_{RONO2}}{N_{SOA}} = \frac{RONO_2\ (moles)}{Volume\ SOA\ (L) \times d_{SOA}\left(\frac{g}{L}\right) \times \frac{1}{M_{SOA}\left(\frac{g}{mol}\right)}} \qquad \text{Equation 2.12}$$

where the moles $RONO_2$ per L SOA are determined experimentally from Equation 2.9 using HR-ToF-AMS, the density of SOA is taken as 1.2×10^3 g per L[138] and the SOA molecular weight assumed to be 200 g per mole.[141-143] The gas phase concentration of organic nitrate in the flow reactor ($[RONO_2]_{gas}$) is the measured concentration.

Chapter 3: Incorporation After Particle Growth: Uptake onto Thin Films of SOA and Model Substrates

3.1 Research Goals

The goal of the first part of this research is to examine the unreactive intermolecular interactions between the molecular probes and the condensed phase of impacted particles. Comparing the uptake of gas phase species with different physicochemical properties onto impacted SOA particles as well as various model substrates provides insight into these intermolecular interactions. Quantification of initial net uptake coefficients (γ) and equilibrium partition coefficients (K_A) allows insight into the interactions that govern how these gas phase species are taken up into organic particles in the atmosphere.

3.2 Results and Discussion

Figure 3.1 shows the ATR-FTIR spectra for the solid film substrates before exposure to the organic nitrates and after exposure to ~7 ppm HHN, ~160 ppm HPN, and ~190 ppm 2EHN. Note that the saturation vapor pressure of HHN is much lower than that of HPN or 2EHN, limiting the HHN concentration that can be generated in the gas phase. Despite the two orders of magnitude lower concentration, uptake of HHN is still clearly evident onto SOA formed with out an OH scavenger, SOA formed with 100 ppm CH as an OH scavenger, PA and PEA. As seen in the figure, there was no observed uptake onto TC. There was slight uptake onto the Ge crystal itself for all three organic nitrates, but it was smaller than with organic material present on the crystal.

The lack of detectable uptake of all the organic nitrates on TC is not surprising. With the absence of polar interactions or hydrogen-bonding between the gas and the hydrocarbon surface, the dispersion forces may simply be too weak to result in any significant uptake onto the TC (the terminology used here is "van der Waals' interactions" for all weak non-covalent forces, including hydrogen-bonding, and "dispersion interactions" is used specifically for forces due to induced dipoles).[172] In contrast, there was significant uptake observed for the organic nitrates onto PA, PEA, and SOA.

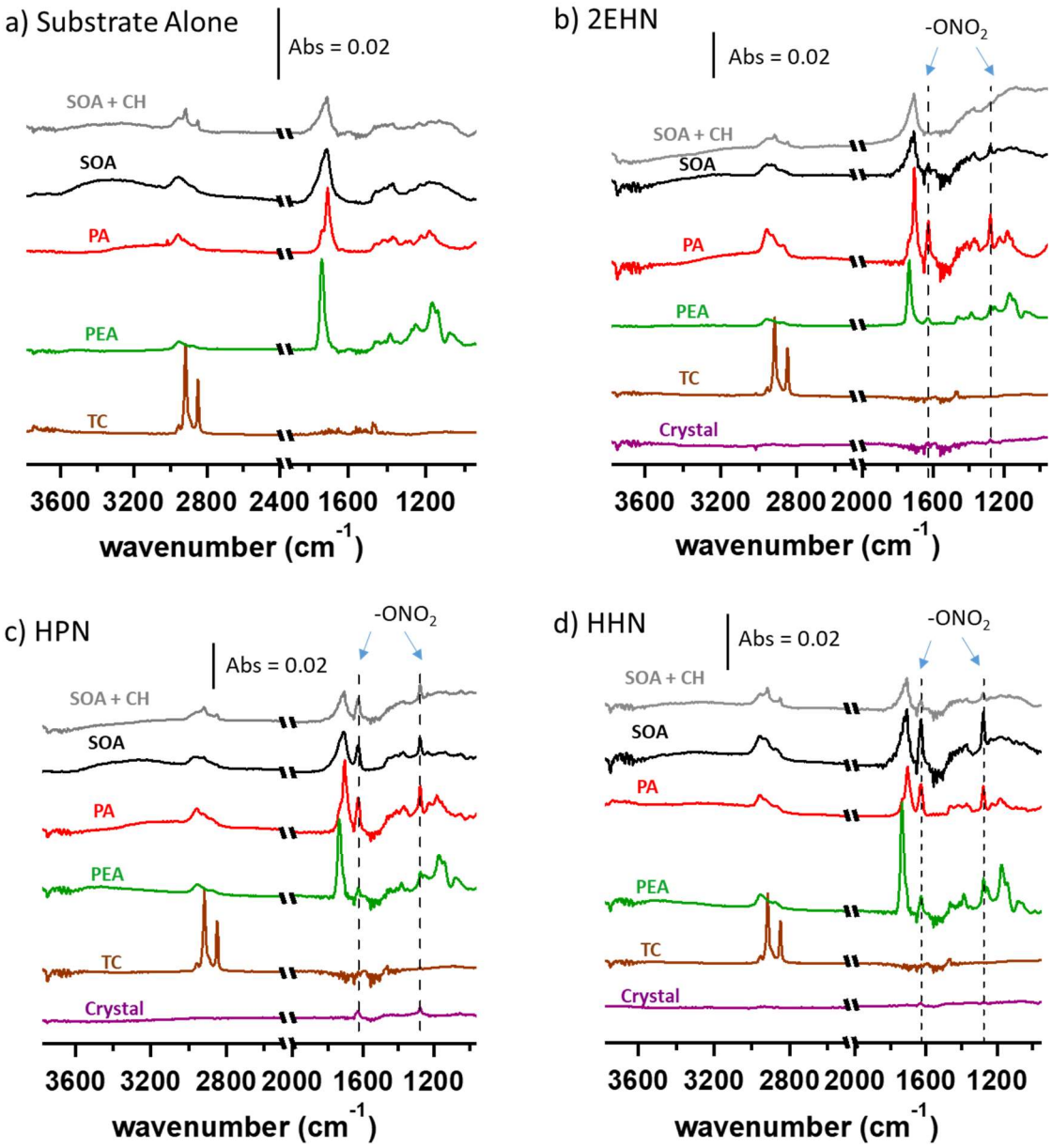

Figure 3.1: ATR- FTIR spectra for a) SOA formed with 100 ppm CH as an OH scavenger, SOA formed with no OH scavenger, PA, PEA, and TC alone, and b) after exposure to gaseous HHN (7 ppm), c) after exposure to gaseous HPN (160 ppm) , and d) after exposure to gaseous 2EHN (190 ppm) once equilibrium was reached (450-1050 seconds), as well as the spectra for exposure of the clean crystal to the organic nitrate. All TC spectra were scaled by a factor of 0.25, and all PEA spectra by a factor of 0.5 to display them on the same scale as the other spectra for clarity. Dashed lines indicate the $–ONO_2$ signals characteristic of organic nitrates. The region between 2500-2000 cm^{-1} is not shown due to CO_2 (g) variation in the purge air.

Figure 3.2 shows typical data for the time-dependent uptake of the three organic nitrates on SOA, SOA + CH, PA, and PEA respectively, in units of molecules cm^{-2} calculated by dividing the absorbance by the absorption cross section (Table 2.3). The curves for SOA, PA, and PEA are best fits from the kinetic multilayer model of gas-particle interactions in aerosols and clouds (KM-GAP) model,[173] discussed in detail below, while the curve for SOA + CH is a best fit to guide the eye. In all cases, there is a rapid initial uptake which then rises to a plateau, at which point there is no further net uptake. The concentrations of the organic nitrates in the films are significant, reaching as high as 3×10^{16} molecules cm^{-2} for HHN on PA. The amount taken up is much larger than a monolayer (~10^{14} molecules cm^{-2}), which suggests either a) that the organic nitrates adsorbed and produced a multilayer film along the surface approximately 100 monolayers thick, or b) that the organic nitrates are not simply adsorbed onto the surface but are penetrating and diffusing throughout the organic film. The former seems unlikely, and diffusion through the organic films is feasible given the timescales of the experiments and estimated thicknesses of the films. As discussed below, this is also supported by relatively slow desorption of the nitrates out of the film. Upon replacing the air stream containing gas phase tracer with that of clean dry air for desorption (~1100 seconds), the organic nitrate signal decreased until it was below the detection limit of the IR beam. This is an indication that the process is non-reactive and reversible, and that any condensed-phase chemistry of these species within the films is likely not fast enough to significantly contribute on these timescales.

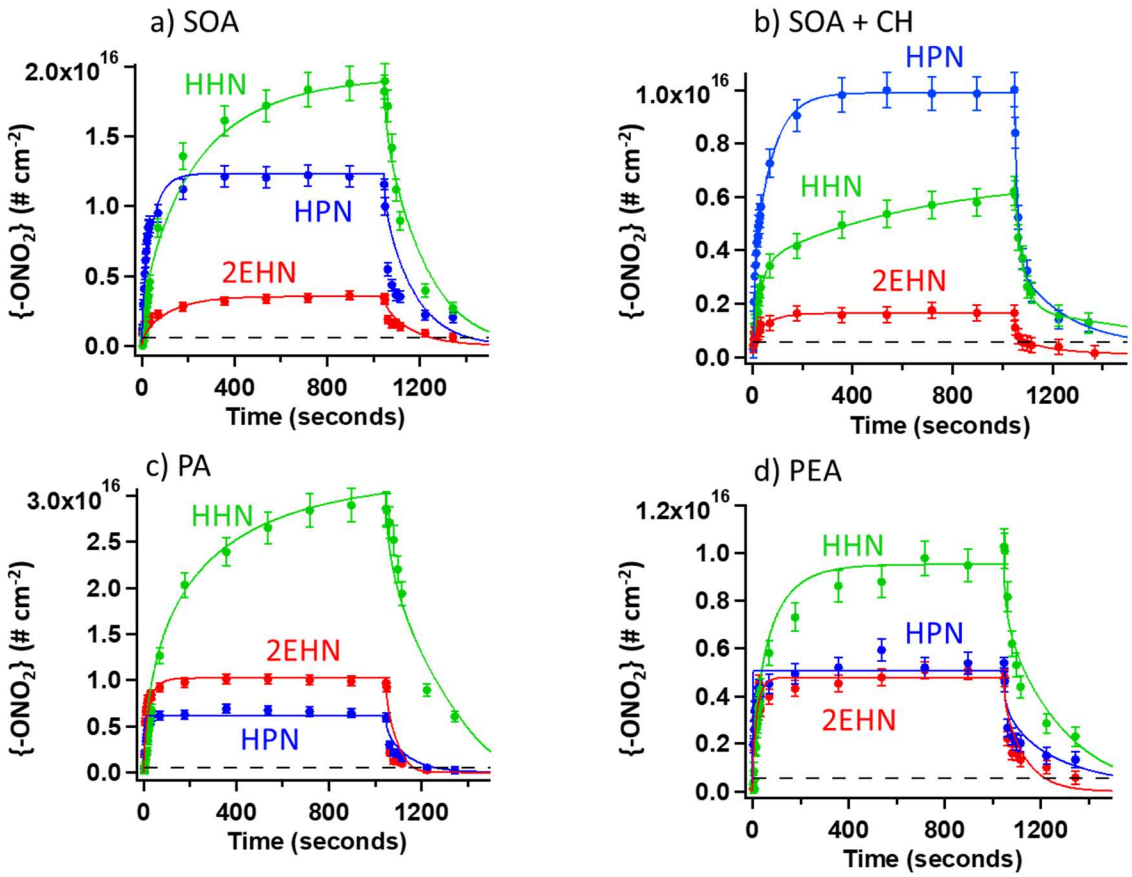

Figure 3.2: Concentrations of organic nitrates in molecules $-ONO_2$ cm^{-2} after exposure of (a) SOA, (b) SOA formed in the presence of CH, (c) PA and (d) PEA to gaseous HHN (7 ppm), HPN (160 ppm), and 2EHN (190 ppm). The dashed black line indicates the experimentally-determined limit of detection for the nitrates. Solid lines are best fits from the KM-GAP model with the exception of SOA formed in the presence of CH, which is a best fit to guide the eye. Error bars are $\pm 2\sigma$ on the experimental data points determined from the uncertainty in the measured absorption cross section of HHN, HPN and 2EHN.

Net Uptake Coefficients

From the initial rapid uptake, a net uptake coefficient γ can be obtained. These are summarized in Table 3.1 and shown in Figure 3.3. In the framework proposed by Pöschl, Rudich, and Ammann[40] and Kolb *et al.*,[39] these would be equivalent to bulk accommodation coefficients (α_b), because the nitrate in the entire film is interrogated by IR. In the application of

the KM-GAP model discussed below, the surface mass accommodation coefficients (α_s) were taken to be one, and diffusion of the gas to the surface is not limiting under our conditions.

Table 3.1: Uptake coefficients (γ) for all three organic nitrates into thin films of particles from the ozonolysis of α-pinene, particles from the ozonolysis of α-pinene (AP) with 100 ppm cyclohexane (CH) as an OH scavenger, PA, and PEA.

	Average Uptake Coefficient[a] (γ)		
Substrates	2EHN	HPN	HHN
SOA (no CH)	$(6.6 \pm 3.1) \times 10^{-6}$	$(1.6 \pm 0.4) \times 10^{-5}$	$(1.8 \pm 0.1) \times 10^{-4}$
SOA (with CH)	$(2.6 \pm 1.0) \times 10^{-6}$	$(1.7 \pm 0.9) \times 10^{-5}$	$(9.4 \pm 2.1) \times 10^{-5}$
PA	$(2.3 \pm 1.2) \times 10^{-5}$	$(2.0 \pm 1.1) \times 10^{-5}$	$(1.6 \pm 0.7) \times 10^{-4}$
PEA	$(1.3 \pm 0.2) \times 10^{-5}$	$(7.7 \pm 3.4) \times 10^{-6}$	$(1.9 \pm 0.5) \times 10^{-4}$

[a] Error bars are ±1σ from the average of three experiments.

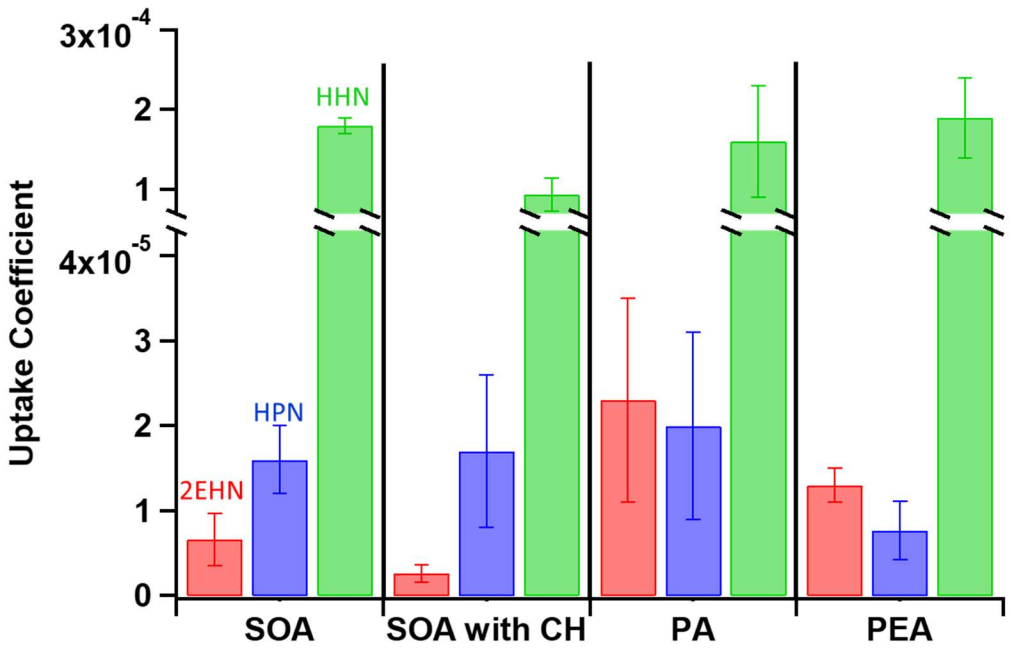

Figure 3.3: Initial uptake coefficients for all organic nitrates into SOA from the ozonolysis of α-pinene, SOA from the ozonolysis of α-pinene with CH as an OH scavenger, PA, and PEA. Error bars are ±1σ from the average of multiple experiments for each organic nitrate.

The limited number of data points in this initial time frame gives rise to significant error bars, and may underestimate the rate of uptake as the films begin to take up the organic nitrate and some re-evaporation from the film occurs. As discussed earlier, the gas-phase organic nitrate concentrations may be overestimated, and the substrate films may not be homogeneous in thickness, which would also result in underestimates of the uptake coefficients. However, this approach should provide initial estimates of relative rates for the different organic nitrate-substrate combinations.

As seen in Figure 3.3, HHN has by far the largest net uptake coefficient for all three substrates, with values over an order of magnitude higher than those of HPN and 2EHN. This is

not surprising, as HHN has the largest capacity for intermolecular interactions, possessing both the additional hydroxyl group for hydrogen bonding and the longer carbon backbone for dispersion interactions. In sharp contrast, uptake of HHN is minimal on TC as well as on the clean crystal (Figure 3.1). Hence, hydrogen bonding and other van der Waals' forces with specific functional groups on the substrates must play a significant role to anchor the incoming gas phase molecule onto PA, PEA and SOA.

For 2EHN and HHN, the uptake coefficient decreased by a factor of ~2 when the SOA was formed in the presence of an OH scavenger, whereas the uptake coefficient for HPN remained constant for the two conditions. These trends are similar to those seen for the partition coefficients for the 2EHN, HPN and HHN into the SOA, discussed in detail later. For a given organic nitrate, having a similar trend for the uptake and partition coefficients indicates that the relative intermolecular interactions that drive uptake on the surface must be similar to those that drive solubility into the bulk. There are some composition differences between SOA formed with versus without the OH scavenger, discussed below, which give rise to the difference in uptake coefficient and partition coefficient for 2EHN and HHN.

These measured uptake coefficients are orders of magnitude less than one. This is reasonable given the range of previously reported uptake coefficients for both reactive and non-reactive uptake. For an example of reactive uptake, Fairhurst *et al.*[174-175] reported that for the uptake of various amines and ammonia with a series of solid dicarboxylic acids, net reactive uptake coefficients ranged from 0.7 to less than 10^{-6}. Additionally, a previous study by

Donaldson *et al.*[176] showed that the unreactive uptake of certain gases onto liquid organic films of oleic acid or squalene ranged from ~10^{-2} to less than 10^{-5}.

Calculations of the structures and binding energies for complexes of the nitrates with the substrates can lend insight into the forces that provide the initial anchor for the incoming nitrate. Binding energy calculations were carried out for complexes of one or two gas phase nitrate molecules (2EHN, HPN and HHN) with one PEA substrate subunit. While PEA has an average molecular weight of 1000 g mol^{-1} and thus contains 5-6 subunits, one PEA subunit was used to represent the substrate due to computational constraints.

Figure 3.4 shows the optimized structures for one nitrate molecule interacting with one PEA subunit for all the organic nitrates. The binding energies are summarized in Table 3.2. As seen in Figure 3.4a, 2EHN is positioned horizontally over the PEA subunit where there are weaker dispersion forces between its alkyl chain and that of PEA, whereas HPN forms one hydrogen bond with the carbonyl group on the PEA (Figure 3.4b). This is consistent with binding energies of 11.8 kcal mol^{-1} and 13.5 kcal mol^{-1} for 2EHN and HPN, respectively. For HPN to be taken up, the HPN molecule must find a carbonyl with which to form a hydrogen bond, which introduces a steric component to the uptake. The interaction of 2EHN with the surface through dispersion interactions is less sterically demanding. Thus, although the binding energy for 2EHN is smaller, the higher net uptake coefficient for 2EHN is consistent with the lack of a significant steric effect. Like HPN, HHN is also able to form a hydrogen bond with

PEA to anchor it to the substrate molecule (Figure 3.4c) with a binding energy of 14.5 kcal mol^{-1}, and it prefers to orient itself vertically with the carbon tail away from the PEA.

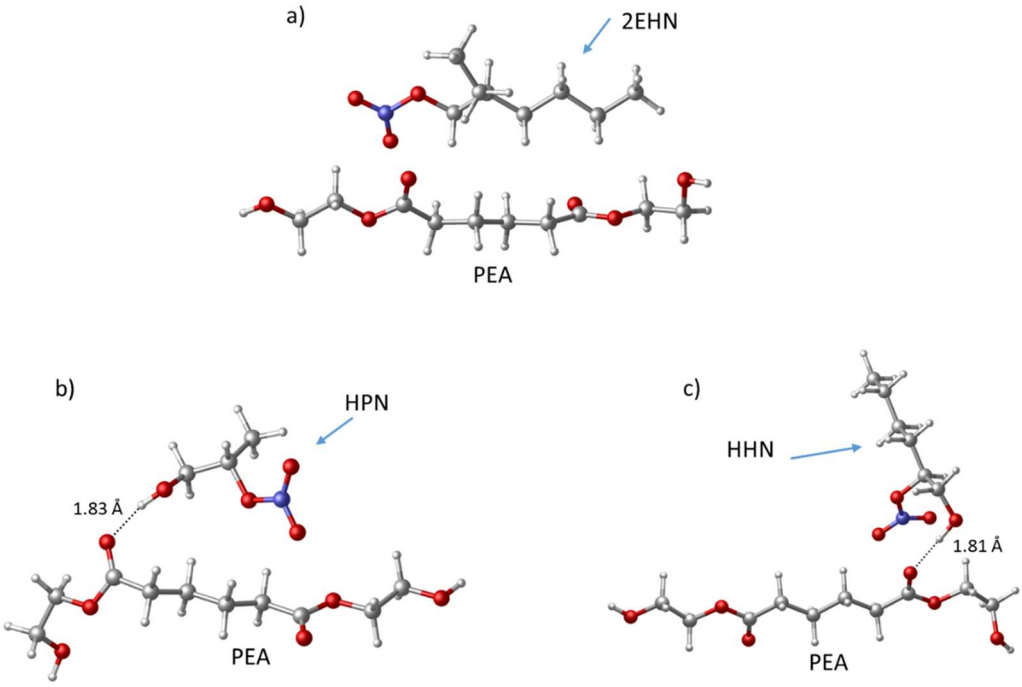

Figure 3.4: Optimized structures for one organic nitrate molecule binding with one PEA subunit for a) 2EHN, b) HPN, and c) HHN. Calculations were performed by Dr. Estefania Rossich Molina and Dr. R. Benny Gerber. Figure adapted from Vander Wall *et al*.[177]

Table 3.2: Binding energies (kcal mol^{-1}) for the optimized structures of either one or two organic nitrate molecules binding with one subunit of PEA, calculated at the B3LYP-D3/6-31+G(d) level of theory. Calculations were performed by Dr. Estefania Rossich Molina and Dr. R. Benny Gerber.

	Binding energy (kcal mol^{-1})		
	HPN	2EHN	HHN
$RONO_2$: PEA	13.5	11.8	14.5
2 $RONO_2$: PEA	18.5	18.0	30.0

Further insight was gained by carrying out calculations for *two* organic nitrate molecules interacting with the PEA subunit. Figure 3.5 shows the optimized structures. The binding energies for these structures are also found in Table 3.2. The binding energies for 2EHN and HPN are similar (18.0 and 18.5 kcal mol^{-1}, respectively), and are higher than for one organic nitrate on one PEA subunit. The binding energy for two HHN molecules with one PEA subunit is much higher, 30.0 kcal mol^{-1}. This is due to a contribution from hydrogen bonding between the HHN nitrate functional group and the PEA terminal hydroxyl group. Since only one PEA subunit was used to represent the substrate, and the polymer itself does not have repeating internal hydroxyl groups, the importance of binding to the terminal hydroxyl and the binding energies may be overestimated. However, the structure in Figure 3.5 shows both HHN molecules assemble vertically, indicating the HHN molecules may be able to assemble along the surface of PEA similar to a self-assembled monolayer, allowing for some dispersive interactions between the HHN carbon backbones. This is consistent with the higher uptake coefficient value for HHN.

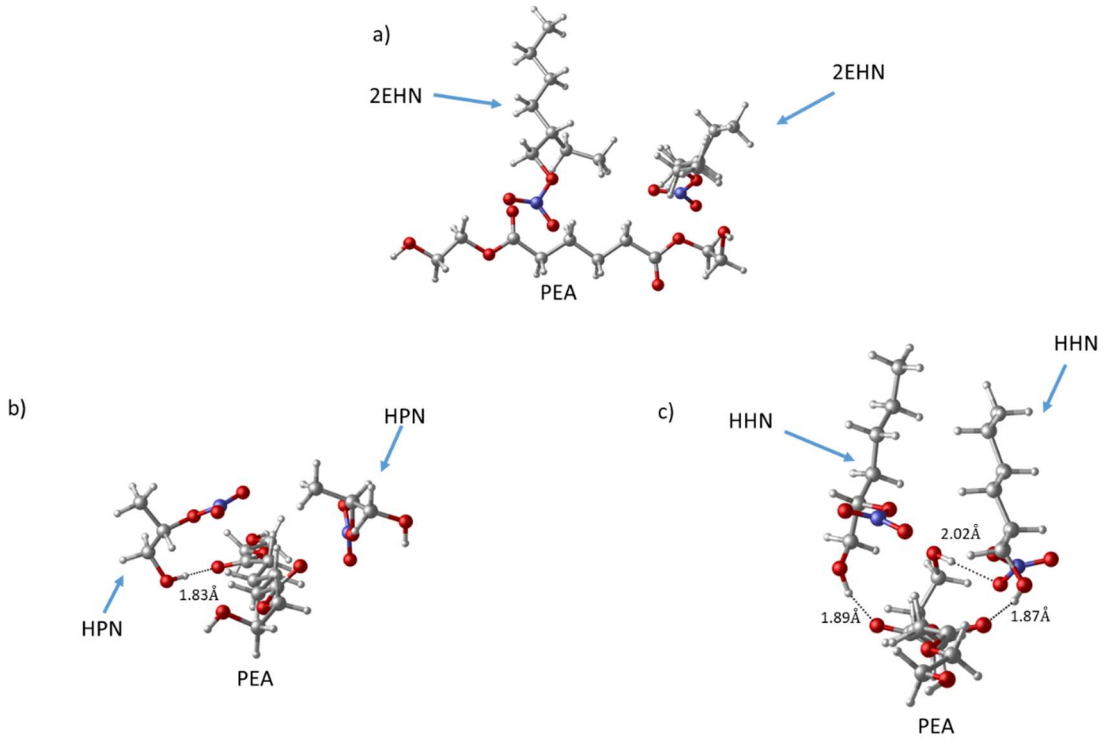

Figure 3.5: Optimized structures for two organic nitrate molecule binding with one PEA subunit for a) 2EHN, b) HPN, and c) HHN. Calculations were performed by Dr. Estefania Rossich Molina and Dr. R. Benny Gerber. Figure adapted from Vander Wall *et al*.[177]

Partition Coefficients and Mole Ratios of Organic Nitrates

From the plateau regions of Figure 3.2, mole ratios were calculated for each organic nitrate-substrate combination. Table 3.3 shows the average ratio of moles of $-ONO_2$ to moles of C=O after exposing SOA, PA, and PEA to each organic nitrate for ~1000 seconds. The mole ratios show large amounts of organic nitrate, up to 0.59 for the case of HHN on PA. These large ratios of nitrate to substrate suggest that the nitrate is not simply adsorbing onto the surface of the solid films, but instead is penetrating and diffusing into the films as discussed above.

Table 3.3: Average mole ratios of $-ONO_2$ to -C=O for PA, PEA, and SOA formed either with or without 100 ppm CH as an OH scavenger, after exposure to each organic nitrate for 1047 seconds, at which point equilibrium has been reached.

	Mole Ratio[a]		
Substrates	2EHN	HPN	HHN
SOA (no CH)	0.088 ± 0.007	0.55 ± 0.29	0.36 ± 0.06
SOA (with CH)	0.022 ± 0.014	0.35 ± 0.19	0.15 ± 0.03
PA	0.24 ± 0.12	0.27 ± 0.12	0.59 ± 0.16
PEA	0.046 ± 0.006	0.077 ± 0.031	0.12 ± 0.04

[a] Error bars are ± 1σ from the average of at least three experiments.

Partition coefficients (K_A) were calculated as described above and are summarized in Table 3.4. As shown in the table, HHN has the largest partition coefficient (i.e., the largest solubility), with values up to two orders of magnitude larger than the other organic nitrates. Additionally, the K_A values for HHN exhibit a clear trend across the substrates, with $K^{PA} > K^{SOA} > K^{SOA+CH} \sim K^{PEA}$. This trend for 2EHN is similar, with $K^{PA} > K^{SOA} > K^{PEA} > K^{SOA+CH}$, while the trend for HPN shows $K^{SOA} \sim K^{SOA+CH} \sim K^{PA} > K^{PEA}$.

Table 3.4: Partition coefficients (K_A) calculated for the uptake of the organic nitrates into thin films of particles formed either with or without CH, and into thin films of PA and PEA. Error bars are ±1σ from the average of three experiments.

	Average Partition Coefficient (K_A)		
Substrates	2EHN	HPN	HHN
SOA (no CH)	$(1.1 \pm 0.1) \times 10^5$	$(5.4 \pm 2.0) \times 10^5$	$(9.0 \pm 1.0) \times 10^6$
SOA (with CH)	$(3.2 \pm 1.5) \times 10^4$	$(4.4 \pm 2.0) \times 10^5$	$(4.9 \pm 0.8) \times 10^6$
PA	$(2.4 \pm 0.8) \times 10^5$	$(3.9 \pm 1.1) \times 10^5$	$(1.2 \pm 0.1) \times 10^7$
PEA	$(7.4 \pm 0.8) \times 10^4$	$(1.5 \pm 0.6) \times 10^5$	$(4.3 \pm 0.6) \times 10^6$

The differences in their intermolecular interactions provide some insight into these trends. In the case of HPN, H-bonding will dominate, as it can both donate and accept H-bonds. In contrast, dispersion forces will likely dominate for 2EHN with its larger alkyl chain. The crystal structure of PA exhibits a head-to-tail arrangement with the acidic hydrogen of one molecule hydrogen bonding to the ketone carbonyl of the next molecule.[178] Although the PA in the film may no longer be in the crystalline form, the FTIR spectrum for the PA film indicates the carbonyl-containing groups are hydrogen-bonded (Figure 2.13), which is similar to the crystal structure. The acid carbonyl does not participate in the self-hydrogen bonding network, and therefore can accept hydrogen bonds from other molecules, for example from HPN. However, PA also has a significant hydrocarbon backbone, allowing the dispersion forces to contribute as well. The relative strengths of these interactions are apparently similar enough to cause 2EHN and HPN to have similar solubilities in PA.

For SOA, the partition coefficient for HPN is about a factor of five larger than for 2EHN, indicating stronger attractive forces between the components of SOA and HPN. SOA is an amorphous mixture containing many different acids and polar functionalities that are available to hydrogen bond to the -OH group of HPN as well as its $–ONO_2$ group.[141] The additional hydrogen-bonding capacity of HPN appears to play a significant role in enhancing its solubility in SOA compared to the solubility of 2EHN.

To further examine the role of these intermolecular interactions in the partitioning and solubility in SOA, the uptake of the organic nitrile NN (whose vapor pressure of 1.3×10^{-4} atm is similar to that of 2EHN, Table 2.1 and Table 2.2) was quantified. Figure 3.6a shows an ATR-FTIR spectra for impacted SOA particles alone and a spectra after exposure to ~100 ppm of gas phase NN upon reaching equilibrium (after ~4000 seconds). Figure 3.6b shows the time profile for the nitrile functional group signal (-CN) at 2250 cm^{-1} after exposure of the SOA to ~100 ppm NN, and the subsequent desorption where the NN air stream was replaced with clean, dry air after ~4000 seconds. Initial uptake coefficients were not quantified for the uptake of NN as the -CN signal took minutes to rise above the limit of detection, likely due to the smaller absorption cross section for NN (Table 2.4). From the equilibrium plateau, the partition coefficient was quantified as described previously using the -CN functional group to quantify NN and the carbonyl to quantify the SOA, and was found to be $(4.0 \pm 0.2) \times 10^5$ ($\pm 1\sigma$). This partition coefficient is larger than that of 2EHN and about equal to that of HPN, but smaller than that of HHN. NN has a C_9 linear hydrocarbon chain, longer than that of any of the organic nitrates. In addition, the C≡ N bond of nitrile functional groups is known to be quite polar, with a bond dipole moment larger than that of a C=O for a carbonyl or the O-H for a hydroxyl group.[179] The

increased dispersion interactions must then play a role in the solubility of NN when compared to HPN, which has the smallest hydrocarbon tail, and 2EHN which has a branched hydrocarbon tail. However, while NN's dispersion interactions from the hydrocarbon tail and the polarity of the nitrile functional group result in a larger solubility than 2EHN and a comparable solubility to HPN, the solubility of NN is much smaller than that of HHN. HHN has both an increased hydrogen-bonding capacity due to being a hydroxy-nitrate and a C_6 linear hydrocarbon tail. These factors combined result in HHN having the highest partition coefficient/largest solubility in the SOA of the studied molecules.

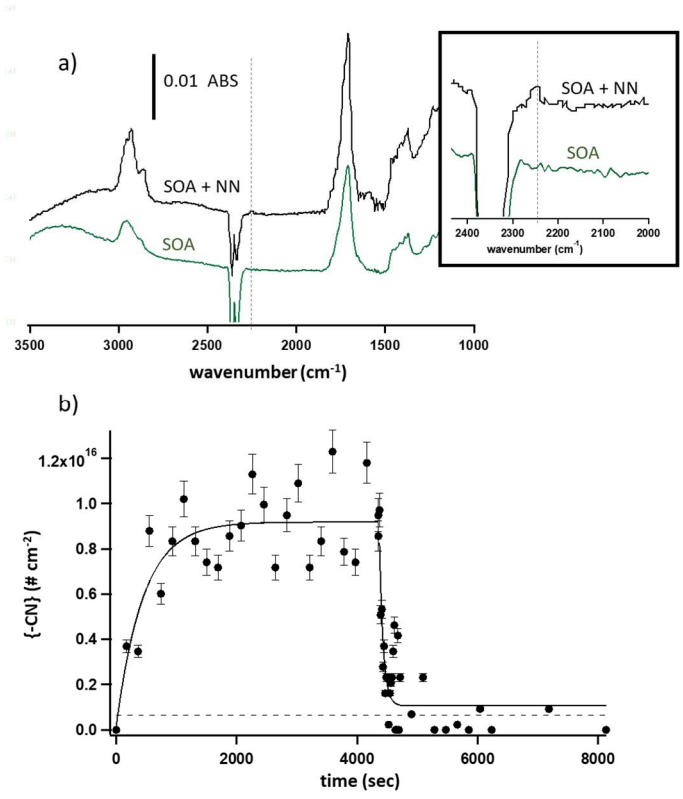

Figure 3.6: a) Typical ATR-FTIR spectra for SOA alone, and SOA after exposure to ~100 ppm NN (g) for approximately 4000 seconds. The inset shows the region from 2000-2400 cm^{-1}, with vertical dashed lines marking the 2250 cm^{-1} peak for the -CN. b) Concentration of NN in molecules –CN cm^{-2} after exposure of SOA without CH as an OH scavenger to ~100 ppm gas phase NN. Solid lines are best fits to guide the eye. Error bars are ± 2σ on the experimental data points determined from the uncertainty in the measured absorption cross section of NN. The dashed line shows the limit of detection.

It is important to note that vapor pressures are not necessarily a good measure of incorporation of the nitrates into the organic substrates. Thus, while 2EHN and HPN have similar vapor pressures (Table 2.1), the solubility of HPN in SOA formed in the absence or presence of an OH scavenger is about 5 to 14 times that of 2EHN, respectively. Similarly, the net uptake coefficient of 2EHN on PEA is about twice that of HPN.

Likewise, the O:C ratio is not a good predictor of uptake and partitioning. The O:C ratios for the organic nitrates are 0.67 for HHN, 0.38 for 2EHN, and 1.3 for HPN. The O:C ratios for PEA and SOA are similar: 0.52 and 0.50, respectively. However, the partition coefficients for all the organic nitrates are greater on SOA than on PEA. The O:C for PA is smaller (0.30), yet the partition coefficient of HHN is higher than in PEA and SOA. Similarly, the solubility of HPN is larger for PA relative to the PEA. This emphasizes the importance of intermolecular interactions both at the surface and in the bulk as fundamental.

For HPN, the partition coefficient on impacted particles formed without CH is not statistically different from that measured on impacted particles formed in the presence of CH, and is in excellent agreement with the air-octanol partition coefficient of $(4.2 \pm 0.3) \times 10^5$ reported by Treves *et al.*[180] This suggests that the magnitude of the HPN partitioning into the particles is unaffected by any composition changes in the SOA resulting from changes in the chemistry in the presence of the OH scavenger. It is interesting that the partition coefficients into SOA and octanol are similar and both are larger than into water,[181-182] suggesting that even

with the hydrogen bonding possibility to the alcohol group of HPN, dispersion forces between HPN and SOA are important as well.

For 2EHN and HHN, the partition coefficients decrease when the SOA is formed in the presence of the OH scavenger by factors of ~3 and ~2, respectively. This reduction in partitioning indicates decreased solubility of 2EHN and HHN into the bulk of the film, which could reflect differences in the SOA composition when CH is added to scavenge the OH. Table 3.5 shows the O:C and H:C ratios and the oxidation state of carbon (OS_c) determined by AMS.[183] Only very small changes in the bulk elemental composition were exhibited, consistent with previous reports for AP ozonolysis SOA formed with or without an OH scavenger.[184] However, this may simply reflect that functional group changes important in determining solubility are not detected in these bulk measurements. The percent change of a few major fragments by AMS when OH scavenger is present (Figure 3.7) shows that there are some changes in the SOA bulk composition. Why this results in changes in the partition coefficients for 2EHN and HHN but not for HPN is not clear, but it illustrates the need for a detailed molecular level understanding of the composition of SOA.[185-186]

Table 3.5: AMS elemental analysis for SOA formed without organic nitrates either with or without 100 ppm of CH as an OH scavenger (Series C) at 31 minutes reaction time. The oxidation state of carbon (OS_c) is determined by 2(O:C) – H:C.[183]

	SOA[a]	SOA + CH[a]
O:C	0.51 ± 0.02	0.48 ± 0.01
H:C	1.6 ± 0.01	1.6 ± 0.01
OS_c	-0.58 ± 0.05	-0.64 ± 0.03

[a]Error bars are ± 2σ

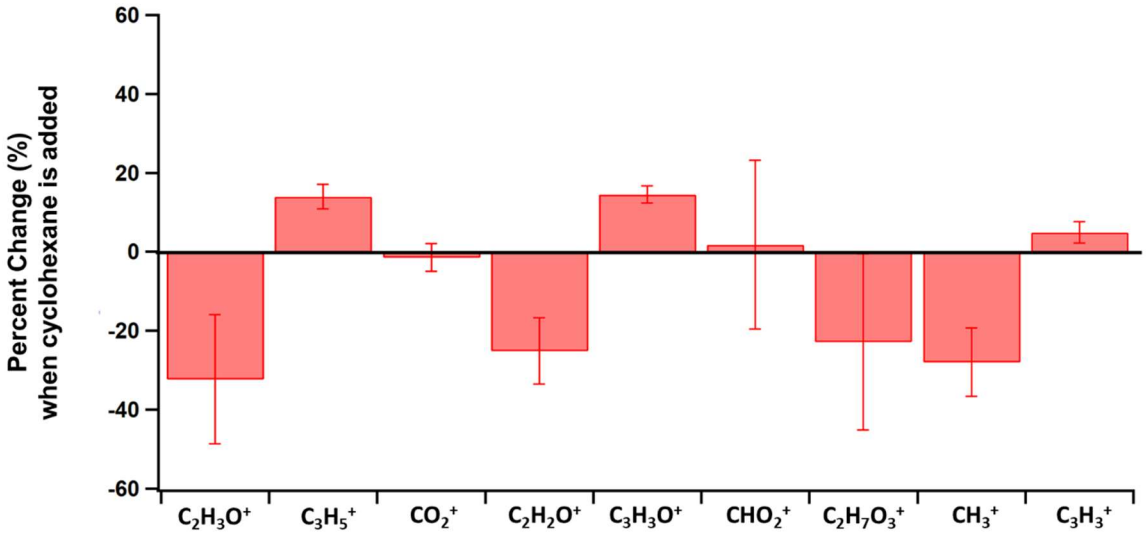

Figure 3.7: Percent change of some of the major fragments observed in the AMS spectra when CH is present compared to SOA formed without CH at 31 minutes reaction time. All fragments have been divided by HROrg to account for differences in the total mass loading. Negative values indicate that the fragment is less abundant when the OH is scavenged, while positive values indicate that the fragment is more abundant when the OH is scavenged. Error bars are ±2σ from the average of three experiments.

KM-GAP

The KM-GAP model[173] was used to investigate diffusion of organic nitrates through the organic film into the bulk. One observation is that bulk diffusion coefficients need to be treated as composition-dependent with Vignes equations to reproduce the entire data set, and a composition-independent constant diffusion coefficient scenario did not accurately capture the experimental data. An example is shown in Figure 3.8 for uptake of HHN on PA. Although both parameterizations fit the uptake of the organic nitrate onto the substrate reasonably well, a constant diffusion coefficient over-predicted how quickly HHN would diffuse back out of the PA film, whereas a composition-dependent diffusion coefficient was a better match to the experimental data (Figure 3.8, solid lines).

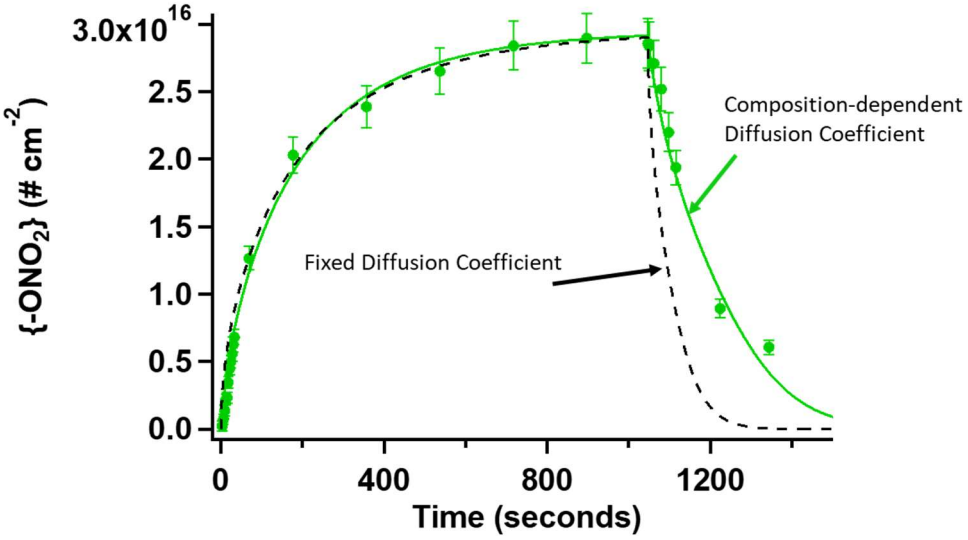

Figure 3.8: Uptake of HHN on PA. Points are the experimental data, where the error bars represent the uncertainty in the absorption cross section (±2σ). The solid line shows the prediction from KM-GAP using a changing composition-dependent diffusion coefficient scenario, while the dashed line shows the prediction using a constant composition-independent diffusion coefficient. Model calculations were performed by Dr. Pascale Lakey and Professor Manabu Shiraiwa. Figure adapted from Vander Wall *et al.*[177]

Figure 3.9 shows the KM-GAP predicted concentration gradients for the organic nitrates as a function of time. The y-axis of Figure 3.9 indicates the distance from the bottom of the film. These profiles indicate that the organic nitrate has indeed penetrated through the entirety of the film over the course of the experiments. Increases in the film thickness indicates that the organic film has swelled due to uptake of significant amounts of the organic nitrate. Figure 3.10 shows the accompanying changes in diffusion coefficients predicted by the KM-GAP model. The profiles indicate that there is a plasticizing effect upon incorporation of the organic nitrate, shown by the increases in diffusion coefficients for several nitrate-substrate systems.

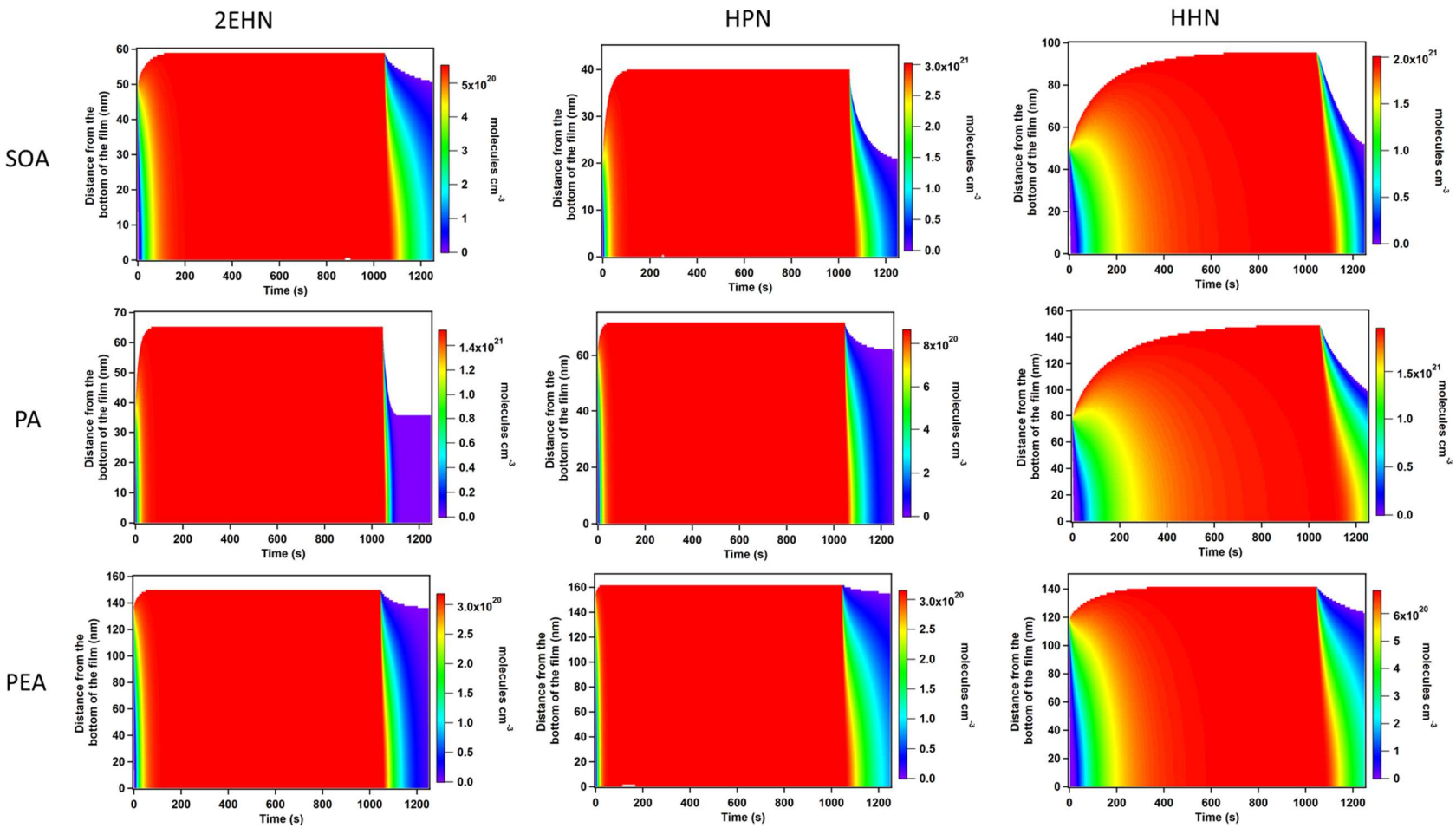

Figure 3.9: Contour plots for the organic nitrate concentrations in molecules cm^{-3} in the PA, PEA, and SOA films as a function of time and distance from the bottom of the film. Model calculations performed by Dr. Pascale Lakey and Professor Manabu Shiraiwa. Figure adapted from Vander Wall *et al.*[177]

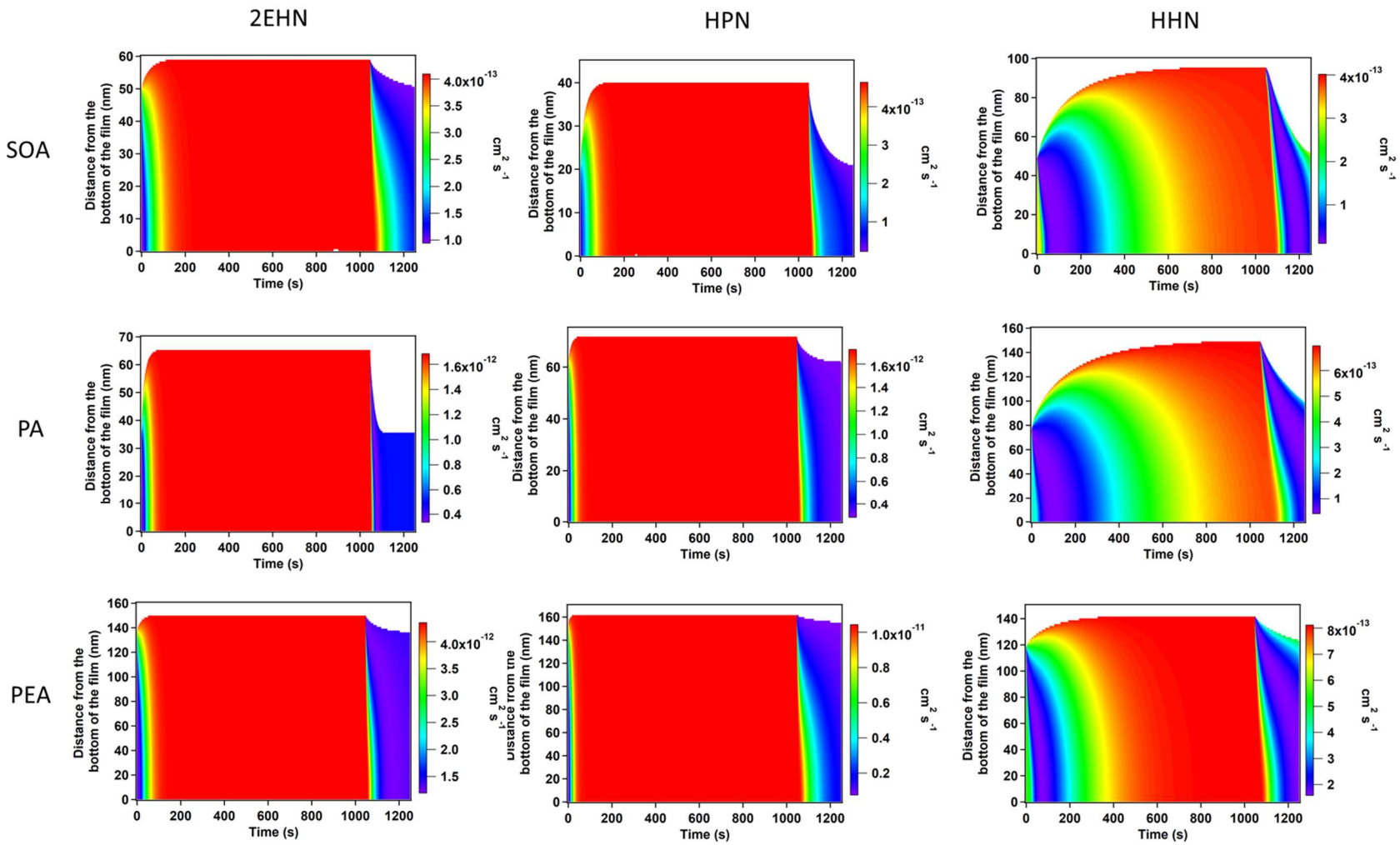

Figure 3.10: Contour plots showing the change in diffusion coefficient for the organic nitrate through PA, PEA, and SOA, as a function of time and distance from the bottom of the film. Model calculations performed by Dr. Pascale Lakey and Professor Manabu Shiraiwa. Figure adapted from Vander Wall *et al.*[177]

Furthermore, upon desorption, the removal of the organic nitrate from the topmost layers of the substrate results in decreasing diffusion coefficients in the upper layers of the film as they partially re-solidify without the organic nitrate. This results in a 'crusting' scenario with higher diffusion coefficients (and thus lower viscosities) in the lower layers of the film and a more viscous outer layer or 'crust' towards the surface. Figure 3.11 shows an expanded view as an example of the crusting on the surface of the film of SOA as 2EHN desorbs from the surface layer. This 'crusting' effect has been observed in previous work by Boyd *et al.*[80] on the evaporation kinetics of mixed limonene and β-pinene SOA, as well as by Pfrang *et al.*[79] on the chemical aging and transformation of multi-component organic aerosol particles.

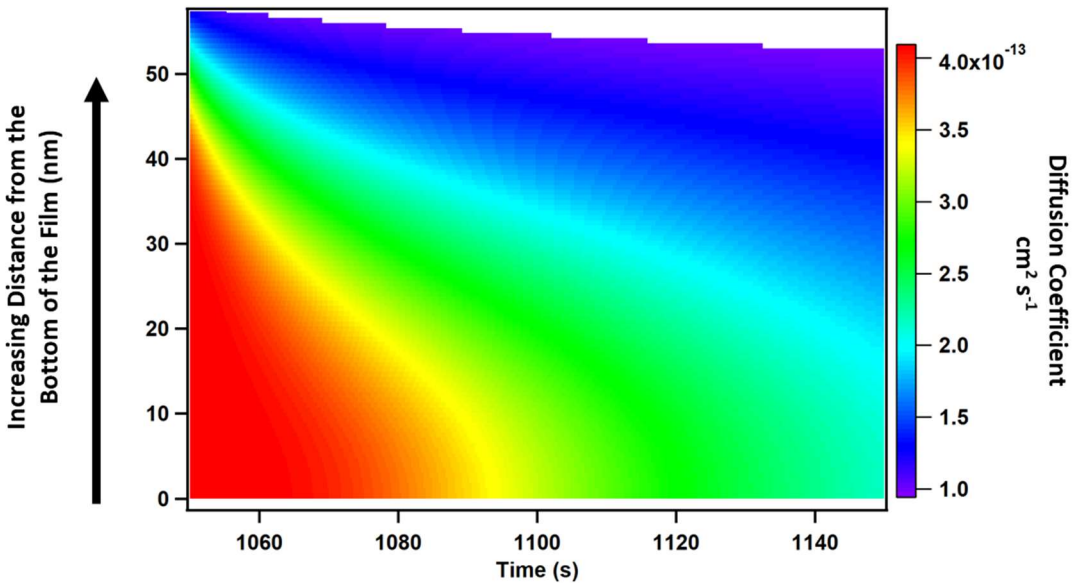

Figure 3.11: An expanded view of the diffusion coefficient contour plot for 2EHN on SOA. Model calculations performed by Dr. Pascale Lakey and Professor Manabu Shiraiwa. Figure adapted from Vander Wall *et al.*[177]

Comparison of Trends in Uptake Coefficients and Partitioning

HHN exhibits the largest partition and net uptake coefficients compared to the other organic nitrates, and also provides the most pronounced differences in uptake versus solubility

across the three substrates. Although both the uptake coefficient and partition coefficient for HHN decrease from SOA without OH scavenger to SOA with CH as an OH scavenger, the uptake coefficient for HHN is similar for SOA without OH scavenger, PA and PEA (Figure 3.3 and Table 3.1), while the solubility of HHN in PEA is lower than that in PA and SOA (Table 3.4). This suggests that the interactions between the nitrate and the substrate in the bulk are different than those controlling uptake at the substrate surface. Figure 3.12 compares the trends in net uptake and partition coefficients for the three nitrates on SOA either with or without OH scavenger. For SOA without OH scavenger, the uptake coefficient increases by a factor of 26 from 2EHN to HHN, whereas the partition coefficient increases by a factor of 83. For comparison, for SOA formed with an OH scavenger the uptake coefficient increases by a factor of 36 from 2EHN to HHN, and the partition coefficient increases by a factor of 154. Thus, the increase of the solubility is greater than that of the uptake coefficient, indicating that the relative contributions of the different attractive forces between the organic nitrates and the substrate must differ for the surface relative to those in the bulk. This is reasonable, given that the organic nitrates in the bulk are surrounded by neighboring molecules with opportunities to optimize the full range of van der Waals' interactions, including H-bonding, electrostatic interactions between partial charges, and dispersion interactions. On the other hand, an incoming gaseous organic nitrate molecule is affected only by available functional groups located on the surface, which will determine the nature and magnitude of the attractive forces. In the case of HHN on SOA, for example, if HHN is H-bonded to the surface in such a manner that the interactions of the alkyl chain with the surface are less than in the bulk where the HHN is engulfed by SOA components, relatively smaller uptake coefficients than expected based on the bulk behavior could result. Consistent with this and as discussed earlier, Figure 3.5 shows that HHN is

predicted to be oriented perpendicular to the PEA surface, minimizing dispersion forces between HHN and the surface PEA. This illustrates the importance of understanding both the nature of the surface and the nature of the gas in predicting uptake of gases into highly viscous particles, and hence their growth mechanisms in air.

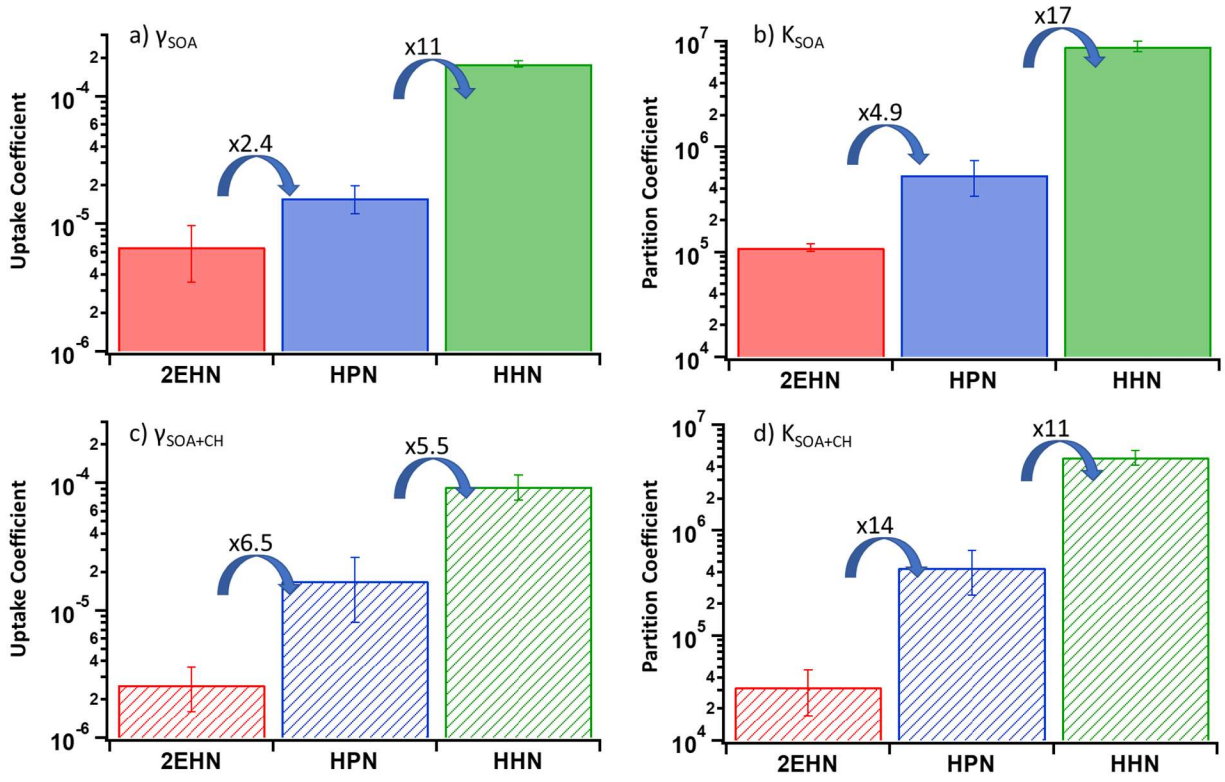

Figure 3.12: (a) Initial uptake coefficients and (b) equilibrium partition coefficients for all organic nitrates into SOA formed without OH scavenger, and (c) initial uptake coefficients and (d) equilibrium partition coefficients for all organic nitrates into SOA formed with 100 ppm CH as an OH scavenger. Error bars are ±1σ from the average of multiple experiments for each organic nitrate

3.3 Conclusions

Intermolecular interactions between gases and atmospheric particle surfaces play an important role in SOA particle growth. The present results indicate that a combination of polar and nonpolar interactions with the surface of SOA particles formed by the ozonolysis of α-

pinene play a role in gas uptake. However, the interactions determining this uptake are not necessarily the same as those occurring in the bulk, and hence the uptake coefficients and partition coefficients do not always correlate. Furthermore, trends in vapor pressure are also not necessarily good indicators of uptake or partitioning. Note that these uptake coefficients may be orders of magnitude less than one and will certainly depend on both the nature of the gas and the surface. Gas partitioning into these substrates can change the viscosity of the film and thus to increase the diffusion coefficients in the bulk. Furthermore, diffusion coefficients can decrease as the nitrates diffuse back out due to the formation of a crust near the surface. This has implications in the kinetics of condensed phase chemistry occurring in the bulk versus at the surface of particles. More knowledge of the nature of the surface of SOA particles, and how gaseous species interact with these surfaces, will allow for a better understanding of SOA particle growth to better predict their effects on Earth's climate.

Chapter 4: Incorporation During Particle Growth in an Aerosol Flow Reactor – The Role of the Hydroxyl Radical

4.1 Research Goals

Chapter 3 described the incorporation of the molecular probes into impacted particles and films of model substrates to examine the intermolecular interactions between the gas phase species and the condensed phase. This chapter focuses on the incorporation of the molecular probes *during* particle formation and growth in a flow reactor, with emphasis on the role of the hydroxyl radical chemistry. This provides a foundation for understanding experiments described in Chapter 5 when an OH scavenger is present.

4.2 Results and Discussion

The role of the hydroxyl radical in the incorporation of the molecular probes (or tracers) was examined *during* the particle formation and growth process (series C and D) in a large aerosol flow reactor using ATR-FTIR and HR-ToF-AMS. Figure 4.1a shows the ATR-FTIR spectra for impacted particles from AP ozonolysis alone (without organic nitrate or OH scavenger) and for particles formed in the presence of 2EHN, HPN, or HHN at 31 minutes reaction time. Figure 4.1b shows the ATR-FTIR spectra for the particles formed in the presence of an OH scavenger. While the organic nitrate peaks at 1630 cm^{-1} and 1280 cm^{-1} are seen in the spectrum when 2EHN is present during particle formation, there is much less organic nitrate after the addition of the OH scavenger. Similar results were obtained for SOA formed in the presence of HHN. For HPN, the organic nitrate signal was below the limit of detection by FTIR either with or without the OH scavenger.

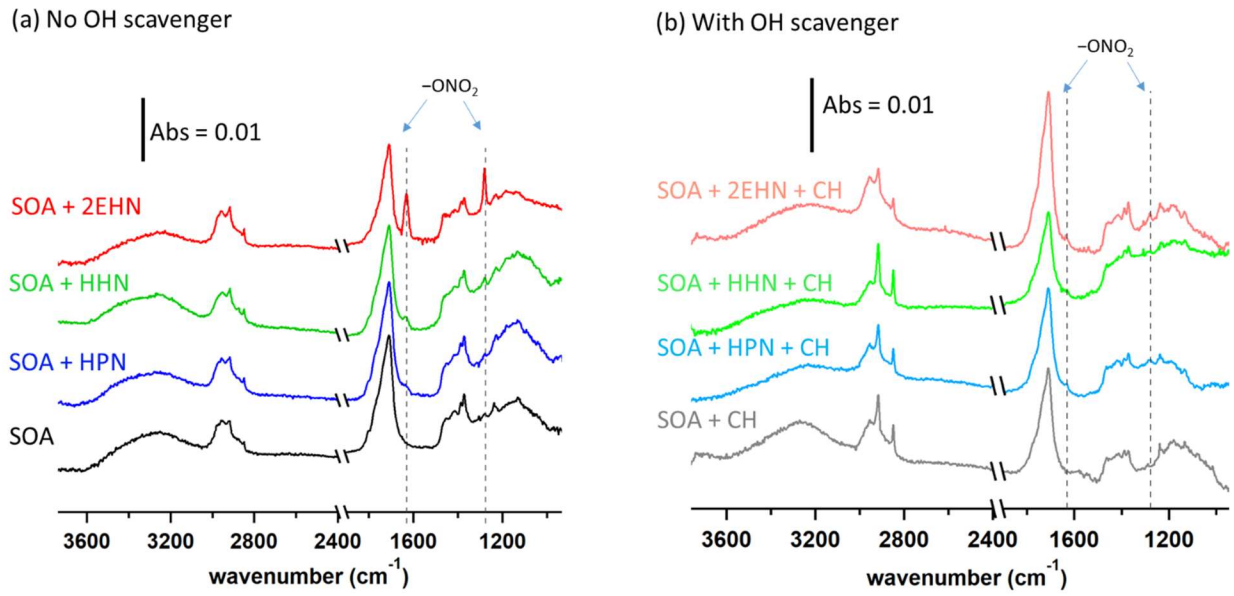

Figure 4.1: ATR-FTIR spectra for a) impacted particles alone and formed in the presence of 2EHN (5.6 ppm), HPN (4.7 ppm), or HHN (0.21 ppm) in the stainless steel flow reactor (Series D) without an OH scavenger, and b) impacted particles alone and formed in the presence of 2EHN, HPN or HHN at the same concentrations in the stainless steel flow reactor in the presence of CH as an OH scavenger (Series D). The region between 2500 – 2000 cm^{-1} is not shown due to variations in the CO_2 in the sampling compartment.

Comparison of the SOA itself formed either with or without CH shows some change in the -CH region (3000-2800 cm^{-1}). Although CH is too volatile to partition into the particle phase, some of its OH oxidation products may be taken up and contribute to the particle growth. Figure 4.2 shows the ATR-FTIR spectra for cyclohexanone and cyclohexanol, which are among the expected products from the CH + OH reaction.[187-189] This shows that the CH + OH products may be contributing to the changes seen in the particles formed in the presence of CH.

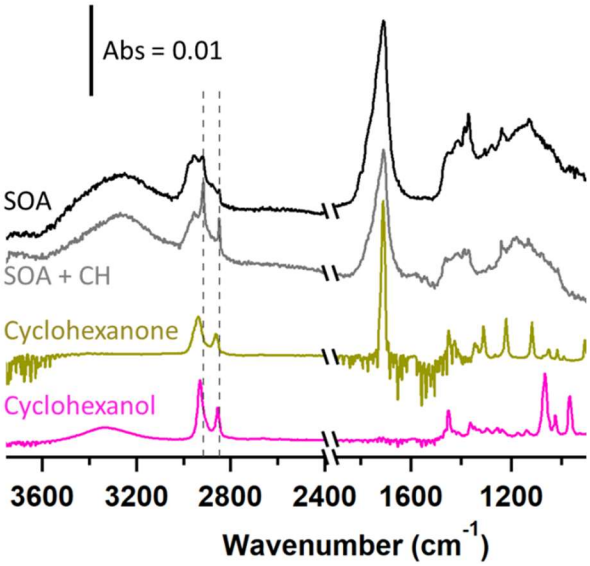

Figure 4.2: ATR-FTIR spectra for impacted SOA particles alone and SOA particles formed with CH as an OH scavenger. Also shown are the spectra for liquid cyclohexanone and cyclohexanol. The cyclohexanone and cyclohexanol spectra have been scaled by a factor of 0.1. The region between 2500 – 2000 cm^{-1} is not shown due to variations in the CO_2 in the sampling compartment. The dashed lines at 2915 and 2850 cm^{-1} are guides for the eye.

The incorporation of a series of organic nitrates and organic nitriles was examined in the absence of an OH scavenger. The ATR-FTIR spectra for SOA alone and formed in the presence of various gas phase concentrations of 2-ethylhexyl nitrate (2EHN), isobutyl nitrate (IBN), nonane nitrile (NN) and valeronitrile (VN) are shown in Figure 4.3. As seen in the spectra, the contribution of the $-ONO_2$ peaks at 1630 and 1280 cm^{-1} (Figure 4.3a and Figure 4.3b) and the -CN peak at ~2250 cm^{-1} (Figure 4.3c and Figure 4.3d) increases with the initial concentration of the gas phase tracer. Figure 4.4a shows the experimentally measured moles $-ONO_2$ or -CN per liter of SOA for these tracers as well as β-hydroxyhexyl nitrate (HHN) and β-hydroxypropyl nitrate (HPN), quantified as described in Equation 2.6-Equation 2.8. As expected, the contribution of the organic nitrate or nitrile to the particles increases with the concentration of the gas phase tracer.

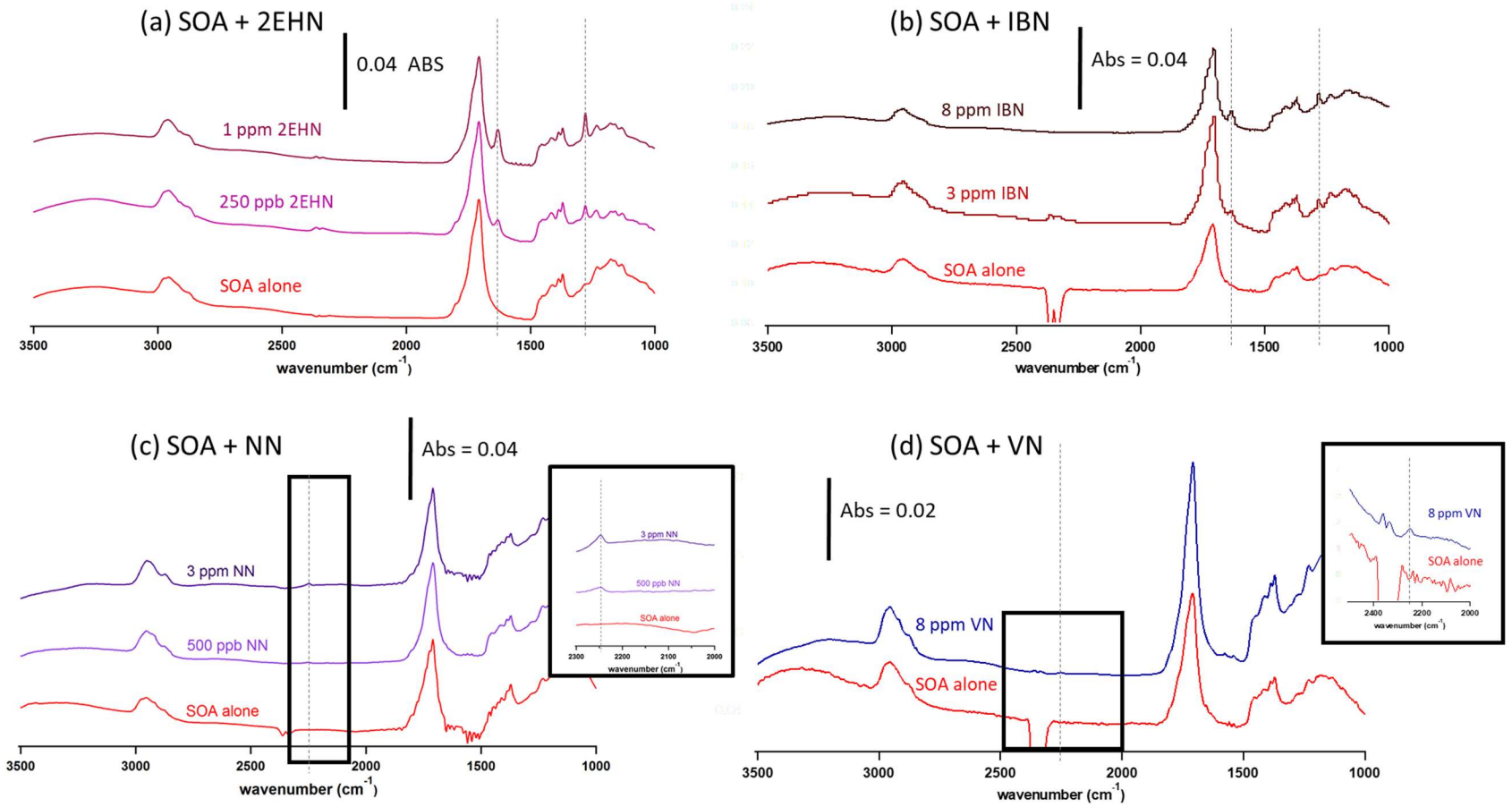

Figure 4.3: ATR-FTIR spectra for SOA formed from 250 ppb AP and 250 ppb O_3 alone in the absence of an OH scavenger, and formed in the presence of different concentrations of a) 2EHN (g), b) IBN (g), c) NN (g), and d) VN (g). The insets on c and d show the 2000-2500 cm^{-1} range for the absorption of the nitrile -C≡N stretch.

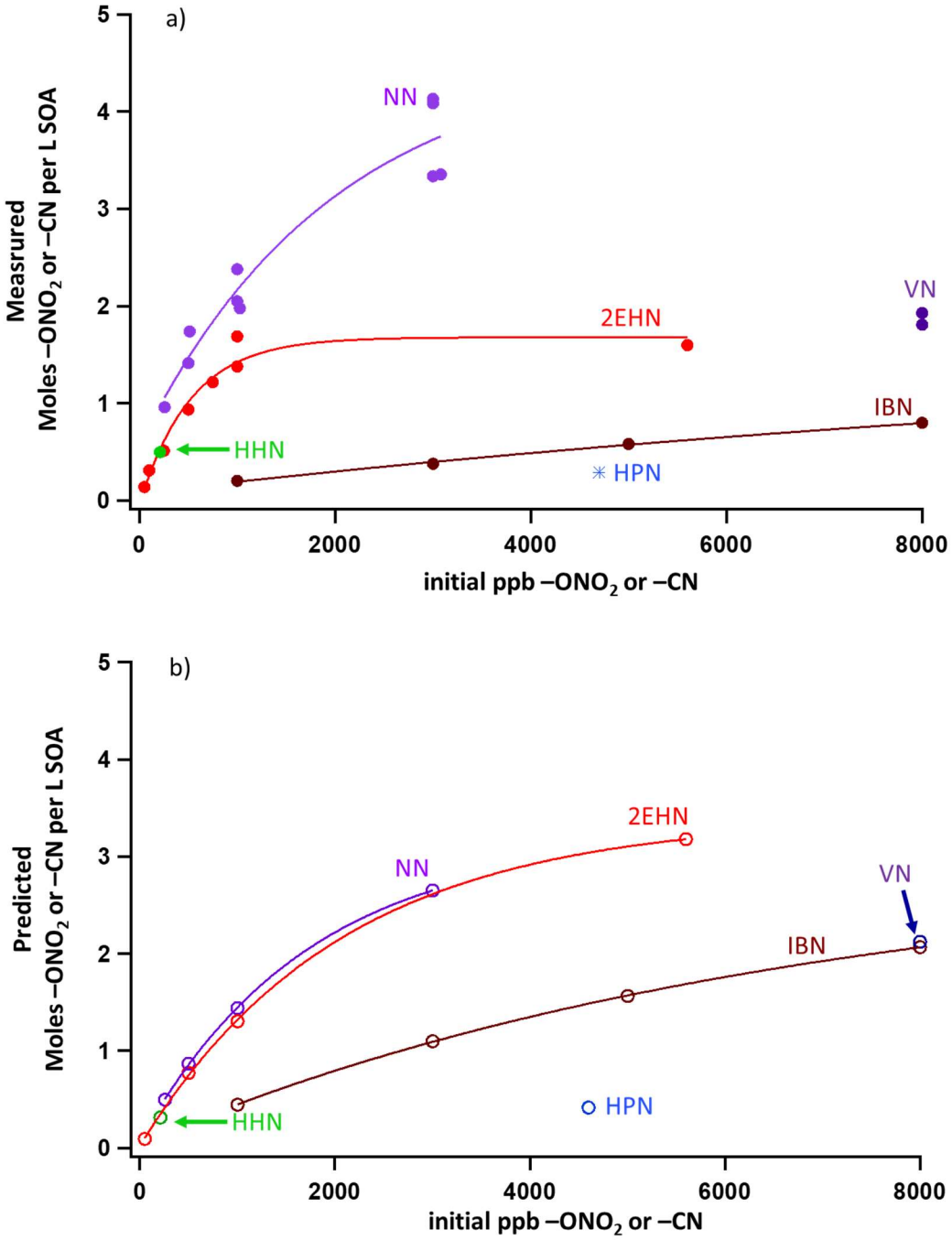

Figure 4.4: a) Experimentally measured moles -ONO_2 or moles -CN per liter of SOA and b) moles -ONO_2 or moles -CN per liter of SOA predicted using Kintecus®[137] for four organic nitrates (2EHN, HHN, HPN, and IBN) and two organic nitriles (NN and VN), for SOA formed from 250 ppb AP and 250 ppb O_3 in the presence of varying initial concentrations of each tracer and in the absence of an OH scavenger, at 31 minutes reaction time. Closed circles show the values quantified by ATR-FTIR, while the star for HPN indicated quantification by HR-ToF-AMS. Solid lines are best fits to guide the eye.

When the gas-phase tracer is present in the flow reactor in the absence of an OH scavenger, the tracers can react in the gas phase with the OH radical generated from the ozonolysis reaction. Figure 4.4b shows the moles $-ONO_2$ or -CN per L SOA for each experimental condition in Figure 4.4a predicted using a simple kinetic reaction scheme (Table 2.6). The model assumed that all of the reacted AP turns into a particle-phase species with a molecular weight of 200 g mol^{-1} and a density of 1.2 g cm^{-3},[138, 141-143] and that all of the tracer that reacts with OH partitions into the particle phase while maintaining the $-ONO_2$ or -CN functional groups.

The calculated OH rate constants for 2EHN and HHN are similar, and are a factor of approximately three larger than that for HPN or IBN (Table 2.6).[135] This is due to the long alkyl chains in 2EHN and HHN, which provide a number of potential sites for hydrogen abstraction by OH. Similarly, the OH rate constant for NN is approximately four times larger than that of VN. Many of the products formed from OH oxidation of these long alkyl chains are expected to be more functionalized and have lower volatility than the parent organic nitrate. Scheme 4.1 shows some of the likely routes for oxidation of 2EHN, HPN and HHN as an example. Thus, the combination of higher rate constants and lower volatility OH oxidation products for 2EHN and HHN are such that the products of OH oxidation can contribute significantly to the mass of the SOA in the absence of an OH scavenger.

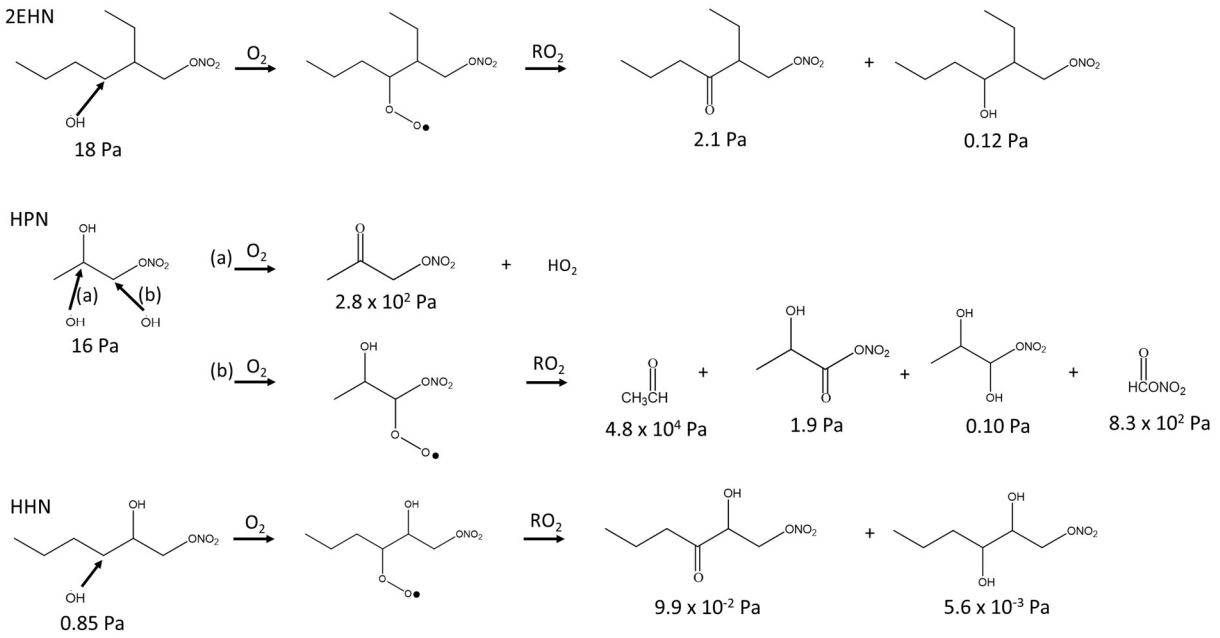

Scheme 4.1: Simplified reaction scheme showing some pathways for OH oxidation of 2EHN, HPN and HHN. The vapor pressures for each compound were estimated using SIMPOL.1.[126] Hydroxyl radical attack on a secondary carbon is shown for 2EHN and HHN due to the higher relative contribution of the sum of the secondary carbons to the total OH rate constant compared to that of the one tertiary carbon.

For the smaller species such as HPN, more of the reaction leads to higher volatility products that are not likely to contribute significantly to the SOA mass. Although the predominant pathway for OH reaction with 2EHN is through the secondary carbons due to their large number, 2EHN also has a tertiary carbon that can lead to fragmentation products. This may explain the model's overprediction for 2EHN (and also IBN). Additionally, as discussed in detail later, the particulate nitrate signal for the experiments with HPN was unaffected by the presence of an OH scavenger.

The trends seen in the organic nitrate signal measured by FTIR (Figure 4.1) in the presence or absence of the OH scavenger are also supported by the AMS data. Figure 4.5 shows the number of moles $RONO_2$ taken up per liter of SOA calculated from the AMS data at 31 min

reaction time (there was no statistical difference between 7 min and 31 min reaction time). Consistent with the FTIR data, the signal for 2EHN increases significantly (by a factor of ~14) when the SOA is formed in the absence of the OH scavenger. This factor is larger than that of Series A, indicating that it is the oxidation products of 2EHN that are incorporated into the SOA, and the difference is not simply due to a difference in the SOA bulk composition. A similar but smaller trend is seen for HHN (a factor of ~2.5), whereas the amount of HPN in the particles is unaffected by the presence of the OH scavenger. However, it should be noted that the detection methods used here (FTIR and AMS) focus on functional group analysis and are not direct measurements of the specific parent organic nitrate.

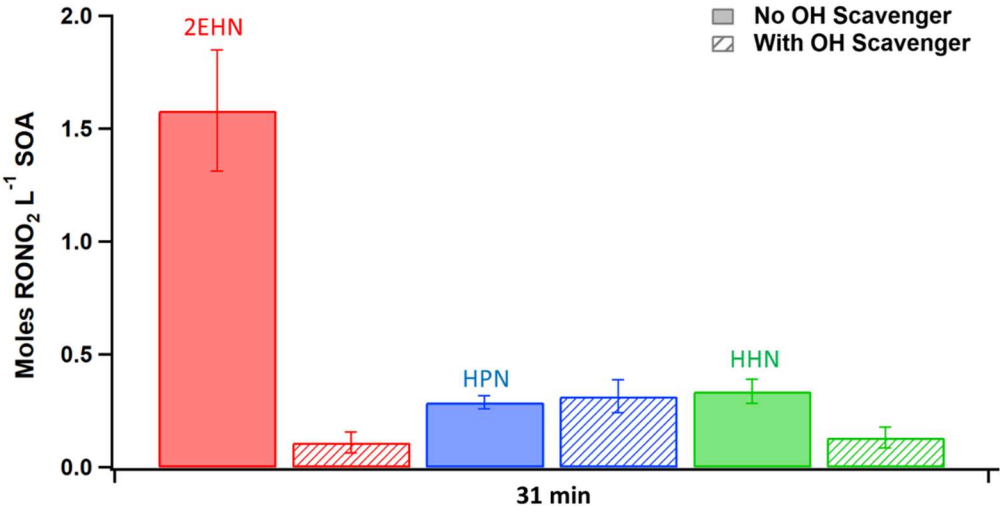

Figure 4.5: Quantification of moles of organic nitrate per liter of SOA (moles $RONO_2$ L^{-1} SOA) for SOA formed in the presence of 2EHN (5.6 ppm), HPN (4.7 ppm), or HHN (0.21 ppm), with or without OH scavenger at 31 minutes reaction time (Series C). Error bars are ± 2σ from the average of three experiments.

The much smaller effect seen for HHN is due to the smaller gas phase concentrations that were able to be added to the flow system, which results in HHN not competing very effectively

with the α-pinene for the OH radical generated in the ozonolysis. Thus, the initial first order rates of loss of OH, estimated using $k[X]_0$, where X = AP or $RONO_2$, are 3.3×10^2 s^{-1} for AP and 8.8×10^2 s^{-1} for 2EHN under the conditions shown in Figure 4.5 (the rate for AP decreases with time due to reaction with O_3). As a result, 2EHN competes with AP for OH, forming oxidized alkyl nitrate products that are incorporated into the SOA. On the other hand, $k[X]_0$ for HHN is only 27 s^{-1}, so relatively small amounts are oxidized by OH, whose removal is now mainly via reaction with AP, and incorporation of the unoxidized parent HHN contributes relatively more than its oxidation products to SOA growth. This is consistent with the magnitude of change in the incorporation of HHN into SOA formed with versus without CH, being similar for series A (uptake into preformed SOA) and series C/D (incorporation during SOA formation). While the first order loss rate for HPN by OH is 1.9×10^2 s^{-1}, many of the oxidation products are sufficiently small that they will not be efficiently incorporated into the SOA.

The contribution of OH radical chemistry is also manifested in the decrease in the particle number concentration in the presence of the OH scavenger, and in the presence of the organic nitrates which can also scavenge OH (Figure 4.6). Note that the total particle number concentration is smaller in the presence of CH (Figure 4.6a). This is consistent with previously reported work on the impact of the OH chemistry on SOA formation.[190-191] For example, Berndt *et al*.[192] showed that the OH radical plays an important role in the formation of highly-oxygenated organic molecules (HOMs), and thus scavenging the OH suppresses the formation of these HOMs, lowering SOA yields. Figure 4.6b, 4.6d, and 4.6f show the particle size distributions when organic nitrates are present during SOA formation without CH. A decrease in SOA is seen in the presence of 2EHN in a manner that is qualitatively similar to that due to

addition of CH alone (Figure 4.6a), while there is little impact for HPN and no impact at all for HHN. This is consistent with the relative rate constants for OH reaction with the organic nitrates versus CH (Table 2.6) and the initial concentrations of these compounds. As described above, 2EHN competes with AP for OH, but HHN does not. The rate of loss of OH by CH is 1.8×10^4 s^{-1}, which overwhelms the reaction of OH with AP or the organic nitrates. Based on kinetics modeling using Kintecus®[137] and a simplified reaction scheme (Table 2.6), less than 0.1% of the parent tracer reacts with OH after 31 min reaction time, indicating that 100 ppm CH is sufficient. Additional experiments were done for 2EHN using 500 ppm CH, and there was no statistical difference in the amount of 2EHN incorporated, supporting that 100 ppm CH is enough to adequately scavenge the OH. At 31 min reaction time without CH present, approximately 1.3% of the 2EHN has reacted with OH compared to ~0.8% of the HPN and ~4.3% of the HHN. This is consistent with the trend in the impacts on SOA, given the much lower initial gas phase concentration of HHN compared to the other organic nitrates.

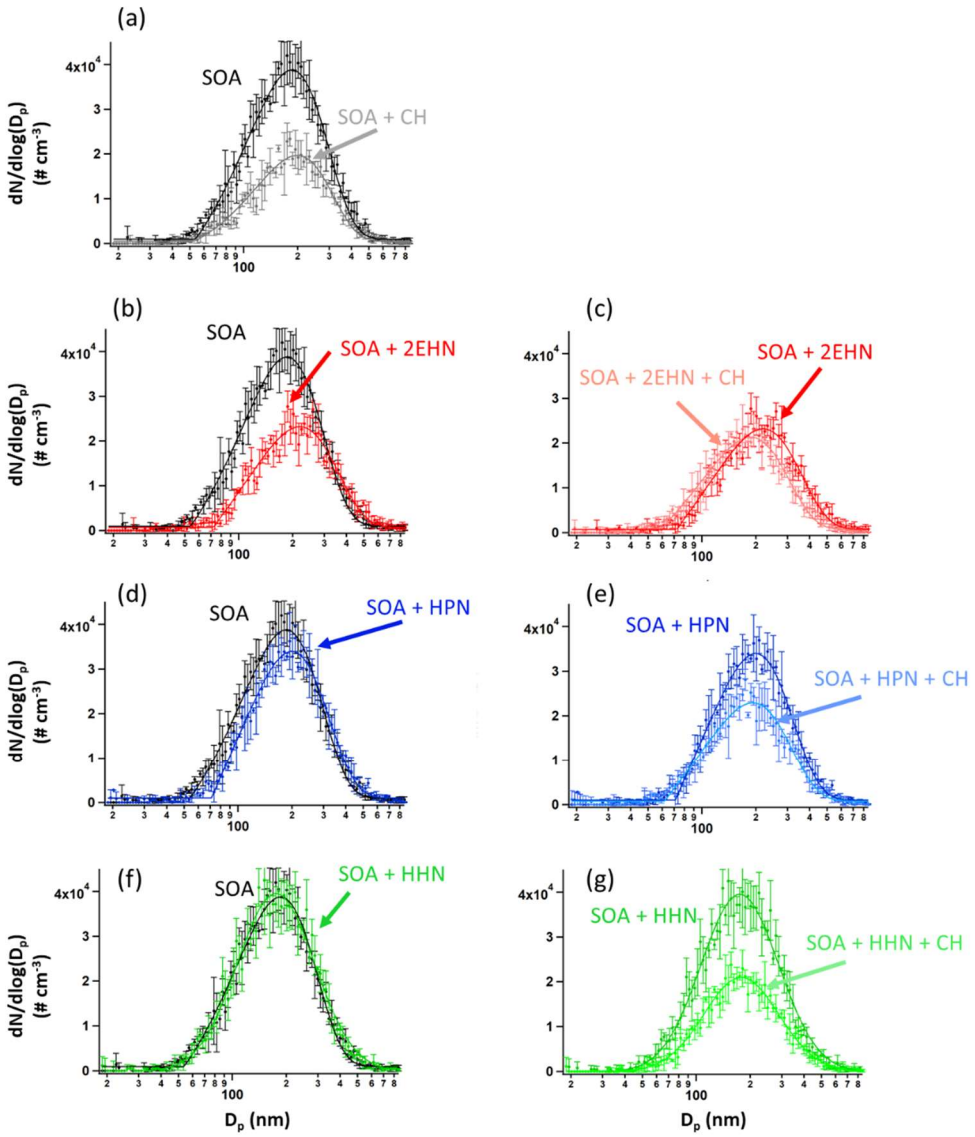

Figure 4.6: Particle number distributions (# cm^{-3}) at 31 minutes reaction time for a) SOA alone and formed in the presence of CH as an OH scavenger, b) SOA alone and formed in the presence of 2EHN (5.6 ppm), c) SOA formed in the presence of 2EHN either with or without CH, d) SOA alone and formed in the presence of HPN (4.7 ppm), e) SOA formed in the presence of HPN either with or without CH, f) SOA alone and formed in the presence of HHN (0.21 ppm), and g) SOA formed in the presence of HHN either with or without CH. Error bars are ±1σ from the average of three scans, and solid lines are best fit distributions to guide the eye.

In the absence of an OH scavenger, partition coefficients for 2EHN and HHN cannot be reliably quantified due to contributions from the $RONO_2$ + OH oxidation products whose identity and gas phase concentrations are not known. Instead, the concentrations of $RONO_2$ in

SOA (moles of $RONO_2$ per liter of SOA) were measured using both AMS (Figure 4.5) and FTIR as described in the experimental methods (Series C and D). The values for 2EHN and HHN are summarized in Table 4.1, showing the two methods are in relatively good agreement. Only the AMS value (Series C) is reported for HPN, as it was below the detection limit by FTIR.

Table 4.1: Organic nitrate content (moles L^{-1} SOA) for particles formed in the presence of 5.6 ppm 2EHN, 4.7 ppm HPN, or 0.21 ppm HHN in the absence of an OH scavenger (Series C and D, no CH).

	$RONO_2$ content (Moles L^{-1} SOA) [a] **Series C (AMS)**	**$RONO_2$ content (Moles L^{-1} SOA)** [a,b] **Series D (FTIR)**
2EHN	1.6 ± 0.3	1.6 ± 0.2
HPN	0.29 ± 0.03	n/a[c]
HHN	0.34 ± 0.05	0.50 ± 0.05

[a]Error bars are ± 2σ from the average of three experiments.
[b]FTIR quantification used the absorption cross section of the parent organic nitrate.[177]
[c]HPN was below the detection limit for FTIR.

4.3 Conclusions

The partitioning of various molecular probes into SOA particles in the absence of an OH scavenger was examined. The OH oxidation of these gas phase species leads to more oxidized lower volatility molecules which, in the case of those species with long hydrocarbon tails, partition into the particles to an even greater extent than the parent molecule. In the case of the smaller branched hydrocarbon chains, reaction with OH can lead to fragmentation, resulting in higher volatility products which will not be readily taken up into the particle phase. Although the OH rate constant for these species is smaller, reaction with OH remains a prevalent pathway and must be considered for these volatile organic molecules.

Chapter 5: Incorporation During Particle Growth in an Aerosol Flow Reactor in the Presence of an OH scavenger

5.1 Research Goals

The previous chapter established that when the molecular probes are present *during* particle formation and growth (series C and D) in a flow reactor in the absence of an OH scavenger, the reaction of OH with the molecular probes can enhance the amount incorporated by formation of more oxygenated, lower volatility products. This chapter focuses on the same system, but in the presence of an OH scavenger, which enables the quantification of partition coefficients for the molecular probes into the particles without complications from the OH oxidation.

5.2 Results and Discussion

When an OH scavenger is present, the main chemical pathway for reaction of the gas phase molecular probes (in this case, gas phase organic nitrates) is removed. Although Criegee intermediates may react with organic nitrates, this pathway is not likely to contribute significantly, as the major Criegee intermediate reactions are likely to be with carboxylic acids with a rate constant of $\sim 10^{-10}$ cm^3 $molecule^{-1}$ s^{-1}.[193] Additionally, the experiments discussed in Chapter 3 showed the incorporation of these species into particles after growth was reversible, indicating that particle-phase reactions of these tracers do not significantly occur on the timescales studied here. Thus, the measured signal for particulate-phase nitrate is attributed to the incorporation of the parent molecule, and partition coefficients can be calculated. Partition coefficients (K_C, defined as the ratio of $[\text{-ONO}_2]_{film}/[\text{-ONO}_2]_{gas}$ where $[\text{-ONO}_2]_{film}$ and $[\text{-ONO}_2]_{air}$ are the concentrations of organic nitrate in the film and in air, respectively) were calculated using

the AMS data for series C where the organic nitrates were present in the flow reactor while particles were forming and growing. Table 5.1 summarizes these partition coefficients at 31 min reaction time, which shows the same increasing trend from 2EHN to HPN to HHN seen for the incorporation after growth (Chapter 3).

Table 5.1: Comparison of partition coefficients into SOA formed in the presence of an OH scavenger when the organic nitrates are incorporated *after* growth (Series A, K_A, and Series B, K_B), or *during* growth (Series C, K_C).

Organic Nitrate	K_A (Series A)[a,b]	K_B (Series B)[c,d]	K_C (Series C)[b,c,e]	Ratio K_C/K_A
2EHN	$(3.2 \pm 1.5) \times 10^4$	$(2.9 \pm 0.7) \times 10^4$	$(4.7 \pm 1.0) \times 10^5$	15 ± 7.6
HPN	$(4.4 \pm 2.0) \times 10^5$	$(1.1 \pm 0.1) \times 10^5$	$(1.7 \pm 0.2) \times 10^6$	3.9 ± 1.8
HHN	$(4.9 \pm 0.8) \times 10^6$	n/a[f]	$(1.6 \pm 0.3) \times 10^7$	3.3 ± 0.81

[a]Using ATR-FTIR on impacted particles exposed to $RONO_2$.
[b]Error bars are $\pm 1\sigma$ from the average of three experiments.
[c]Using AMS on suspended particles exposed to $RONO_2$.
[d]Error bars are $\pm 1\sigma$ from the average of ~1-8 minutes exposure time
[e]Values are taken at 31 minutes reaction time in the stainless steel flow reactor
[f]Series B not done for HHN due to decomposition of the organic nitrate.

To establish that the uptake into impacted particles is similar to particles suspended in air, experiments were carried out in which the SOA particles were denuded (to reduce the amount of α-pinene gas phase oxidation products), diverted to a mini glass flow tube, and subsequently exposed to gas phase 2EHN or HPN (series B). In the case of 2EHN, the measured 2EHN concentration (~120 ppm) was similar in magnitude to that used for the impacted particles in series A. The gas phase concentration of HPN in this series could not be accurately measured from the glass flow tube due to losses on the walls and sampling line. However, the measured concentration of 2EHN in series B showed ~40% loss to the glass walls of the flow tube when

compared to the gas phase concentration directly out of the trap. Assuming a slightly higher percent loss of 50% of the more oxygenated HPN to the walls of the glass flow tube, the resulting gas phase concentration is ~80 ppm. The partition coefficient for series B was determined using AMS for times of exposure to the gas phase $RONO_2$ of approximately one to eight minutes. These exposure times encompass the timeframe for the organic nitrate to reach equilibrium in experiments on impacted particles, which was approximately 2-3 min (Figure 3.2). The average partition coefficient (K_B) for 2EHN is in reasonable agreement with that for series A (Table 5.1). The agreement is not as good for HPN, which may be due to uncertainties in the gas phase concentration due to wall losses. These experiments confirm that suspended particles come to the same equilibrium as the thin film of impacted particles upon exposure to high concentrations of organic nitrates. It also demonstrates that both the AMS and the FTIR measurements are in excellent agreement with each other.

The concentration of the organic nitrate in series B was then reduced by removing the reservoir inside the glass flow tube and instead introducing the organic nitrate into the system using a trap and flowing clean air over the pure liquid. This diluted the organic nitrate, resulting in gas phase concentrations of ~12 ppm for 2EHN and ~6.6 ppm for HPN. Under these conditions, the organic nitrate signal in the particles is expected to approach the limit of detection, and in fact it was undetected. This smaller gas phase organic nitrate concentration is comparable to the concentration used in series C/D (incorporation *during* growth, discussed in Chapter 4 and below) where a plasticizing effect was not observed. The lack of detection of the organic nitrate is thus consistent with earlier experiments that have shown that SOA from the ozonolysis of AP under dry conditions is a high viscosity semi-solid.[48, 55, 63-67, 70] Diffusion

coefficients for particles from AP ozonolysis formed under dry conditions range from 10^{-14}-10^{-17} cm^2 s^{-1}.[52, 62-63, 194] Using the Stokes-Einstein relation and assuming a molecular radius of 1 nm,[26, 37] this results in viscosities ranging from 10^5-10^8 Pa s, consistent with measured viscosities for SOA from AP ozonolysis.[50, 55, 68, 195-197] The resulting characteristic timescale for diffusion[60] through a semi-solid 200 nm particle is at least half an hour, much longer than the maximum residence time for series B of ~8 minutes. Thus, net uptake of the organic nitrate into high viscosity SOA on the time scale of these experiments is smaller than at equilibrium due to slow diffusion through the particles.

The incorporation of the organic nitrates *during* growth (series C) was then examined as described in Chapter 2 (section 2.6) in the presence of 100 ppm CH as an OH scavenger for comparison. The results show that the partition coefficients (K_C) in these experiments are much larger than those for series A (Table 5.1), which might seem surprising since they imply a larger than equilibrium concentration in the particles. As described above, the difference observed is not associated with bias in the two analytical techniques (AMS and ATR-FTIR) that were used. Additionally, series C used much lower gas phase concentrations than for series A, so the explanation cannot be a significant plasticizing effect that lowers the viscosity and results in faster uptake. In support of this, Figure 5.1 shows typical impaction patterns for SOA formed either with or without an organic nitrate or OH scavenger present. Also shown in Figure 5.1 for comparison are the impaction patterns for deliquesced Na_2SO_4 particles, dry carboxylate-modified latex particles, and SOA particles formed at 87% relative humidity which is known to decrease their viscosity.[196-198] Upon impaction, particles hit and may stick to the substrate directly below the orifice plate to form spots, or they may bounce and either be re-entrained into

the gas stream, be subsequently re-captured on the substrate to form a cloud or halo, or form midlines due to multi-orifice interactions.[199] The impaction patterns in Figure 5.1 are distinctly different from both the deliquesced $NaSO_4$ and the SOA formed at high relative humidity, indicating the particles in the current study are highly viscous. The patterns do not change across the experimental conditions, suggesting there was no significant change in the viscosity upon addition of the organic nitrates or cyclohexane. One might therefore expect that the uptake into semi-solid particles would be hindered. However, our results (series C) show the opposite, which highlights that the incorporation of organic nitrates is driven by a different phenomenon than diffusion.

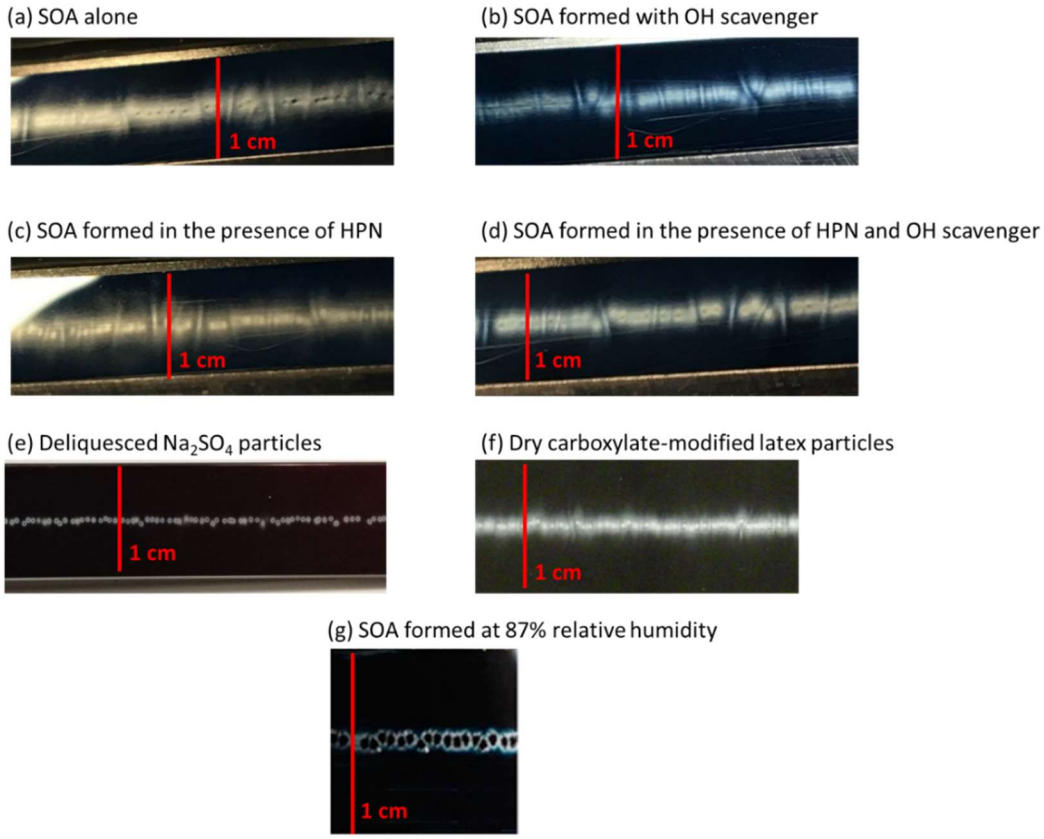

Figure 5.1: Typical impaction patterns for a) SOA alone for Series A without organic nitrate or CH, b) SOA formed in Series A in the presence of CH, c) SOA formed in the presence of 4.7 ppm HPN in the flow reactor (Series C/D), d) SOA formed in the presence of both HPN and CH (Series C/D), e) deliquesced Na_2SO_4 particles, f) dry 270 nm carboxylate-modified latex particles, and g) SOA particles formed at 87% relative humidity (parts e-g adapted from Kidd *et al*).[70]

When the gas phase $RONO_2$ concentration used in series B for incorporation after growth was lowered to approximately that used in series C, the organic nitrate signal became undetectable, consistent with a higher viscosity limiting uptake into and diffusion through the pre-formed and denuded particles.[54] K_C values from series C taken at 7 min and 31 min are not significantly different, and thus the higher partition coefficients in series C are not resulting from the longer time spent in the flow reactor. The presence of the gas-phase ozonolysis products in the large flow reactor in series C must therefore play a central role in the incorporation of the

organic nitrates *during* particle formation and growth that enhances organic nitrate uptake beyond the expected equilibrium established in series A/B.

Physical Mechanism for Particle Growth

As described previously, the growth of the SOA particles by ozonolysis products and the incorporation of the organic nitrates into the particles in the stainless steel flow reactor may be best described by a kinetically limited "burying" mechanism. Figure 5.2 shows a simplified schematic that describes this mechanism, where $RONO_2$ represents the organic nitrate, and P1 is a proxy low volatility organic from the ozonolysis of α-pinene. When the organic nitrate is present *during* particle growth in the flow reactor (series C/D), condensing P1 molecules can bury the organic nitrate and hinder re-evaporation into the gas phase, resulting in larger partition coefficients than those measured after particle growth at equilibrium (series A/B).

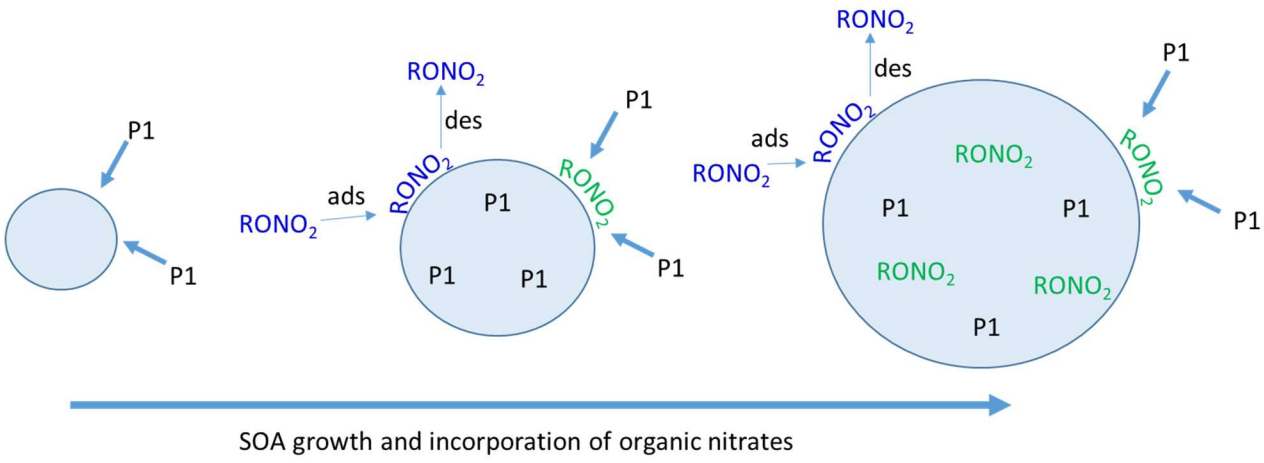

Figure 5.2: Schematic of "burying" mechanism for incorporation of organic nitrate tracers as SOA particles are forming. $RONO_2$ represents the organic nitrate, and P1 is a proxy for low volatility organics from the ozonolysis of α-pinene. When the organic nitrate is present during

particle growth, the P1 can bury the organic nitrate and hinder its re-evaporation into the gas phase.

Figure 5.3 shows the HR-PToF data for both the total organic and the ratio of (NO^+ + NO_2^+) to total organics as a function of particle size for SOA formed in the presence of 2EHN at 7 min reaction time, either with or without CH. The ratio (NO^+ + NO_2^+)/HROrg is a measure of the relative concentrations of organic nitrate in the SOA. This ratio is approximately constant across the range of particle sizes, confirming that relative rates of incorporation of the organic nitrates and the organics that grow the particles do not vary significantly as the particles grow across this diameter range. The corresponding data for SOA formed in the presence of HPN and HHN are also shown in Figure 5.3 and show similar results. For comparison, Figure 5.4 shows HR-PToF analysis for two major fragments, $C_2H_3O^+$ (a marker for carbonyl groups) and CO_2^+ (a marker for carboxylic acid groups),[200-201] and the ratio of these two fragments. In contrast to the uniform organic nitrate composition over all particle diameters, this ratio is smaller for smaller diameter particles, indicating more acid groups on average than in the larger particles.

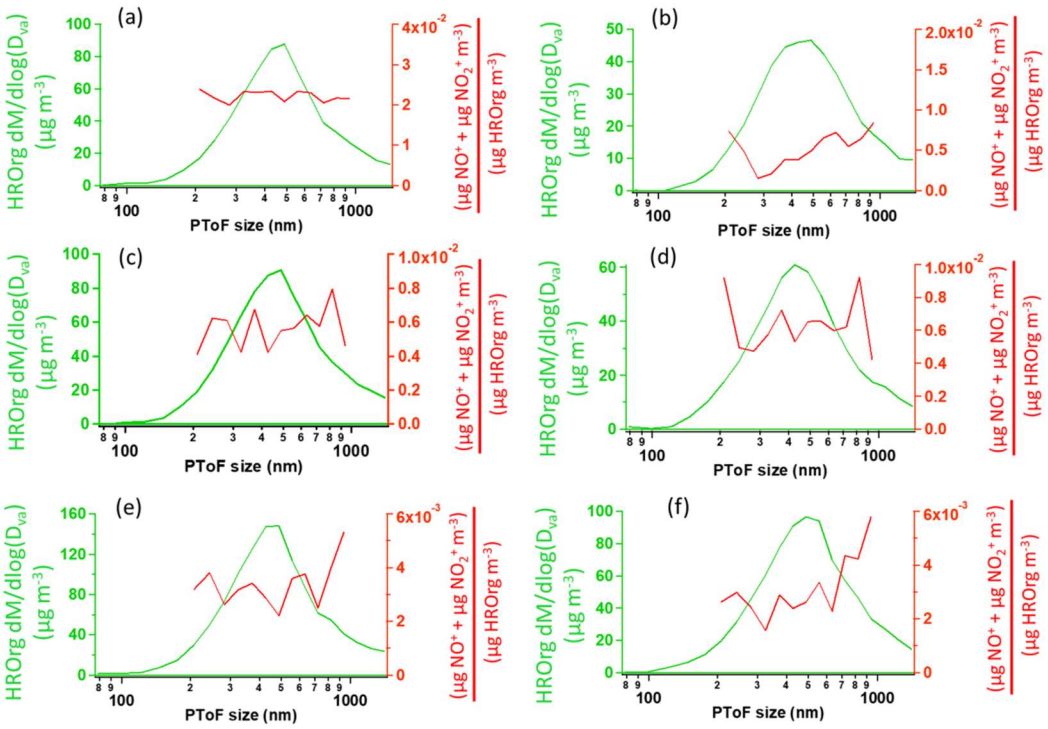

Figure 5.3: The HR-PToF mass distribution of total HROrg (green) and the HR-PToF mass ratio of (NO^+ + NO_2^+) to HROrg (red) for a) SOA formed in the presence of 2EHN (1.4×10^{14} molecules cm^{-3}), b) SOA formed in the presence of 2EHN and CH (2.5×10^{15} molecules cm^{-3}), c) SOA formed in the presence of HPN (1.2×10^{14} molecules cm^{-3}), d) SOA formed in the presence of HPN and CH (2.5×10^{15} molecules cm^{-3}), e) SOA formed in the presence of HHN (5.0×10^{12} molecules cm^{-3}), and f) SOA formed in the presence of HHN and CH (2.5×10^{15} molecules cm^{-3}) at 7 min reaction time. Note the NO^+ and NO_2^+ signals in the presence of CH have high uncertainty due to weak signal.

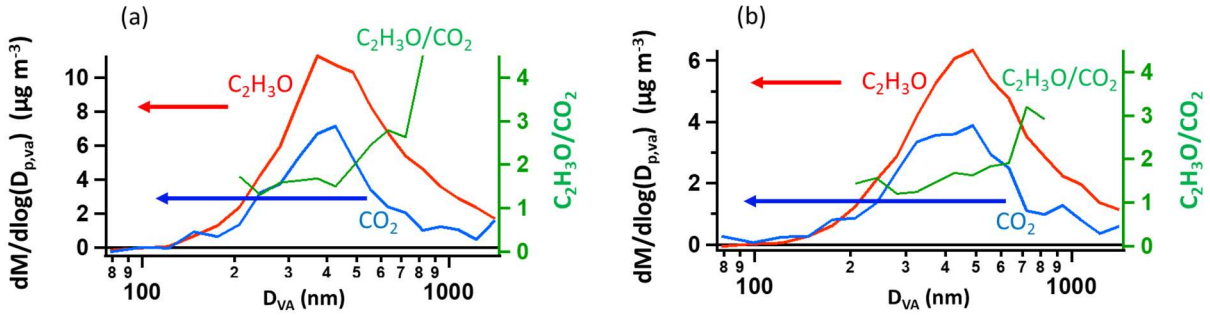

Figure 5.4: The HR-PToF mass distribution $C_2H_3O^+$ (red), CO_2^+ (blue), and the ratio of $C_2H_3O^+/CO_2^+$ (green) for a) SOA alone at 7 minutes reaction time, and b) SOA formed in the presence of CH (2.5×10^{15} molecules cm^{-3}) at 7 minutes reaction time.

5.3 Conclusions

Uptake of organic nitrate tracers into highly viscous, semi-solid SOA particles during their formation in the ozonolysis of AP offers new insights into the molecular interactions between gases and particles that ultimately lead to particle growth. The role of the OH radical resulting from the ozonolysis reaction is important not only for the bulk composition of the particles and overall SOA number concentration, but also for the role it plays in the gas-phase chemistry of the organic nitrates. In the case of the smallest organic nitrate, HPN, the partitioning was unaffected both by the reaction of HPN with OH and by any changes in the particle composition by scavenging OH. However, the two long-chain organic nitrates were affected by both factors.

The amount of organic nitrate taken up into growing particles relative to the gas phase concentration was found to be larger than expected based on the equilibrium partition coefficients into pre-existing impacted particles. This may be attributed to the evolution of particles during growth, such that continued uptake of organics leads to 'burying' of the organic nitrate, hindering re-evaporation into the gas phase. This is consistent with the HR-PToF analysis which shows that the organic nitrate was evenly distributed across all particle diameters. Such a mechanism results in a larger amount of organic nitrate in the particles than expected based on the equilibrium achieved when the nitrate is incorporated after growth into impacted particles. This could play a role in cases where mechanisms in addition to thermodynamic partitioning have been implicated.[73, 81, 103, 202] The results highlight the importance of a molecular level understanding of the interactions of gases with particle surfaces and their bulk as the foundation for accurately predicting their impacts on air quality and climate.

Chapter 6: Incorporation During Growth at Variable Mass Loadings

6.1 Research Goals

This research examines the changes in particle mass loading and composition and how they affect the incorporation of gas phase species. The preceding chapters show indication of a burying mechanism that can facilitate the incorporation of gases into the particles at amounts larger than expected based on equilibrium partitioning. Previous studies have shown that changing the concentration of the SOA precursors or varying the particle mass loading can change the composition and viscosity of the particles, including changing the distribution of oligomer products.[195, 203-208] This chapter expands on series C and D (incorporation *during* growth) and examines how changes in the gas phase product distribution as well as changes in the particle composition affect the incorporation of the molecular probes.

6.2 Results and Discussion

Particle size distributions

Figure 6.1 shows typical values for (a) the total number concentration, (b) number-weighted geometric mean diameter, (c) total surface area, and (d) total mass concentration for particles formed from AP and O_3 either with or without OH scavenger at 7 min and 31 min reaction time. The corresponding particle number distributions are shown in Figure 6.2. In all cases, there is little evolution of the size distributions between 7 min and 31 min reaction time, indicating that most of the particle formation and growth is completed by 7 min.

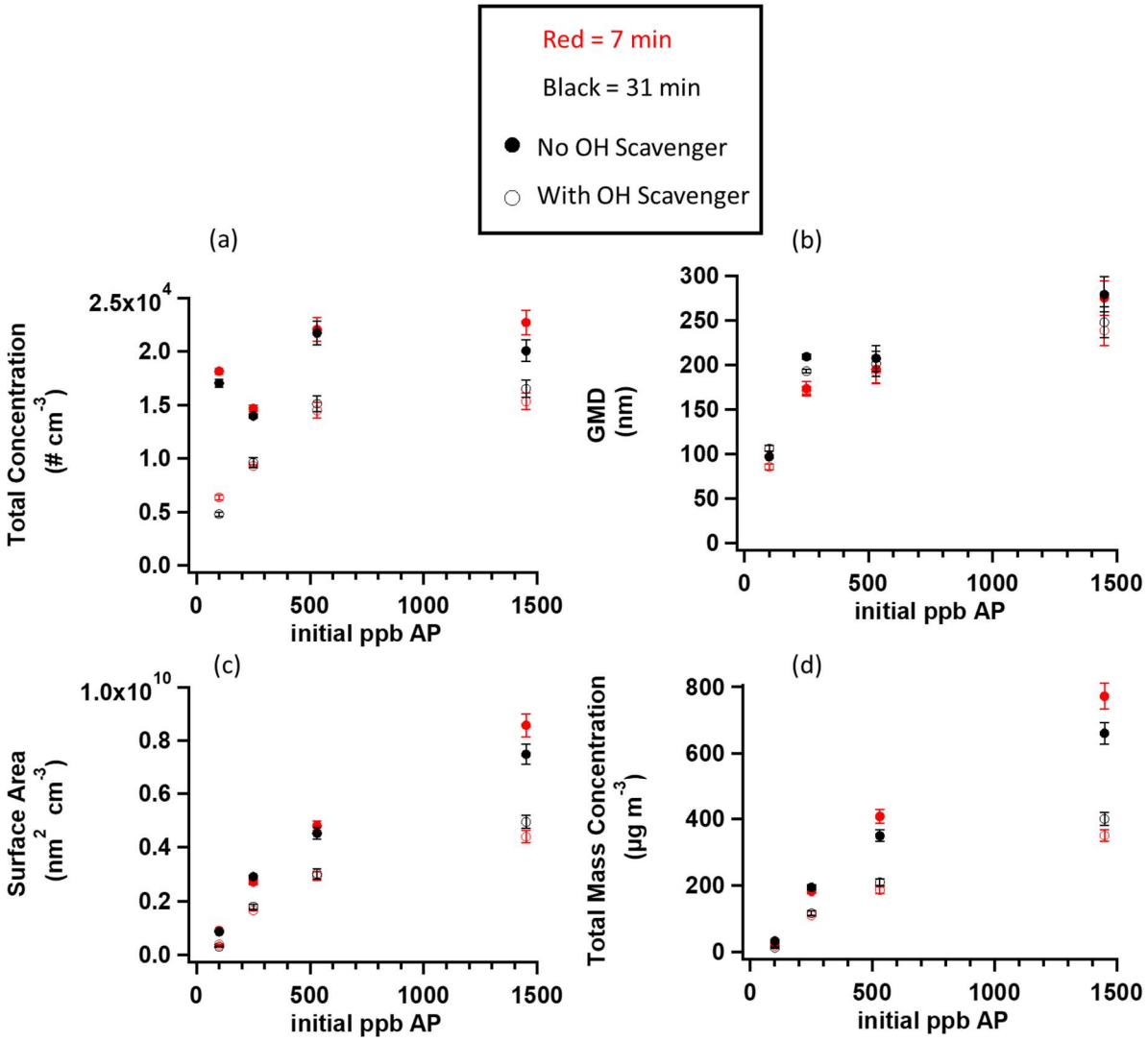

Figure 6.1: Typical a) total particle concentrations (# cm^{-3}), b) number-weighted geometric mean diameter (GMD, nm), c) surface area concentration (nm^2 cm^{-3}), and d) total mass concentration (µg m^{-3}) for particles formed either without OH scavenger (closed circles) or with OH scavenger (open circles), at 7 min (red) and 31 min (black) reaction time, formed without organic nitrate present. Error bars are ± 1σ from the average of 3 consecutive scans for the 100 and 250 ppb AP conditions, and ± 5% applied to the Weibull fit for the higher concentrations.

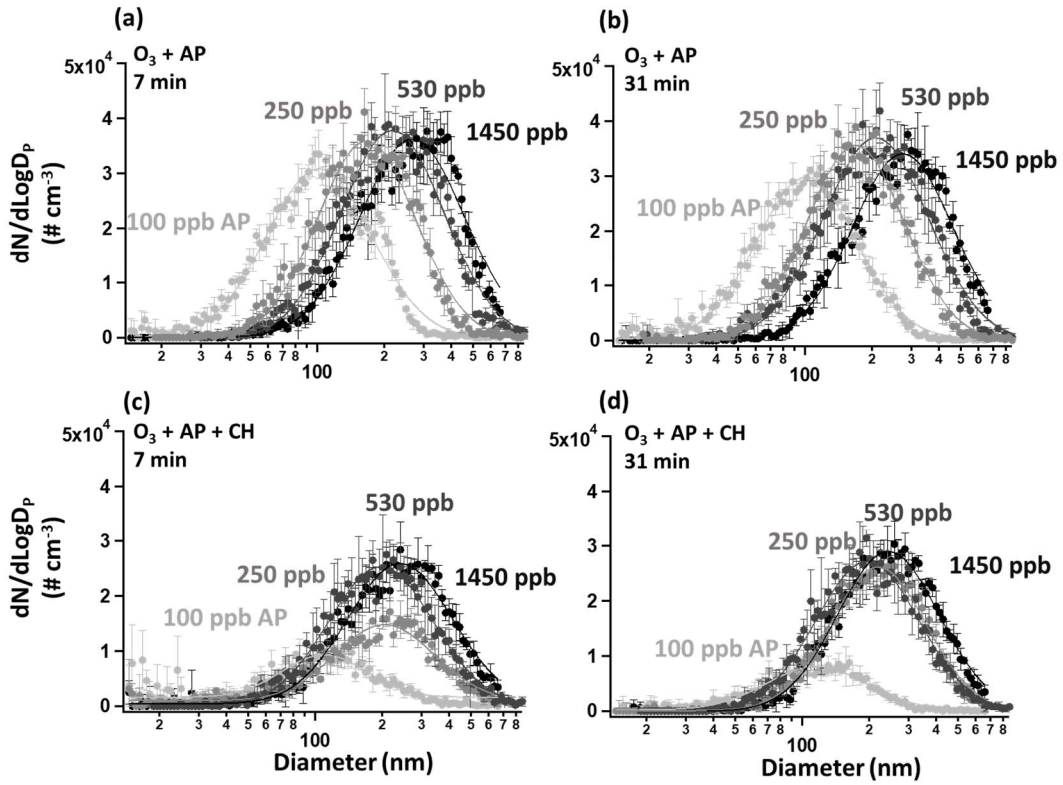

Figure 6.2: Particle size distributions for SOA formed *without* OH scavenger in the absence of organic nitrate at a) 7 min and b) 31 min reaction time, and the particle size distributions for particles formed *with* OH scavenger in the absence of organic nitrate at c) 7 min and d) 31 min reaction time. Error bars are ± 1σ from the average of 3 scans.

When particles are formed in the presence of 100 ppm CH as an OH scavenger, the total particle number concentration drops for all concentrations of AP (along with the corresponding mass and surface area concentrations), but the particle diameter does not significantly change compared to without OH scavenger. This is consistent with previous studies that showed OH scavengers can reduce the total number of particles formed.[190, 192]

Two cases are evident as initial AP concentration increases. First, while for experiments performed in the absence of OH scavenger the total number concentration remains relatively similar across the conditions, the particles are growing as indicated by the increase in GMD

(~100 nm at 100 ppb AP versus ~250 nm at 1450 ppb AP), leading to an increase in total mass and surface area. Thus, as the concentration of AP increases, the concentrations of its oxidation products that are responsible for particle growth also increase. Second, in the presence of CH, total number and GMD (and thus surface area and mass) increase, indicating that both new particle formation and growth are occurring.

Similar trends are seen for SOA formed in the presence of each organic nitrate. Figure 6.3 shows the particle size distributions for SOA alone, upon addition of each organic nitrate, and after OH scavenger is added. The organic nitrates themselves can act as OH scavengers, and in the case of 2EHN and HHN their rate constants with OH are comparable to that of CH with OH (Table 2.6). Of the three organic nitrates, 2EHN has the fastest OH rate constant and the largest gas phase concentration. These two factors result in the most prominent change in the particle size distribution upon addition of 2EHN to the system. Second, HHN has a similar OH rate constant to 2EHN, but has a much smaller gas phase concentration, so there was no evident change in the size distribution upon addition of HHN. Lastly, HPN has a similar gas phase concentration to 2EHN but a lower OH rate constant, and so the change in the particle size distribution upon addition of HPN was less drastic than for 2EHN. The size distributions show that the impacts of adding an organic nitrate are, in some cases, similar to those of adding an OH scavenger, which has implications for the organic nitrate content in the particles as discussed later.

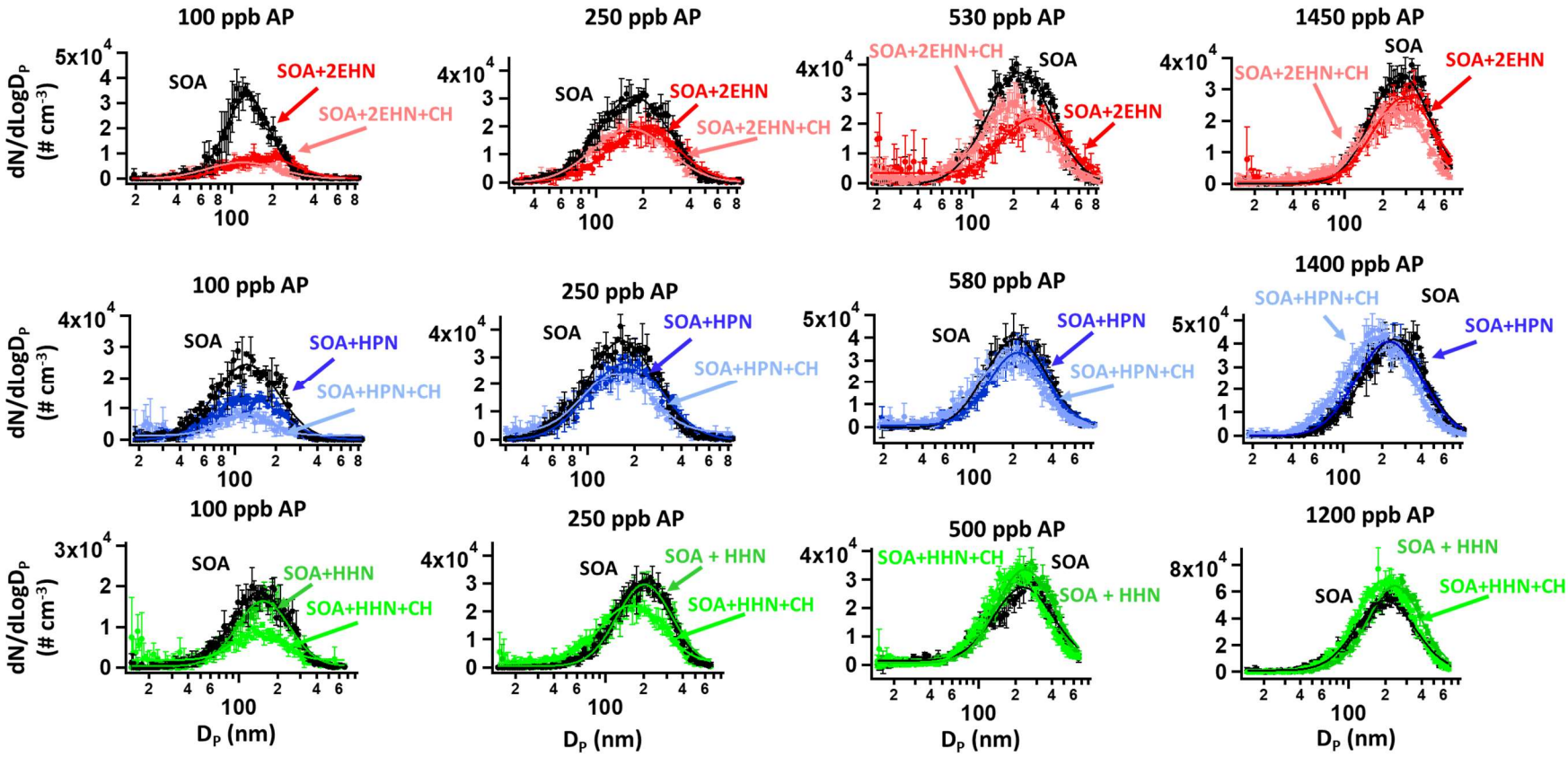

Figure 6.3: Particle size distributions for SOA alone, upon addition of each organic nitrate, and after addition of CH as an OH scavenger, at 7 min reaction time. Error bars are ± 1σ from the average of 2-3 scans.

Figure 6.4 shows the SOA yields (defined as the amount of SOA formed (μg m^{-3}) divided by the amount of AP reacted (μg m^{-3}) as a function of SOA mass loading for all experiments either with OH scavenger or without OH scavenger, and either with or without the organic nitrate present. The presence of the OH scavenger or the organic nitrates (which can also act as OH scavengers themselves) did not have a significant impact on the yield. The range of values for SOA yield here are in good agreement with previously reported yields from AP ozonolysis.[209-217] Previous studies have shown that the addition of OH scavengers changes the ratio of HO_2 to RO_2 in the system relative to that of no OH scavenger, which resulted in lower SOA yields when the OH scavenger was present.[191, 218-219] Although the total particle number and SOA mass decreased when CH was present in these experiments (Figure 6.2 and Figure 6.3), there was no observed decrease in the SOA yield, although variability in the measured SOA yield is large. As mentioned in Chapter 2, there is some uncertainty in the initial concentration of AP at the higher AP/mass loading conditions. This uncertainty and the large scatter in the measured SOA yields result in no statistical difference in the yields measured here across all reaction conditions.

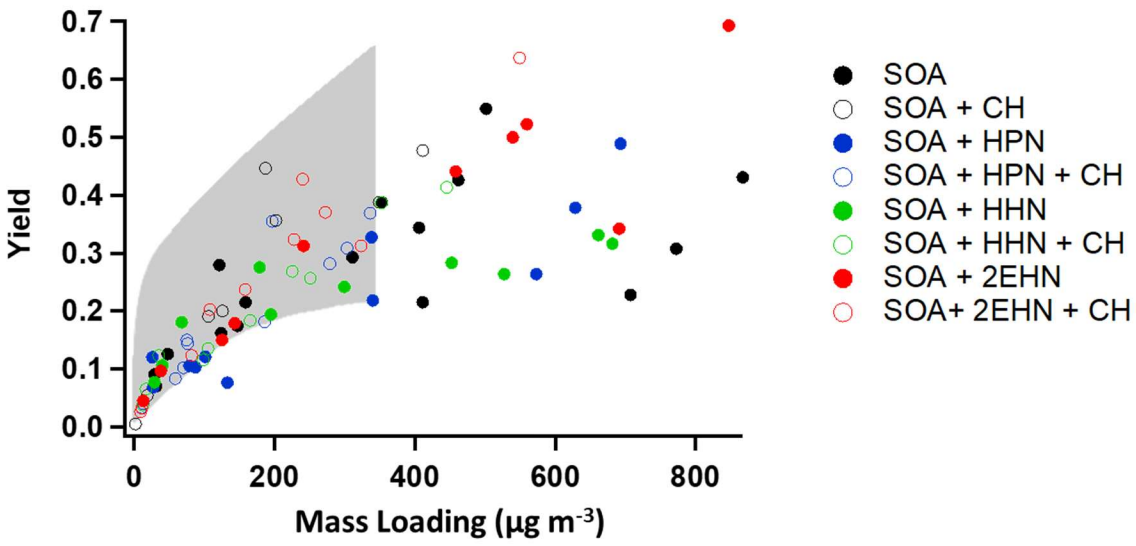

Figure 6.4: SOA yields as a function of the SOA mass loading, for SOA formed either with 100 ppm CH as an OH scavenger (open circles) or without OH scavenger (closed circles), alone (black) or in the presence of 5.6 ppm 2EHN (red), 4.7 ppm HPN (blue), or 0.21 ppm HHN (green). The grey shaded region shows the range of yields reported in the literature for particles formed either with or without OH scavenger.[209-217]

Indications of Particle Phase

SOA particles from the ozonolysis of AP under dry conditions have previously been shown to be highly viscous or semi-solid in phase.[48, 55, 63-67, 70] Figure 6.5 shows photographs of the impaction pattern for the particles formed either with or without OH scavenger without organic nitrate present for all AP concentrations. High viscosity semi-solid or solid particles can bounce and be re-entrapped, resulting in a cloud or halo around the midline.[70, 199] For the impacted particles formed at AP concentrations above 500 ppb, the cloud was evident both without the OH scavenger and when the OH scavenger was present. This indicates that scavenging the OH chemistry did not change the bouncing properties of the particles.

Some changes in the size of cloud were seen from the variation in total impacted mass due to lower particle concentrations when OH was scavenged. Although a small cloud was visible for the 250 ppb initial AP condition without OH scavenger, when OH scavenger was present it was only evident at the mid-lines of the orifice plate holes but was still different from a mirror image of the holes of the orifice plate that is expected for liquid particles. The impacted particle pattern for 250 ppb AP with OH scavenger condition appeared similar to dry carboxylate-modified latex particles of a similar diameter, further indicating that these particles are not liquid.[70, 220] At 100 ppb AP, the cloud was further reduced either with or without OH scavenger regardless of amount impacted due to the smaller size of the particles. This is expected, as smaller particles are known to affect the probability of bounce and recapture and due to the majority of the particles being smaller than the 50% cutoff of 240 nm for the impactor (thus resulting in a smaller total impacted mass).[70, 221] Jain *et al*.[207] showed that the bounce factor of particles from AP ozonolysis in the absence of an OH scavenger decreased as the mass loading increased. Additionally, Grayson *et al*.[195] found that under dry conditions, the experimental flow time (an indicator of viscosity) for particles from AP ozonolysis using 2-butanol as an OH scavenger decreased by a factor of 45 as the mass loading increased from 121 μg m^{-3} to 14000 μg m^{-3}. The mass loadings studied here cover a much smaller range, from ~10-900 μg m^{-3}, and therefore the change in viscosity over this range is expected to be negligible. Thus, the particles at the smaller mass loading conditions in Figure 6.5 are likely highly viscous despite the reduced evidence of particle bounce.

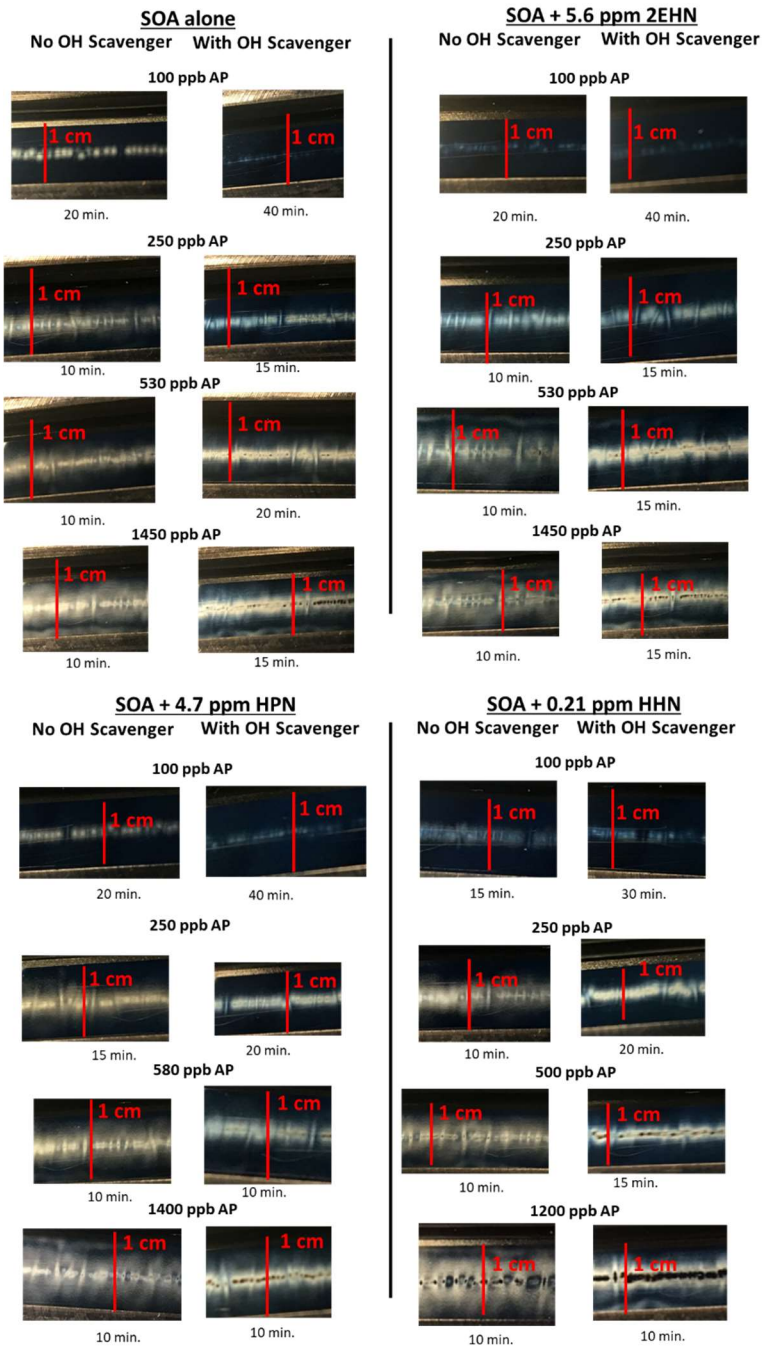

Figure 6.5: Typical impaction patterns for particles formed from 250 ppb O_3 at various AP concentrations, in the presence or absence of each organic nitrate, either with or without 100 ppm CH OH scavenger. The white shows the impacted particles reflecting overhead fluorescent lights. Impactions are taken at the end of the flow reactor, corresponding to 31 min reaction time. The time below each photo shows the amount of time for which the particles were collected.

High concentrations of these $RONO_2$ have been shown to have a plasticizing effect on the SOA (Chapter 3). Equilibrium with the gas phase was achieved upon introduction of high concentrations (approaching saturation vapor pressures) of the three organic nitrates on the timescale of ~4 to 20 min.[177] However, the concentrations used in the flow reactor are over 30 times smaller, and did not induce a significant plasticizing effect in our previous study using initial conditions of 250 ppb of both AP and O_3.[220] Figure 6.5 also shows typical patterns for impaction of the particles formed in the presence of ppb to low ppm concentrations of gas phase organic nitrate, either with or without OH scavenger. The particles formed in the presence of the organic nitrate showed similar trends to those discussed above for the 'SOA alone' conditions, which indicates that the gas phase organic nitrate concentrations were not high enough to induce a significant plasticizing effect, and the particles remained highly viscous.

Particulate organic nitrate concentrations in the absence of an OH scavenger

Figure 6.6a shows the HR-ToF-AMS measured concentration of condensed phase organic nitrate (in moles $RONO_2$ per L of SOA) for all concentrations of AP in the absence of an OH scavenger at 7 minutes reaction time, calculated using Equation 2.9. Similar values were obtained for particles measured at 31 min. For 2EHN, the amount of organic nitrate that is observed in the particles decreases as the initial concentration of AP increases. The OH rate constant for 2EHN (Table 2.6) is such that it can react to form lower volatility oxidation products retaining the $-ONO_2$ moiety[220] that can partition into the SOA. The initial first order rates of loss due to reaction with OH, estimated as $k[X]_0$ where X is AP or 2EHN, reveal the likelihood of 2EHN acting as an OH scavenger at each condition. For the lowest initial concentration of AP ($[AP]_0$ = 100 ppb), 2EHN acts as an efficient OH scavenger itself as its initial loss rate

($k[2EHN]_0 = 8.8 \times 10^2\ s^{-1}$) is almost seven times higher than that of AP ($k[AP]_0 = 1.3 \times 10^2\ s^{-1}$), consistent with the change in the particle size distribution seen in Figure 6.3. Alternately, for the higher concentrations of AP ($[AP]_0 = 1450$ ppb), the initial rate of AP loss ($k[AP]_0 = 1.9 \times 10^3\ s^{-1}$) is ~2.2 times higher than that of 2EHN. Thus, as the initial concentration of AP increases, OH preferentially reacts with AP instead of 2EHN, and as a result, less multifunctional lower volatility oxidation product derived from the parent nitrate is taken up into the particles, consistent with the trends in Figure 6.3 and Figure 6.6a.

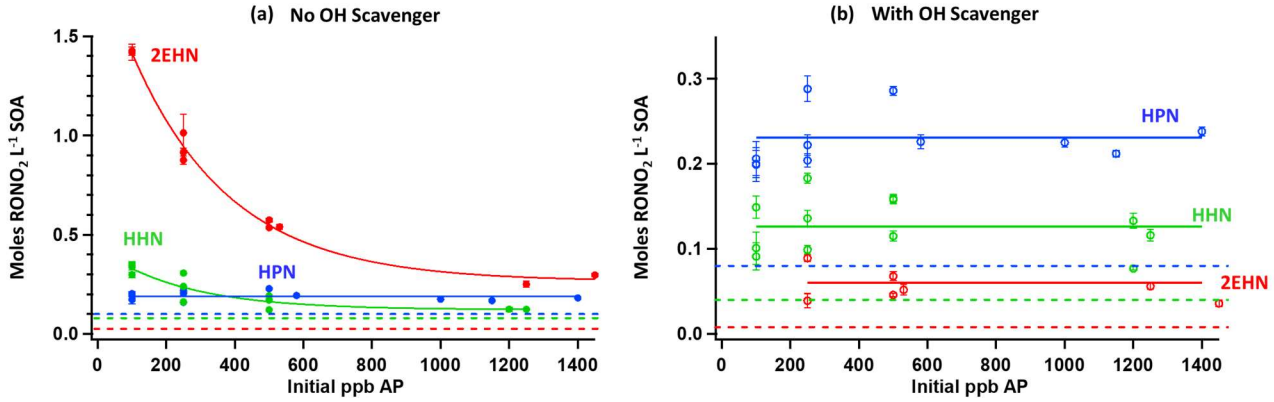

Figure 6.6: Moles organic nitrate per liter of SOA (determined from the AMS) for particles formed in the presence of 5.7 ppm 2EHN, 4.6 ppm HPN, or 0.21 ppm HHN, a) in the absence of 100 ppm CH as an OH scavenger and b) in the presence of 100 ppm CH, each at 7 minutes reaction time. Error bars are ± 2σ from the absolute uncertainty in the AMS. Solid lines are best fits to the data points to guide the eye in (a), and in (b) they are the average moles organic nitrate per liter SOA across the reaction conditions. Dashed lines are the expected values if equilibrium partitioning from uptake into thin films of impacted particles held.[177, 220] The 2EHN signal in the particles in (b) was not detectable at 100 ppb initial AP.

A similar trend is seen in Figure 6.6a for HHN, but to a much lesser extent. The initial first order rate of loss due to reaction with OH is 27 s^{-1} for HHN and is less than that of AP across all the conditions in the figure. For 100 ppb AP the initial rate of AP loss due to OH reaction is ~5 times higher, whereas it is ~80 times higher for ~1.5 ppm AP relative to HHN loss.

For the lowest concentration of AP, some of the OH is still able to react with HHN to form lower volatility oxidation products (with a retained -ONO_2 functional group)[220] that are incorporated into the particles. Therefore, there is slightly more organic nitrate taken up in this condition when compared to the higher concentrations of AP in the presence of HHN.

For HPN, the amount of organic nitrate taken up into the particles is unaffected by the concentration of AP (Figure 6.6). The initial rate of loss to reaction with OH is 1.9×10^2 s^{-1} for HPN (compared to 8.8×10^2 s^{-1} for 100 ppb AP). However, as discussed previously by Vander Wall *et al*,[220] the products of the HPN reaction with OH are likely to be small and more volatile and thus are not expected to be incorporated into the SOA. However, there is a change in the particle size distributions in the presence of HPN at the smallest AP concentration (Figure 6.3), reflecting a smaller contribution of OH + AP chemistry to particle nucleation/growth.

In summary, the measurements of condensed phase organic nitrate in the absence of an OH scavenger indicate that under each initial AP condition, a different amount of (unidentified) oxidation products is taken up into the particles. However, in the presence of an OH scavenger, only the parent organic nitrate is taken up, and thus these scavenger experiments can be used to determine partition coefficients for the three parent organic nitrates.

Partition coefficients and particle composition in the presence of an OH scavenger

When an OH scavenger is present, the contribution of the $RONO_2$ + OH reaction products to the particulate organic nitrate signal is small. From kinetics modeling[137, 220] at 7 min reaction time, less than 0.03% of HPN, 0.10% of HHN, and 0.11% of 2EHN reacts with OH

when 100 ppm CH is present at all AP concentrations (compared to 0.3% of HPN, 1.5% of HHN, and 0.83% of 2EHN when no OH scavenger is present), and thus the organic nitrate in the particles is attributed to the parent organic nitrate. Figure 6.6b shows the measured concentrations of the organic nitrate in SOA in the presence of CH. Under those conditions, no trends are apparent across the range of AP concentrations, with the exception of 2EHN which is not detected at the lowest AP concentration (100 ppb). With that exception, it is important to note that for all three nitrates, the concentration of the nitrate taken up by the particles is higher than that estimated from equilibrium partitioning into thin films of impacted particles (dashed lines in Figure 6.6, determined after accounting for the difference in gas phase $RONO_2$ concentration between the flow reactor and thin film experiments).[220]

Partition coefficients, $K_{C,}$ were calculated using Equation 2.9 and are shown in Figure 6.7 for all three organic nitrates across all initial concentrations of AP. Also shown in Figure 6.7 are the partition coefficients determined for equilibrium partitioning into thin films of impacted particles formed from 250 ppb AP and 100 ppm CH.[220] For all $RONO_2$ there was no distinct trend in the partition coefficient across all AP concentrations, apart from the partitioning of 2EHN into SOA formed from 100 ppb AP, which was not detectable. The average partition coefficients across all measurable conditions were found to be $(3.1 \pm 0.4) \times 10^5$ for 2EHN, $(1.7 \pm 0.2) \times 10^6$ for HPN, and $(2.1 \pm 0.3) \times 10^7$ for HHN ($\pm 1\sigma$), indicated by the solid lines in Figure 6.7.

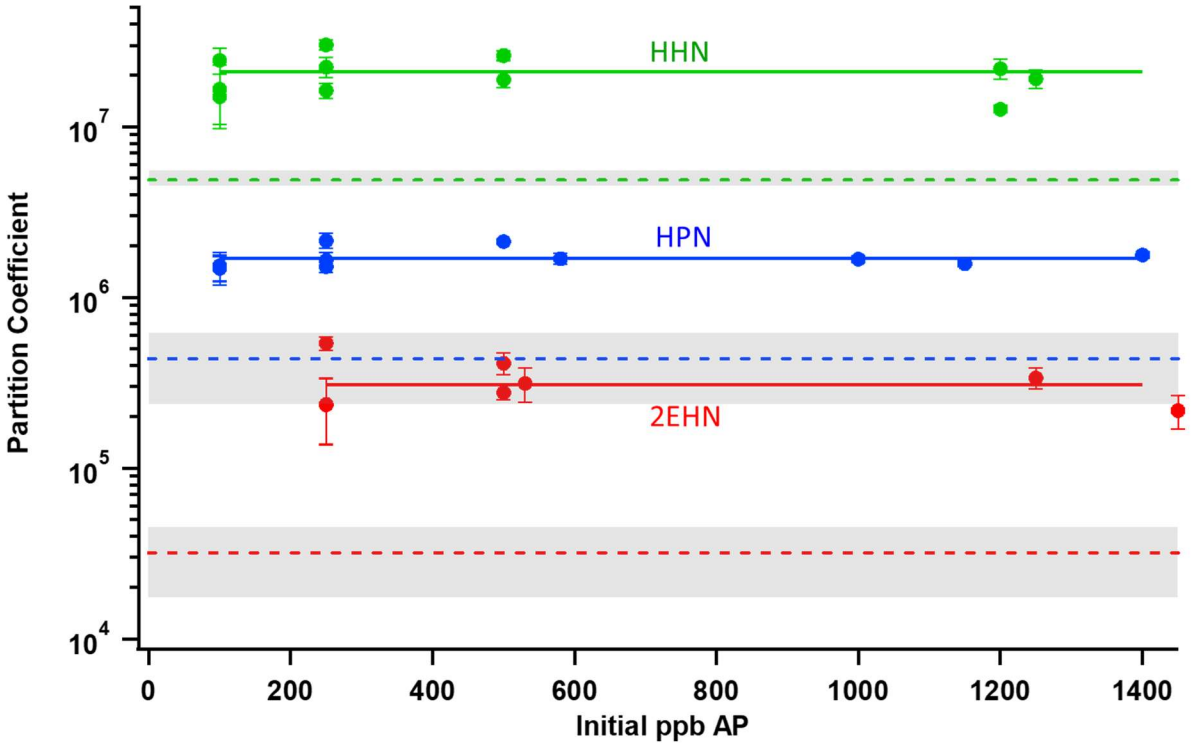

Figure 6.7: Partition coefficients (closed circles) for particles formed from AP ozonolysis in the presence of 100 ppb CH as an OH scavenger and 5.7 ppm 2EHN, 4.6 ppm HPN, or 0.21 ppm HHN. Error bars are ± 2σ from the absolute uncertainty in the AMS. The dashed lines show the partition coefficients measured for the equilibrium partitioning of ~190 ppm 2EHN, ~ 160 ppm HPN, or ~7 ppm HHN into thin films of particles formed from 250 ppb AP and 100 ppb CH, with grey boxes showing ± 1σ from the average of at least three experiments. The 2EHN signal in the particles was not detectable at 100 ppb initial AP.

One possible explanation for the lack of dependence on precursor AP concentration or mass loading in the partition coefficients is that the partitioning of the organic nitrates could have reached equilibrium. SOA particles from AP ozonolysis are known to become less viscous when formed at higher initial AP concentrations/higher mass loadings.[195, 207] Thus, if equilibrium partitioning were to be reached, it would be more probable for particles formed at the higher initial AP concentrations. All SOA particles formed in the current study were observed to exhibit significant bounce patterns in the impactor, especially the higher initial AP concentrations due to larger mass loadings (Figure 6.5). Furthermore, the SOA particles with

organic nitrate incorporated in them also exhibited clear bounce patterns, again especially at the higher initial AP concentrations. Additionally, Vander Wall *et al.*[220] showed in a previous study that the partition coefficients for these organic nitrates incorporated into particles *during* growth (at 250 ppb $[AP]_o$) were *higher* than the equilibrium partition coefficients for these nitrates into thin films of impacted particles (i.e., after growth) that reached equilibrium between ~4 to 20 min with gas phase concentrations near the saturation vapor pressure.

Chapter 5 showed that when particles formed from 250 ppb AP in the presence of CH as an OH scavenger were exposed to gas phase 2EHN *after* growth in a glass flow tube B, using a similar gas phase concentration to those used here in the flow reactor, the amount of 2EHN in the particles was undetectable in the time frame of 7 minutes. Similar results were seen when particles formed under the same conditions were exposed to ~6.5 ppm of gas phase HPN in the glass flow tube B for 7 min, again resulting in undetectable levels of particulate organic nitrate. This indicates that in the large flow reactor, the detectable organic nitrate in the particles *during* growth was still above the expected equilibrium partitioning value.

A possible explanation for the constant partition coefficients as a function of initial AP concentration is that the relative rate of uptake for the organic nitrates and the gaseous ozonolysis products, represented by P_{SOA}, remains constant. P_{SOA} is a bulk designation for all products derived from the ozonolysis of AP that may contribute to particle formation and growth and is representative of what forms the SOA. As the concentration of AP increases, P_{SOA} is anticipated to increase. Thus, the number of collisions of P_{SOA} per cm^2 of particle surface area, and hence its uptake, will increase (creating higher SOA mass loading). However, the $RONO_2$

collisions per cm^2 of particle surface area should remain the same, since the $RONO_2$ gas phase concentrations remain constant. One might expect that as more P_{SOA} collides and is taken up into the particles, the particulate $RONO_2$ signal per L of SOA would decrease due to dilution. This is in contrast to the observed constant $RONO_2$ concentration in SOA across the studied reaction conditions/initial AP concentrations when OH is scavenged (Figure 6.6b). However, if P_{SOA} contributes to the incorporation of $RONO_2$ by acting as a burying species, as the concentration of P_{SOA} increases the trapping of $RONO_2$ in the particles will also increase, counterbalancing the effects of dilution and resulting in a constant particulate $RONO_2$ concentration. To explore this in more detail, the effective uptake coefficients for the organic nitrates were estimated using Equation 2.10-Equation 2.12 and the average $RONO_2$ concentration per L of SOA (Figure 6.6b), and are shown in Figure 6.8 for initial concentrations of 250 ppb O_3 and AP from 100-1450 ppb. The effective net uptake coefficients for the incorporation of the organic nitrates into the particles (γ_{RONO2}) were found to increase with initial AP concentration (Figure 6.8) with approximate values from $(0.2\text{-}4) \times 10^{-3}$ for HHN, $(0.1\text{-}3) \times 10^{-4}$ for HPN, and $(2\text{-}5) \times 10^{-5}$ for 2EHN.

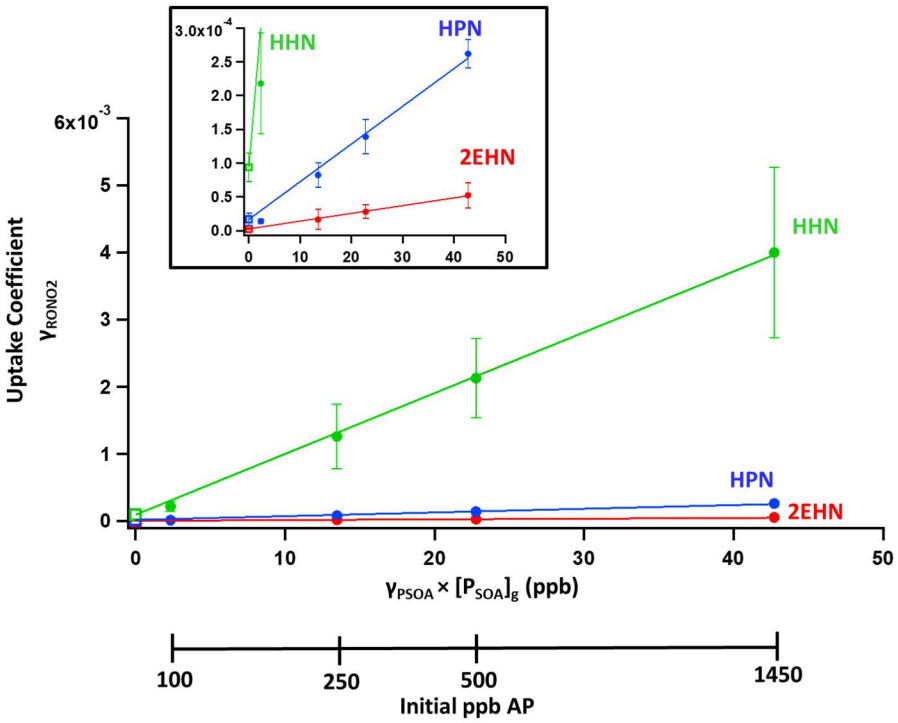

Figure 6.8: Effective uptake coefficients for the uptake of organic nitrates into the particles (γ_{RONO2}) versus the product of the uptake coefficient of P_{SOA} (γ_{PSOA}) and the concentration of P_{SOA} (ppb). The inset shows an expanded view for HPN and 2EHN. The open boxes at $\gamma_{PSOA} \times [P_{SOA}]_g = 0$ are the uptake coefficient measured from thin films of impacted particles. Error bars are ± 1σ propagated from the average of at least 3 experiments. Lines are linear fits to the data points.

In the absence of any P_{SOA} from the ozonolysis of AP (i.e. as $[P_{SOA}]_g$ approaches 0 ppb), the uptake coefficient is expected to be the γ_{RONO2} for the organic nitrate alone based solely on the collisions with the particle surface per cm^2 (in the absence of any enhancement due to burying), which was measured previously as the uptake coefficient onto thin films of impacted particles (Table 3.1). These values are included as the y-intercept in Figure 6.8, and are in good agreement with the trend in uptake coefficients. This analysis conveys the ability of the burying mechanism to increase uptake beyond that which is expected to occur through collisional uptake

alone. However, it ignores potential changes in gas and particle phase composition at lower $[AP]_0$,[203-207, 222-223] which are examined below.

The effectiveness of burying the organic nitrate depends not only on the concentration of P_{SOA}, but also on the nature of P_{SOA} as a burying species, which may vary depending on the reaction conditions. Previously, Claflin *et al.*[222] showed that SOA formed at low RH under a high-[VOC] condition (1 ppm AP, 2 ppm O_3) had a different distribution of functional groups than SOA formed under a low-[VOC] condition (10 ppb AP, 300 ppb O_3), with the latter having a higher contribution from peroxides, while most other functional groups were higher in the former scenario. Additionally, Molteni *et al.*[204] showed that the distribution of highly oxygenated organic molecules (HOMs) varied with the reaction conditions, and larger contributions from dimers occurred at higher initial AP concentrations/as more AP was reacted away.

To probe this for the reaction conditions studied here, the MCM (v3.3.1)[165] model was used to predict changes in the product distribution. An updated mechanism[167] was used that includes dimer formation from RO_2-RO_2 chemistry, where the RO_2 comes from oxidation steps within the original MCM as well as autoxidation processes producing more highly-oxidized RO_2 species. As the initial concentration of AP increases and more AP is reacted away, the total amount of products also increases, with or without the new implementation added (Figure 6.9a and Figure 6.9b). The total concentration of all C_1-C_{20} products predicted by the MCM with dimers added and the concentration of the C_{10}-C_{20} products are listed in Table 6.1. The C_{14}-C_{17} products were omitted from the graph due to their negligible concentrations, but are accounted

for in Table 6.1. Across all conditions there were small changes in the distribution of the products, as seen by Figure 6.9c and Figure 6.9d. The percent contribution from the $C_{14\text{-}20}$ dimers to the total products was about the same for the 100 ppb AP condition (~8%) as the 1.5 ppm AP condition (~10%). Thus, the steady increase in concentrations of products that bury the organic nitrates is likely more important than the change in product distributions, which is minimal.

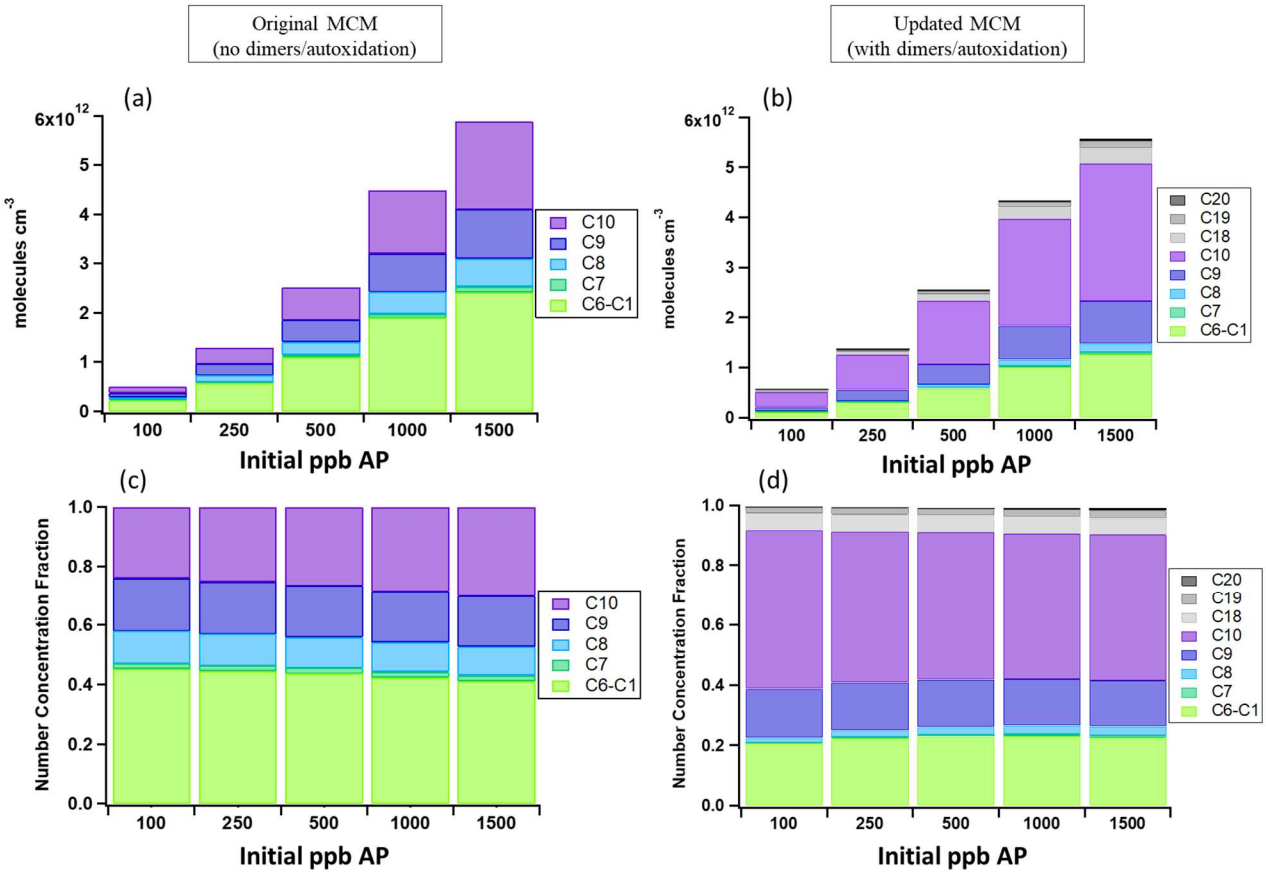

Figure 6.9: AP oxidation product distribution from the MCM after 7 minutes reaction in the presence of CH (100ppm) separated by carbon number for species with more than 5 carbons. a) The stable gas phase molecules formed based on the original MCM mechanism, b) the stable gas phase molecules formed using the updated MCM mechanism including autooxidation processes and the formation of dimers, c) the normalized fraction of stable products without dimers (original MCM mechanism), and d) the normalized fraction of stable products with dimers added.

Table 6.1: Concentrations of stable gas phase products (ppb) formed, predicted by the MCM with dimer formation added.

$[AP]_0$ (ppb)	MCM predicted C_1-C_{20} total products (ppb)	MCM predicted C_{10}-C_{20} products (ppb)	% C_{10}-C_{20} of total
100	23	14	61%
250	56	33	59%
500	104	61	59%
1500	229	134	59%

Although only relatively small changes were observed in the overall product distribution (in terms of number of carbons per molecule), some changes in composition were seen from the MCM results when the level of oxidation was taken into account. Figure 6.10 shows the distribution of C_{10} products separated by the number of oxygens for all conditions when autoxidation/dimer formation was added into the MCM. Although the majority (~50%) of the C_{10} species remain $C_{10}O_5$ across the conditions, as the concentration of AP increases, so does the contribution of less-oxygenated species, also indicated by the decrease in the average O:C of the C_{10} species from 0.65 at 100 ppb AP to 0.55 at 1.5 ppm AP. This is consistent with the AMS measurements of particle O:C, discussed below.

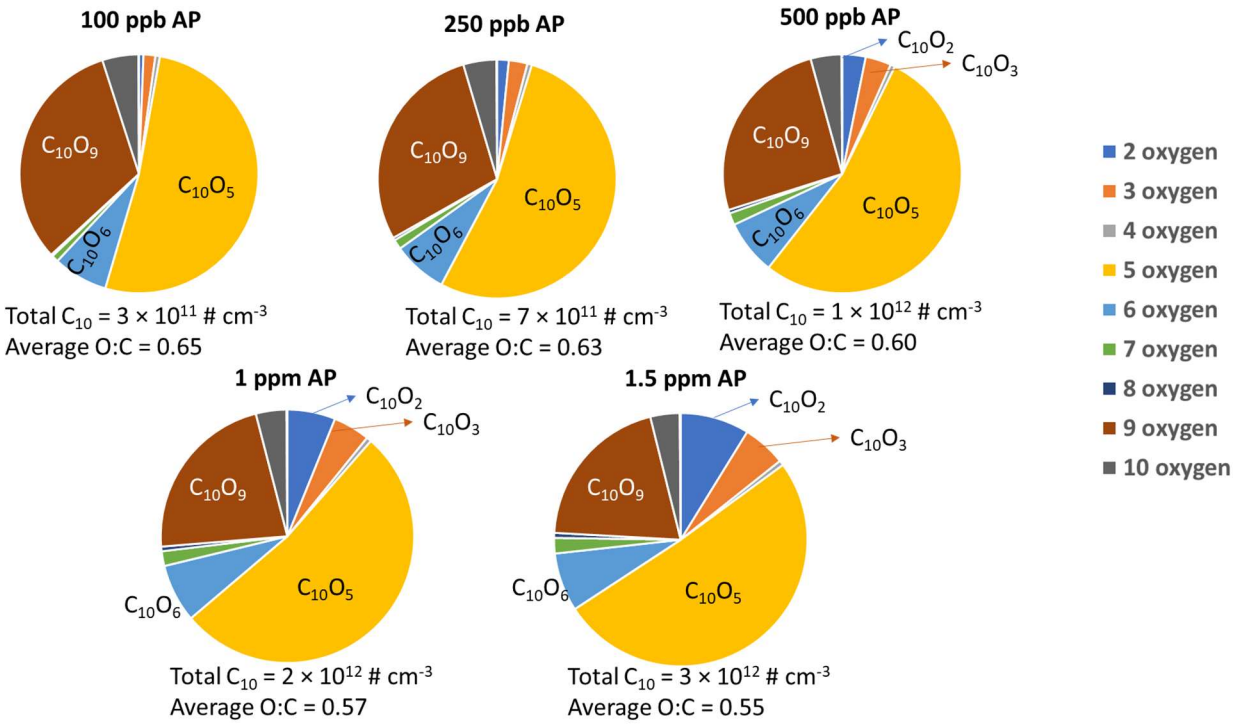

Figure 6.10: Percent contribution for the C_{10} species separated by the number of oxygens for all initial concentrations of α-pinene. Also shown are the total concentration of the C_{10} species at each condition, and the average O:C ratio for the C_{10} products.

Following a kinetic burying mechanism, for an incoming organic nitrate molecule to be incorporated into the particles, it must have a sufficient residence time on the particle surface such that a colliding low volatility ozonolysis product (represented by P_{SOA}) can efficiently bury it. The number of collisions cm^{-2} s^{-1} for P_{SOA} with the particle surface can be estimated using gas kinetic theory and Equation 6.1:

$$\text{Collisions cm}^{-2}\text{s}^{-1} = [P_{SOA}]_g \times \sqrt{\frac{RT}{2\pi M}} \qquad \text{Equation 6.1}$$

where $[P_{SOA}]_g$ is the concentration of ozonolysis products that make up the SOA matrix, and M is the average molecular weight of P_{SOA} (assumed to be 200 g $mole^{-1}$).[141-142] The $[P_{SOA}]_g$ was

estimated from the $\gamma_{PSOA} \times [P_{SOA}]_g$ using Equation 2.11 and the measured SOA mass loading, assuming a γ_{PSOA} of one. If the inverse of the collision frequency is an estimate of the time between collisions of a burying P_{SOA} species with 1 cm^2 of particle surface, the time between collisions can be calculated. Since a γ_{PSOA} of one is an assumption, the time between collisions is considered relative time. Figure 6.11 shows the relative time between collisions of P_{SOA} with the particle surface, normalized to that estimated for 100 ppb AP.

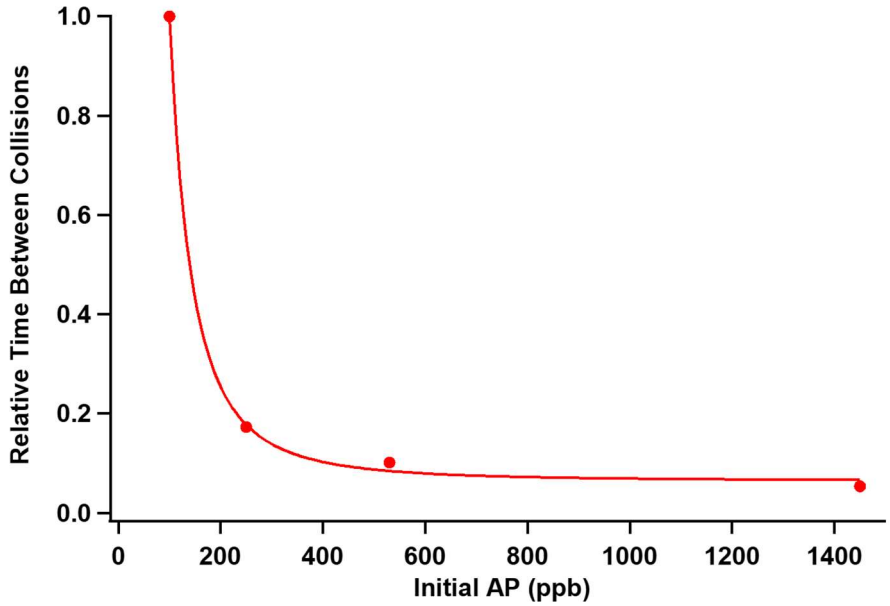

Figure 6.11: Relative time between collisions for an incoming burying species (P_{SOA}) colliding with the particles formed as a function of the initial concentration of AP. Values are normalized to the 100 ppb AP condition. The solid line is a best fit to guide the eye.

The relative time between collisions for a burying species with the particles is much larger at 100 ppb AP than it is for the other reaction conditions/initial concentrations of AP, ~5.8 times longer than that for the 250 ppb AP condition. Between the 250 to 530 ppb and the 530 to 1450 ppb AP conditions, the relative time between collisions decreased by ~1.7 and 1.8 times, respectively. As seen in Table 6.1, the total concentrations of gas phase products predicted by

the MCM increases by a factor of ~2 between each reaction condition, which is in good agreement with the change in relative time between collisions except in the case of the 100 ppb AP condition. The estimated relative time between collisions assumed a γ_{PSOA} of one for all reaction conditions. However, if γ_{PSOA} is much lower for the 100 ppb AP condition, this would increase the estimated collision frequency and thus lower the time between collisions.

The hydroxy nitrates were taken up at all reaction conditions, indicating that the average residence time for the HPN and HHN on the particle surface was sufficiently long that they could be buried by an incoming P_{SOA} molecule. As discussed previously, particulate 2EHN was undetectable at the 100 ppb AP condition. This may be explained by a residence time of the 2EHN on the particle surface that is insufficient to allow for burying at this condition. 2EHN has the smallest hydrogen-bonding capacity when compared to the hydroxy nitrates, which as shown previously has implications for the initial uptake coefficient onto films of impacted particles (Chapter 3). Additionally, the experimentally determined composition of the particles, discussed below, was also slightly different at 100 ppb AP when compared to the particles formed at the rest of the reaction conditions, exhibiting a higher degree of oxygenation (higher O:C). This supports the idea that there were insufficient favorable interactions of 2EHN with the particle surface, and thus shorter surface residence time for this molecule to be taken up/buried at this condition.

HR-ToF-AMS was used to detect changes in particle composition. The average O:C ratio of the SOA slightly decreased from 0.46 to 0.42 as the AP initial concentration increased, though the overall change was small, as shown in Table 6.2. Figure 6.12 shows the intensity

ratio of CO_2^+ (*m/z* 44) to either $C_4H_7^+$ (*m/z* 55, Figure 6.12a) or $C_2H_3O^+$ (*m/z* 43, Figure 6.12b), as well as the ratio of CO_2^+ to HROrg plotted against the ratio of $C_2H_3O^+$ to HROrg (Figure 6.12c). CO_2^+ is an indicator of more-oxygenated species such as acids and peroxides,[75, 200-201] while $C_4H_7^+$ and $C_2H_3O^+$ are indicators of less-oxygenated species within the particles. While there was little to no change from 250 ppb AP and higher, the 100 ppb AP condition exhibited a larger contribution from the more-oxygenated CO_2^+ fragment. The MCM similarly predicted a higher O:C for the 100 ppb AP condition, though a consistent decrease in the average O:C in the C_{10} species was seen as the initial AP increased. However, the MCM is a prediction of all gas-phase species, which may explain this difference from the particle-phase measurements.

Table 6.2: Oxygen-to-Carbon ratio for SOA formed in the flow reactor in the presence of an OH scavenger, at 7 minutes reaction time. Error bars are ± 1σ from the average of three experiments.

$[AP]_0$ (ppb)	O:C (± 1σ)
100	0.46 ± 0.01
250	0.43 ± 0.02
500-530	0.43 ± 0.02
700-1450	0.42 ± 0.01

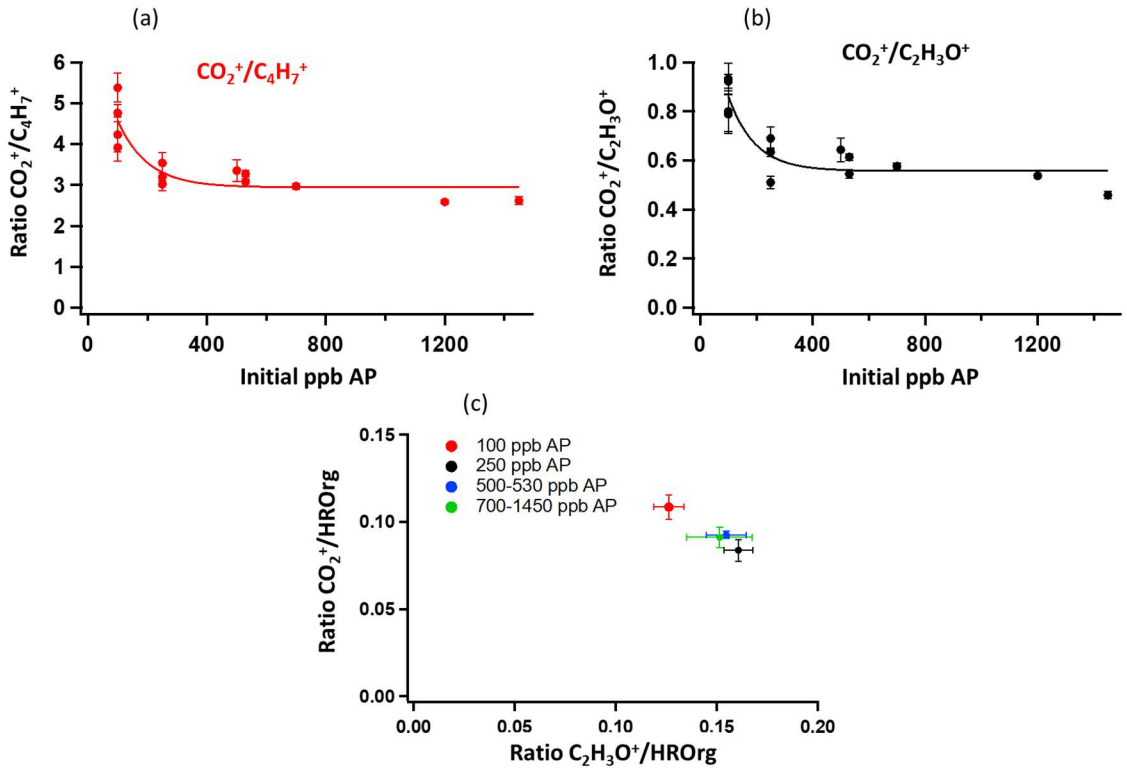

Figure 6.12: The AMS fragment ratio for CO_2^+ to a) $C_4H_7^+$ and b) $C_2H_3O^+$ at each initial concentration of AP with 100 ppm CH as an OH scavenger, and c) the ratio of CO_2^+ to HROrg versus the ratio of $C_2H_3O^+$ to HROrg. Error bars in a) and b) are ± 1σ from the absolute uncertainty in the AMS, and error bars in c) are ± 1σ from the average of at least three experiments. Solid lines are best fits to guide the eye.

The change in the average O:C is consistent with other observations at variable AP concentrations/mass loading. Shilling *et al.*[203] showed that for SOA particles formed from AP ozonolysis using 1-butanol as an OH scavenger, the changes in the particle O:C and composition were more pronounced at smaller mass loadings, with higher O:C as the mass loading decreased, consistent with the results shown here. The slightly more-oxygenated composition at 100 ppb AP could be consistent with the decrease in the partition coefficient of 2EHN, the least-oxygenated organic nitrate studied here. The 2EHN should have a smaller affinity for these particles due to its less-polar alkyl nature and smaller hydrogen-bonding capacity compared to

the hydroxy-nitrates,[177] which may result in an insufficient surface residence time to be incorporated into the particles by a burying species at this condition. HHN and HPN are more oxygenated with larger hydrogen-bonding capacities, and thus may have a stronger interaction with the particles such that they did not show this change at the lowest concentration of AP.

6.3 Conclusions

Results from this study show that reactions with OH can increase the total amount of organic nitrate fraction of the SOA through the formation of lower volatility multi-functional organic nitrates. In the presence of an OH-scavenger, the partition coefficients of all three studied parent organic nitrates showed no dependence on precursor AP concentration/particle mass loading (with the exception of 2EHN, which was undetectable in the particles at the lowest concentration of AP studied here), while the effective uptake coefficients for the organic nitrate into the particles (γ_{RONO2}) increased with AP concentration/mass loading. In the absence of any P_{SOA} from the ozonolysis of AP, the uptake coefficient approaches that of the organic nitrate alone based solely on the collisions with the particle surface, which was the measured uptake coefficient onto impacted particles (Table 3.1). Model studies predicted that while the distribution of products did not significantly change across the conditions studied here, the total concentration of products increased with the AP concentration, as expected. The similar partition coefficients across the conditions and the increase in effective uptake coefficients for the organic nitrates are explained by a kinetically-controlled burying mechanism.[220] Nevertheless, the nature of the gas phase molecule with the interface of the particle will also play a significant role in the uptake, as at the 100 ppb AP condition the less polar alkyl nitrate 2EHN

was not quantifiable in the particles, likely because of a smaller affinity for the particles (which were found to be smaller and more oxygenated than the other conditions).

The results here indicate that the interaction of gaseous species with highly viscous SOA particles in the atmosphere to contribute to particle growth depends on both the nature of the gas phase and that of the particle phase. The formation of large, low volatility species in the gas phase can facilitate the incorporation of more volatile molecules at amounts greater than expected based on equilibrium partitioning through a kinetically controlled burying mechanism. Figure 6.13 depicts such a mechanism for a semisolid particle, where a gas phase molecule (G, such as an organic nitrate) would be adsorbed on the surface of an SOA particle for a long enough time that it can be buried by an incoming oxidation product from AP (or P_{SOA} molecule). This burying is in competition with scattering or desorption/evaporation. The burying process can help trap the organic nitrate within the particle, reducing its re-evaporation into the gas phase and thus incorporating more within the particle phase than would be expected based on equilibrium partitioning.

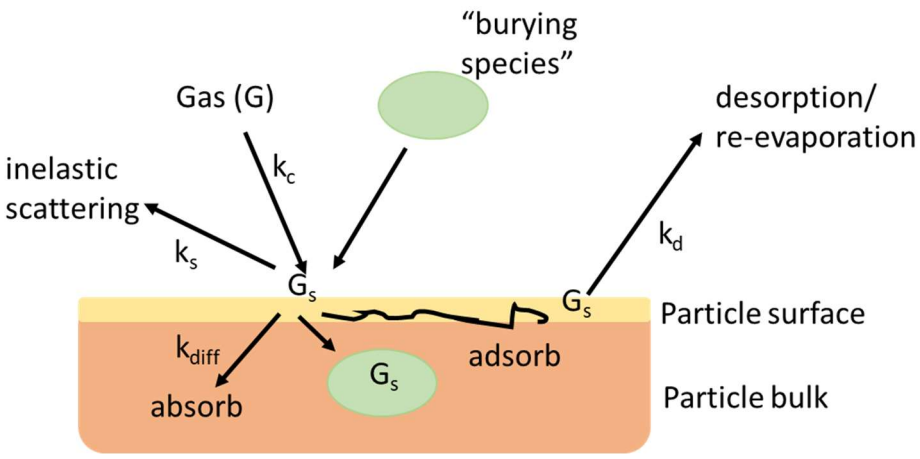

Figure 6.13: A schematic of the interactions between a gas-phase species (G), representative of the organic nitrate in our study with an SOA particle. Once G is on the particle surface, the burying species (P_{SOA} oxidation products from AP ozonolysis) facilitates the incorporation of G into the particle by hindering desorption/re-evaporation.

This kinetically-controlled burying mechanism was examined for semi-solid particles formed under dry conditions. In the ambient atmosphere, the relative humidity (RH) can vary. Increasing RH is known to decrease particle viscosity, resulting in more liquid-like particles.[196-198] As particle viscosity decreases, diffusion into the bulk becomes more rapid,[54, 61] and the contribution of the burying mechanism (a process driven by surface interactions) likely decreases. Expanding this work to study the effects of varying RH on the incorporation of tracers into the particle phase and the effects of the burying mechanism will help provide insight into the importance of this mechanism under ambient atmospheric conditions throughout the globe.

References

1. Finlayson-Pitts, B. J.; Pitts, J. N., *Chemistry of the Upper and Lower Atmosphere: Theory, Experiments, and Applications*. Academic Press: **2000**.

2. Seinfeld, J. H.; Pandis, S. N., *Atmospheric Chemistry and Physics: From Air Pollution to Climate Change*. Wiley: **2006**.

3. Pope, C. A.; Dockery, D. W., Health effects of fine particulate air pollution: lines that connect. *J. Air Waste Manage.* **2006**, *56* (6), 709-742.

4. Poschl, U., Atmospheric aerosols: Composition, transformation, climate and health effects. *Angew. Chem. Int. Edit.* **2005**, *44* (46), 7520-7540.

5. Mauderly, J. L.; Chow, J. C., Health effects of organic aerosols. *Inhal. Toxicol.* **2008**, *20* (3), 257-288.

6. Landrigan, P. J.; Fuller, R.; Acosta, N. J. R.; Adeyi, O.; Arnold, R.; Basu, N.; Baldé, A. B.; Bertollini, R.; Bose-O'Reilly, S.; Boufford, J. I.; Breysse, P. N.; Chiles, T.; Mahidol, C.; Coll-Seck, A. M.; Cropper, M. L.; Fobil, J.; Fuster, V.; Greenstone, M.; Haines, A.; Hanrahan, D.; Hunter, D.; Khare, M.; Krupnick, A.; Lanphear, B.; Lohani, B.; Martin, K.; Mathiasen, K. V.; McTeer, M. A.; Murray, C. J. L.; Ndahimananjara, J. D.; Perera, F.; Potočnik, J.; Preker, A. S.; Ramesh, J.; Rockström, J.; Salinas, C.; Samson, L. D.; Sandilya, K.; Sly, P. D.; Smith, K. R.; Steiner, A.; Stewart, R. B.; Suk, W. A.; van Schayck, O. C. P.; Yadama, G. N.; Yumkella, K.; Zhong, M., The Lancet Commission on pollution and health. *Lancet* **2018**, *391* (10119), 462-512.

7. Mannucci, P. M.; Harari, S.; Martinelli, I.; Franchini, M., Effects on health of air pollution: a narrative review. *Intern. Emerg. Med.* **2015**, *10* (6), 657-662.

8. Nel, A., Air pollution-related illness: effects of particles. *Science* **2005**, *308* (5723), 804-806.

9. Heal, M. R.; Kumar, P.; Harrison, R. M., Particles, air quality, policy and health. *Chem. Soc. Rev.* **2012**, *41* (19), 6606-6630.

10. Hinds, W. C., *Aerosol Technology: Properties, Behavior, and Measurement of Airborne Particles*. John Wiley & Sons: **1982**.

11. Singh, A.; Bloss, W. J.; Pope, F. D., 60 years of UK visibility measurements: impact of meteorology and atmospheric pollutants on visibility. *Atmos. Chem. Phys.* **2017**, *17* (3), 2085-2101.

12. Farmer, D. K.; Cappa, C. D.; Kreidenweis, S. M., Atmospheric Processes and Their Controlling Influence on Cloud Condensation Nuclei Activity. *Chem. Rev.* **2015**, *115* (10), 4199-4217.

13. Shrivastava, M.; Cappa, C. D.; Fan, J.; Goldstein, A. H.; Guenther, A. B.; Jimenez, J. L.; Kuang, C.; Laskin, A.; Martin, S. T.; Ng, N. L.; Petäjä, T.; Pierce, J. R.; Rasch, P. J.; Roldin, P.; Seinfeld, J. H.; Shilling, J.; Smith, J. N.; Thornton, J. A.; Volkamer, R.; Wang, J.; Worsnop, D. R.; Zaveri, R. A.; Zelenyuk, A.; Zhang, Q., Recent advances in understanding secondary organic aerosol: implications for global climate forcing. *Rev. Geophys.* **2017**, *55* (2), 509-559.

14. IPCC, 2013: Summary for Policymakers. In *Climate Change 2013: The Physical Science Basis. Contribution of Working Group I to the Fifth Assessment Report of the Intergovernmental Panel on Climate Change* Stocker, T. F.; Qin, D.; Plattner, G.-K.; Tignor, M.; Allen, S. K.; Boschung, J.; Nauels, A.; Xia, Y.; Bex, V.; Midgley, P. M., Eds. Cambridge University Press: Cambridge, United Kingdom And New York, NY, USA, **2013**.

15. Kanakidou, M.; Seinfeld, J. H.; Pandis, S. N.; Barnes, I.; Dentener, F. J.; Facchini, M. C.; Van Dingenen, R.; Ervens, B.; Nenes, A.; Nielsen, C. J.; Swietlicki, E.; Putaud, J. P.; Balkanski, Y.; Fuzzi, S.; Horth, J.; Moortgat, G. K.; Winterhalter, R.; Myhre, C. E. L.; Tsigaridis, K.; Vignati, E.; Stephanou, E. G.; Wilson, J., Organic aerosol and global climate modelling: a review. *Atmos. Chem. Phys.* **2005**, *5*, 1053-1123.

16. Putaud, J. P.; Van Dingenen, R.; Alastuey, A.; Bauer, H.; Birmili, W.; Cyrys, J.; Flentje, H.; Fuzzi, S.; Gehrig, R.; Hansson, H. C.; Harrison, R. M.; Herrmann, H.; Hitzenberger, R.; Hüglin, C.; Jones, A. M.; Kasper-Giebl, A.; Kiss, G.; Kousa, A.; Kuhlbusch, T. A. J.; Löschau, G.; Maenhaut, W.; Molnar, A.; Moreno, T.; Pekkanen, J.; Perrino, C.; Pitz, M.; Puxbaum, H.; Querol, X.; Rodriguez, S.; Salma, I.; Schwarz, J.; Smolik, J.; Schneider, J.; Spindler, G.; ten Brink, H.; Tursic, J.; Viana, M.; Wiedensohler, A.; Raes, F., A European aerosol phenomenology – 3: Physical and chemical characteristics of particulate matter from 60 rural, urban, and kerbside sites across Europe. *Atmos. Environ.* **2010**, *44* (10), 1308-1320.

17. Minguillón, M. C.; Querol, X.; Baltensperger, U.; Prévôt, A. S. H., Fine and coarse PM composition and sources in rural and urban sites in Switzerland: Local or regional pollution? *Sci. Total Environ.* **2012**, *427-428*, 191-202.

18. Jimenez, J. L.; Canagaratna, M. R.; Donahue, N. M.; Prevot, A. S. H.; Zhang, Q.; Kroll, J. H.; DeCarlo, P. F.; Allan, J. D.; Coe, H.; Ng, N. L.; Aiken, A. C.; Docherty, K. S.; Ulbrich, I. M.; Grieshop, A. P.; Robinson, A. L.; Duplissy, J.; Smith, J. D.; Wilson, K. R.; Lanz, V. A.; Hueglin, C.; Sun, Y. L.; Tian, J.; Laaksonen, A.; Raatikainen, T.; Rautiainen, J.; Vaattovaara, P.; Ehn, M.; Kulmala, M.; Tomlinson, J. M.; Collins, D. R.; Cubison, M. J.; Dunlea, J.; Huffman, J. A.; Onasch, T. B.; Alfarra, M. R.; Williams, P. I.; Bower, K.; Kondo, Y.; Schneider, J.; Drewnick, F.; Borrmann, S.; Weimer, S.; Demerjian, K.; Salcedo, D.; Cottrell, L.; Griffin, R.; Takami, A.; Miyoshi, T.; Hatakeyama, S.; Shimono, A.; Sun, J. Y.; Zhang, Y. M.; Dzepina, K.; Kimmel, J. R.; Sueper, D.; Jayne, J. T.; Herndon, S. C.; Trimborn, A. M.; Williams, L. R.; Wood, E. C.; Middlebrook, A. M.; Kolb, C. E.; Baltensperger, U.; Worsnop, D. R., Evolution of Organic Aerosols in the Atmosphere. *Science* **2009**, *326* (5959), 1525.

19. Riipinen, I.; Yli-Juuti, T.; Pierce, J. R.; Petäjä, T.; Worsnop, D. R.; Kulmala, M.; Donahue, N. M., The contribution of organics to atmospheric nanoparticle growth. *Nat. Geosci.* **2012**, *5*, 453.

20. Zhang, Q.; Jimenez, J. L.; Canagaratna, M. R.; Allan, J. D.; Coe, H.; Ulbrich, I.; Alfarra, M. R.; Takami, A.; Middlebrook, A. M.; Sun, Y. L.; Dzepina, K.; Dunlea, E.; Docherty, K.; DeCarlo, P. F.; Salcedo, D.; Onasch, T.; Jayne, J. T.; Miyoshi, T.; Shimono, A.; Hatakeyama, S.; Takegawa, N.; Kondo, Y.; Schneider, J.; Drewnick, F.; Borrmann, S.; Weimer, S.; Demerjian, K.; Williams, P.; Bower, K.; Bahreini, R.; Cottrell, L.; Griffin, R. J.; Rautiainen, J.; Sun, J. Y.; Zhang, Y. M.; Worsnop, D. R., Ubiquity and dominance of oxygenated species in organic aerosols in anthropogenically-influenced Northern Hemisphere midlatitudes. *Geophys. Res. Letters* **2007**, *34* (13).

21. Rogge, W. F.; Mazurek, M. A.; Hildemann, L. M.; Cass, G. R.; Simoneit, B. R. T., Quantification of urban organic aerosols at a molecular level: Identification, abundance and seasonal variation. *Atmos. Environ. A, Gen. Top.* **1993**, *27* (8), 1309-1330.

22. Kang, M.; Ren, L.; Ren, H.; Zhao, Y.; Kawamura, K.; Zhang, H.; Wei, L.; Sun, Y.; Wang, Z.; Fu, P., Primary biogenic and anthropogenic sources of organic aerosols in Beijing, China: Insights from saccharides and n-alkanes. *Environ. Pollut.* **2018**, *243*, 1579-1587.

23. Rinaldi, M.; Decesari, S.; Finessi, E.; Giulianelli, L.; Carbone, C.; Fuzzi, S.; O'Dowd, C. D.; Ceburnis, D.; Facchini, M. C., Primary and secondary organic marine aerosol and oceanic biological activity: Recent results and new perspectives for future studies. *Adv. Meteorol.* **2010**, *2010*.

24. Gantt, B.; Meskhidze, N., The physical and chemical characteristics of marine primary organic aerosol: a review. *Atmos. Chem. Phys.* **2013**, *13* (8), 3979-3996.

25. Nielsen, I. E.; Skov, H.; Massling, A.; Eriksson, A. C.; Dall'Osto, M.; Junninen, H.; Sarnela, N.; Lange, R.; Collier, S.; Zhang, Q.; Cappa, C. D.; Nøjgaard, J. K., Biogenic and anthropogenic sources of aerosols at the High Arctic site Villum Research Station. *Atmos. Chem. Phys.* **2019**, *19* (15), 10239-10256.

26. Samaké, A.; Bonin, A.; Jaffrezo, J. L.; Taberlet, P.; Weber, S.; Uzu, G.; Jacob, V.; Conil, S.; Martins, J. M. F., High levels of primary biogenic organic aerosols in the atmosphere in summer are driven by only a few microbial taxa from the leaves of surrounding plants. *Atmos. Chem. Phys. Discuss.* **2020**, *2020*, 1-23.

27. Ziemann, P. J.; Atkinson, R., Kinetics, products, and mechanisms of secondary organic aerosol formation. *Chem. Soc. Rev.* **2012**, *41* (19), 6582-6605.

28. Seinfeld, J. H.; Pankow, J. F., Organic Atmospheric Particulate Material. *Annu. Rev. Phys. Chem.* **2003**, *54* (1), 121-140.

29. Kroll, J. H.; Seinfeld, J. H., Chemistry of secondary organic aerosol: Formation and evolution of low-volatility organics in the atmosphere. *Atmos. Environ.* **2008**, *42* (16), 3593-3624.

30. Hallquist, M.; Wenger, J. C.; Baltensperger, U.; Rudich, Y.; Simpson, D.; Claeys, M.; Dommen, J.; Donahue, N. M.; George, C.; Goldstein, A. H.; Hamilton, J. F.; Herrmann, H.; Hoffmann, T.; Iinuma, Y.; Jang, M.; Jenkin, M. E.; Jimenez, J. L.; Kiendler-Scharr, A.;

Maenhaut, W.; McFiggans, G.; Mentel, T. F.; Monod, A.; Prévôt, A. S. H.; Seinfeld, J. H.; Surratt, J. D.; Szmigielski, R.; Wildt, J., The formation, properties and impact of secondary organic aerosol: current and emerging issues. *Atmos. Chem. Phys.* **2009**, *9* (14), 5155-5236.

31. Kansal, A., Sources and reactivity of NMHCs and VOCs in the atmosphere: A review. *J. Hazard. Mater.* **2009**, *166* (1), 17-26.

32. Eggersdorfer, M., Terpenes. In *Ullmann's Encyclopedia of Industrial Chemistry*, **2000**.

33. Guenther, A.; Geron, C.; Pierce, T.; Lamb, B.; Harley, P.; Fall, R., Natural emissions of non-methane volatile organic compounds, carbon monoxide, and oxides of nitrogen from North America. *Atmos. Environ.* **2000**, *34* (12), 2205-2230.

34. Guenther, A.; Hewitt, C. N.; Erickson, D.; Fall, R.; Geron, C.; Graedel, T.; Harley, P.; Klinger, L.; Lerdau, M.; Mckay, W. A.; Pierce, T.; Scholes, B.; Steinbrecher, R.; Tallamraju, R.; Taylor, J.; Zimmerman, P., A global model of natural volatile organic compound emissions. *J. Geophys. Res. Atmos.* **1995**, *100* (D5), 8873-8892.

35. Geron, C.; Rasmussen, R.; R. Arnts, R.; Guenther, A., A review and synthesis of monoterpene speciation from forests in the United States. *Atmos. Environ.* **2000**, *34* (11), 1761-1781.

36. Rinne, H. J. I.; Guenther, A. B.; Greenberg, J. P.; Harley, P. C., Isoprene and monoterpene fluxes measured above Amazonian rainforest and their dependence on light and temperature. *Atmos. Environ.* **2002**, *36* (14), 2421-2426.

37. Koch, S.; Winterhalter, R.; Uherek, E.; Kolloff, A.; Neeb, P.; Moortgat, G. K., Formation of new particles in the gas-phase ozonolysis of monoterpenes. *Atmos. Environ.* **2000**, *34* (23), 4031-4042.

38. Zhao, D. F.; Kaminski, M.; Schlag, P.; Fuchs, H.; Acir, I. H.; Bohn, B.; Häseler, R.; Kiendler-Scharr, A.; Rohrer, F.; Tillmann, R.; Wang, M. J.; Wegener, R.; Wildt, J.; Wahner, A.; Mentel, T. F., Secondary organic aerosol formation from hydroxyl radical oxidation and ozonolysis of monoterpenes. *Atmos. Chem. Phys.* **2015**, *15* (2), 991-1012.

39. Kolb, C. E.; Cox, R. A.; Abbatt, J. P. D.; Ammann, M.; Davis, E. J.; Donaldson, D. J.; Garrett, B. C.; George, C.; Griffiths, P. T.; Hanson, D. R.; Kulmala, M.; McFiggans, G.; Pöschl, U.; Riipinen, I.; Rossi, M. J.; Rudich, Y.; Wagner, P. E.; Winkler, P. M.; Worsnop, D. R.; O' Dowd, C. D., An overview of current issues in the uptake of atmospheric trace gases by aerosols and clouds. *Atmos. Chem. Phys.* **2010**, *10* (21), 10561-10605.

40. Pöschl, U.; Rudich, Y.; Ammann, M., Kinetic model framework for aerosol and cloud surface chemistry and gas-particle interactions - Part 1: General equations, parameters, and terminology. *Atmos. Chem. Phys.* **2007**, *7* (23), 5989-6023.

41. Abbatt, J. P. D.; Lee, A. K. Y.; Thornton, J. A., Quantifying trace gas uptake to tropospheric aerosol: recent advances and remaining challenges. *Chem. Soc. Rev.* **2012**, *41* (19), 6555-6581.

42. Pankow, J. F., Review and Comparative-Analysis of the Theories on Partitioning between the Gas and Aerosol Particulate Phases in the Atmosphere. *Atmos. Environ.* **1987**, *21* (11), 2275-2283.

43. Pankow, J. F., An absorption model of gas/particle partitioning of organic compounds in the atmosphere. *Atmos. Environ.* **1994**, *28* (2), 185-188.

44. Pankow, J. F., An absorption model of the gas/aerosol partitioning involved in the formation of secondary organic aerosol. *Atmos. Environ.* **1994**, *28* (2), 189-193.

45. Donahue, N. M.; Ortega, I. K.; Chuang, W.; Riipinen, I.; Riccobono, F.; Schobesberger, S.; Dommen, J.; Baltensperger, U.; Kulmala, M.; Worsnop, D. R.; Vehkamaki, H., How do organic vapors contribute to new-particle formation? *Faraday Discuss.* **2013**, *165*, 91-104.

46. Donahue, N. M.; Epstein, S. A.; Pandis, S. N.; Robinson, A. L., A two-dimensional volatility basis set: 1. organic-aerosol mixing thermodynamics. *Atmos. Chem. Phys.* **2011**, *11* (7), 3303-3318.

47. Donahue, N. M.; Robinson, A. L.; Stanier, C. O.; Pandis, S. N., Coupled partitioning, dilution, and chemical aging of semivolatile organics. *Environ. Sci. Technol.* **2006**, *40* (8), 2635-2643.

48. Vaden, T. D.; Imre, D.; Beránek, J.; Shrivastava, M.; Zelenyuk, A., Evaporation kinetics and phase of laboratory and ambient secondary organic aerosol. *Proc. Natl. Acad. Sci. U. S. A.* **2011**, *108* (6), 2190-2195.

49. Virtanen, A.; Joutsensaari, J.; Koop, T.; Kannosto, J.; Yli-Pirila, P.; Leskinen, J.; Makela, J. M.; Holopainen, J. K.; Pöschl, U.; Kulmala, M.; Worsnop, D. R.; Laaksonen, A., An amorphous solid state of biogenic secondary organic aerosol particles. *Nature* **2010**, *467* (7317), 824-827.

50. Pajunoja, A.; Malila, J.; Hao, L.; Joutsensaari, J.; Lehtinen, K. E. J.; Virtanen, A., Estimating the Viscosity Range of SOA Particles Based on Their Coalescence Time. *Aerosol. Sci. Tech.* **2014**, *48* (2), i-iv.

51. Virtanen, A.; Kannosto, J.; Kuuluvainen, H.; Arffman, A.; Joutsensaari, J.; Saukko, E.; Hao, L.; Yli-Pirila, P.; Tiitta, P.; Holopainen, J. K.; Keskinen, J.; Worsnop, D. R.; Smith, J. N.; Laaksonen, A., Bounce behavior of freshly nucleated biogenic secondary organic aerosol particles. *Atmos. Chem. Phys.* **2011**, *11* (16), 8759-8766.

52. Perraud, V.; Bruns, E. A.; Ezell, M. J.; Johnson, S. N.; Yu, Y.; Alexander, M. L.; Zelenyuk, A.; Imre, D.; Chang, W. L.; Dabdub, D.; Pankow, J. F.; Finlayson-Pitts, B. J., Nonequilibrium atmospheric secondary organic aerosol formation and growth. *Proc. Natl. Acad. Sci. U. S. A.* **2012**, *109* (8), 2836-2841.

53. Pfrang, C.; Shiraiwa, M.; Poschl, U., Chemical ageing and transformation of diffusivity in semi-solid multi-component organic aerosol particles. *Atmos Chem Phys* **2011**, *11* (14), 7343-7354.

54. Koop, T.; Bookhold, J.; Shiraiwa, M.; Pöschl, U., Glass transition and phase state of organic compounds: dependency on molecular properties and implications for secondary organic aerosols in the atmosphere. *Phys. Chem. Chem. Phys.* **2011**, *13* (43), 19238-19255.

55. Renbaum-Wolff, L.; Grayson, J. W.; Bateman, A. P.; Kuwata, M.; Sellier, M.; Murray, B. J.; Shilling, J. E.; Martin, S. T.; Bertram, A. K., Viscosity of α-pinene secondary organic material and implications for particle growth and reactivity. *Proc. Natl. Acad. Sci. U. S. A.* **2013**, *110* (20), 8014-8019.

56. Reid, J. P.; Bertram, A. K.; Topping, D. O.; Laskin, A.; Martin, S. T.; Petters, M. D.; Pope, F. D.; Rovelli, G., The viscosity of atmospherically relevant organic particles. *Nat. Commun.* **2018**, *9* (1), 956-969.

57. Cappa, C. D.; Wilson, K. R., Evolution of organic aerosol mass spectra upon heating: implications for OA phase and partitioning behavior. *Atmos. Chem. Phys.* **2011**, *11* (5), 1895-1911.

58. Ziemann, P. J., ATMOSPHERIC CHEMISTRY Phase matters for aerosols. *Nature* **2010**, *467* (7317), 797-798.

59. Marshall, F. H.; Miles, R. E. H.; Song, Y. C.; Ohm, P. B.; Power, R. M.; Reid, J. P.; Dutcher, C. S., Diffusion and reactivity in ultraviscous aerosol and the correlation with particle viscosity. *Chem. Sci.* **2016**, *7* (2), 1298-1308.

60. Shiraiwa, M.; Ammann, M.; Koop, T.; Pöschl, U., Gas uptake and chemical aging of semisolid organic aerosol particles. *Proc. Natl. Acad. Sci. U. S. A.* **2011**, *108* (27), 11003-11008.

61. Shiraiwa, M.; Seinfeld, J. H., Equilibration timescale of atmospheric secondary organic aerosol partitioning. *Geophys. Res. Letters* **2012**, *39*.

62. Zhou, S. M.; Shiraiwa, M.; McWhinney, R. D.; Pöschl, U.; Abbatt, J. P. D., Kinetic limitations in gas-particle reactions arising from slow diffusion in secondary organic aerosol. *Faraday Discuss.* **2013**, *165*, 391-406.

63. Abramson, E.; Imre, D.; Beránek, J.; Wilson, J.; Zelenyuk, A., Experimental determination of chemical diffusion within secondary organic aerosol particles. *Phys. Chem. Chem. Phys.* **2013**, *15* (8), 2983-2991.

64. Bateman, A. P.; Bertram, A. K.; Martin, S. T., Hygroscopic Influence on the Semisolid-to-Liquid Transition of Secondary Organic Materials. *J. Phys. Chem. A* **2015**, *119* (19), 4386-4395.

65. Saukko, E.; Lambe, A. T.; Massoli, P.; Koop, T.; Wright, J. P.; Croasdale, D. R.; Pedernera, D. A.; Onasch, T. B.; Laaksonen, A.; Davidovits, P.; Worsnop, D. R.; Virtanen, A., Humidity-dependent phase state of SOA particles from biogenic and anthropogenic precursors. *Atmos. Chem. Phys.* **2012**, *12* (16), 7517-7529.

66. Kuwata, M.; Martin, S. T., Phase of atmospheric secondary organic material affects its reactivity. *Proc. Natl. Acad. Sci. U. S. A.* **2012**, *109* (43), 17354-17359.

67. Bell, D. M.; Imre, D.; T. Martin, S.; Zelenyuk, A., The properties and behavior of α-pinene secondary organic aerosol particles exposed to ammonia under dry conditions. *Phys. Chem. Chem. Phys.* **2017**, *19* (9), 6497-6507.

68. Yli-Juuti, T.; Pajunoja, A.; Tikkanen, O.-P.; Buchholz, A.; Faiola, C.; Väisänen, O.; Hao, L.; Kari, E.; Peräkylä, O.; Garmash, O.; Shiraiwa, M.; Ehn, M.; Lehtinen, K.; Virtanen, A., Factors controlling the evaporation of secondary organic aerosol from α-pinene ozonolysis. *Geophys. Res. Letters* **2017**, *44* (5), 2562-2570.

69. Li, Y. J.; Liu, P.; Gong, Z.; Wang, Y.; Bateman, A. P.; Bergoend, C.; Bertram, A. K.; Martin, S. T., Chemical reactivity and liquid/nonliquid states of secondary organic material. *Environ. Sci. Technol.* **2015**, *49* (22), 13264-13274.

70. Kidd, C.; Perraud, V.; Wingen, L. M.; Finlayson-Pitts, B. J., Integrating phase and composition of secondary organic aerosol from the ozonolysis of alpha-pinene. *Proc. Natl. Acad. Sci. U. S. A.* **2014**, *111* (21), 7552-7557.

71. Shiraiwa, M.; Li, Y.; Tsimpidi, A. P.; Karydis, V. A.; Berkemeier, T.; Pandis, S. N.; Lelieveld, J.; Koop, T.; Pöschl, U., Global distribution of particle phase state in atmospheric secondary organic aerosols. *Nat. Commun.* **2017**, *8*, 15002, DOI: 10.1038/ncomms15002.

72. Zaveri, R. A.; Shilling, J. E.; Zelenyuk, A.; Liu, J.; Bell, D. M.; D'Ambro, E. L.; Gaston, C. J.; Thornton, J. A.; Laskin, A.; Lin, P.; Wilson, J.; Easter, R. C.; Wang, J.; Bertram, A. K.; Martin, S. T.; Seinfeld, J. H.; Worsnop, D. R., Growth kinetics and size distribution dynamics of viscous secondary organic aerosol. *Environ. Sci. Technol.* **2018**, *52* (3), 1191-1199.

73. Riipinen, I.; Pierce, J. R.; Yli-Juuti, T.; Nieminen, T.; Häkkinen, S.; Ehn, M.; Junninen, H.; Lehtipalo, K.; Petäjä, T.; Slowik, J.; Chang, R.; Shantz, N. C.; Abbatt, J.; Leaitch, W. R.; Kerminen, V. M.; Worsnop, D. R.; Pandis, S. N.; Donahue, N. M.; Kulmala, M., Organic condensation: a vital link connecting aerosol formation to cloud condensation nuclei (CCN) concentrations. *Atmos. Chem. Phys.* **2011**, *11* (8), 3865-3878.

74. Wang, C.; Wania, F.; Goss, K.-U., Is secondary organic aerosol yield governed by kinetic factors rather than equilibrium partitioning? *Environ. Sci. Proc. Imp.* **2018**, *20* (1), 245-252.

75. Denjean, C.; Formenti, P.; Picquet-Varrault, B.; Pangui, E.; Zapf, P.; Katrib, Y.; Giorio, C.; Tapparo, A.; Monod, A.; Temime-Roussel, B.; Decorse, P.; Mangeney, C.; Doussin, J. F., Relating hygroscopicity and optical properties to chemical composition and structure of secondary organic aerosol particles generated from the ozonolysis of α-pinene. *Atmos. Chem. Phys.* **2015**, *15* (6), 3339-3358.

76. McIntire, T. M.; Ryder, O. S.; Gassman, P. L.; Zhu, Z.; Ghosal, S.; Finlayson-Pitts, B. J., Why ozonolysis may not increase the hydrophilicity of particles. *Atmos. Environ.* **2010**, *44* (7), 939-944.

77. Upshur, M. A.; Vega, M. M.; Bé, A. G.; Chase, H. M.; Zhang, Y.; Tuladhar, A.; Chase, Z. A.; Fu, L.; Ebben, C. J.; Wang, Z.; Martin, S. T.; Geiger, F. M.; Thomson, R. J., Synthesis and surface spectroscopy of α-pinene isotopologues and their corresponding secondary organic material. *Chem. Sci.* **2019**, *10* (36), 8390-8398.

78. Shrestha, M.; Zhang, Y.; Upshur, M. A.; Liu, P.; Blair, S. L.; Wang, H.-f.; Nizkorodov, S. A.; Thomson, R. J.; Martin, S. T.; Geiger, F. M., On Surface Order and Disorder of α-Pinene-Derived Secondary Organic Material. *J. Phys. Chem. A* **2015**, *119* (19), 4609-4617.

79. Pfrang, C.; Shiraiwa, M.; Pöschl, U., Chemical ageing and transformation of diffusivity in semi-solid multi-component organic aerosol particles. *Atmos. Chem. Phys.* **2011**, *11* (14), 7343-7354.

80. Boyd, C. M.; Nah, T.; Xu, L.; Berkemeier, T.; Ng, N. L., Secondary organic aerosol (SOA) from nitrate radical oxidation of monoterpenes: effects of temperature, dilution, and humidity on aerosol formation, mixing, and evaporation. *Environ. Sci. Technol.* **2017**, *51* (14), 7831-7841.

81. Zelenyuk, A.; Imre, D.; Beránek, J.; Abramson, E.; Wilson, J.; Shrivastava, M., Synergy between Secondary Organic Aerosols and Long-Range Transport of Polycyclic Aromatic Hydrocarbons. *Environ. Sci. Technol.* **2012**, *46* (22), 12459-12466.

82. Skalska, K.; Miller, J. S.; Ledakowicz, S., Trends in NOx abatement: A review. *Sci. Total Environ.* **2010**, *408* (19), 3976-3989.

83. Pacyna, J. M.; Larssen, S.; Semb, A., European survey for NOx emissions with emphasis on Eastern Europe. *Atmos. Environ. A, Gen. Top.* **1991**, *25* (2), 425-439.

84. Ng, N. L.; Brown, S. S.; Archibald, A. T.; Atlas, E.; Cohen, R. C.; Crowley, J. N.; Day, D. A.; Donahue, N. M.; Fry, J. L.; Fuchs, H.; Griffin, R. J.; Guzman, M. I.; Herrmann, H.; Hodzic, A.; Iinuma, Y.; Jimenez, J. L.; Kiendler-Scharr, A.; Lee, B. H.; Luecken, D. J.; Mao, J.; McLaren, R.; Mutzel, A.; Osthoff, H. D.; Ouyang, B.; Picquet-Varrault, B.; Platt, U.; Pye, H. O. T.; Rudich, Y.; Schwantes, R. H.; Shiraiwa, M.; Stutz, J.; Thornton, J. A.; Tilgner, A.; Williams, B. J.; Zaveri, R. A., Nitrate radicals and biogenic volatile organic compounds: oxidation, mechanisms, and organic aerosol. *Atmos. Chem. Phys.* **2017**, *17* (3), 2103-2162.

85. Brown, S. S.; Stutz, J., Nighttime radical observations and chemistry. *Chem. Soc. Rev.* **2012**, *41* (19), 6405-6447.

86. Wayne, R. P.; Barnes, I.; Biggs, P.; Burrows, J. P.; Canosa-Mas, C. E.; Hjorth, J.; Le Bras, G.; Moortgat, G. K.; Perner, D.; Poulet, G.; Restelli, G.; Sidebottom, H., The nitrate radical: Physics, chemistry, and the atmosphere. *Atmos. Environ. A, Gen. Top.* **1991**, *25* (1), 1-203.

87. Roberts, J. M., The atmospheric chemistry of organic nitrates. *Atmos. Environ. A, Gen. Top.* **1990**, *24* (2), 243-287.

88. Sobanski, N.; Thieser, J.; Schuladen, J.; Sauvage, C.; Song, W.; Williams, J.; Lelieveld, J.; Crowley, J. N., Day and night-time formation of organic nitrates at a forested mountain site in south-west Germany. *Atmos. Chem. Phys.* **2017**, *17* (6), 4115-4130.

89. Fry, J. L.; Kiendler-Scharr, A.; Rollins, A. W.; Brauers, T.; Brown, S. S.; Dorn, H. P.; Dubé, W. P.; Fuchs, H.; Mensah, A.; Rohrer, F.; Tillmann, R.; Wahner, A.; Wooldridge, P. J.; Cohen, R. C., SOA from limonene: role of NO_3 in its generation and degradation. *Atmos. Chem. Phys.* **2011**, *11* (8), 3879-3894.

90. Fry, J. L.; Draper, D. C.; Barsanti, K. C.; Smith, J. N.; Ortega, J.; Winkler, P. M.; Lawler, M. J.; Brown, S. S.; Edwards, P. M.; Cohen, R. C.; Lee, L., Secondary organic aerosol formation and organic nitrate yield from NO_3 oxidation of biogenic hydrocarbons. *Environ. Sci. Technol.* **2014**, *48* (20), 11944-11953.

91. Slade, J. H.; de Perre, C.; Lee, L.; Shepson, P. B., Nitrate radical oxidation of γ-terpinene: hydroxy nitrate, total organic nitrate, and secondary organic aerosol yields. *Atmos. Chem. Phys.* **2017**, *17* (14), 8635-8650.

92. Spittler, M.; Barnes, I.; Bejan, I.; Brockmann, K.; Benter, T.; Wirtz, K., Reactions of NO_3 radicals with limonene and α-pinene: product and SOA formation. *Atmos. Environ.* **2006**, *40*, 116-127.

93. Atkinson, R.; Aschmann, S. M.; Carter, W. P.; Winer, A. M.; Pitts Jr, J. N., Alkyl nitrate formation from the nitrogen oxide (NO_x)-air photooxidations of C_2-C_8 n-alkanes. *J. Phys. Chem.* **1982**, *86* (23), 4563-4569.

94. Berkemeier, T.; Ammann, M.; Mentel, T. F.; Pöschl, U.; Shiraiwa, M., Organic Nitrate Contribution to New Particle Formation and Growth in Secondary Organic Aerosols from α-Pinene Ozonolysis. *Environ. Sci. Technol.* **2016**, *50* (12), 6334-6342.

95. Renbaum, L. H.; Smith, G. D., Organic nitrate formation in the radical-initiated oxidation of model aerosol particles in the presence of NOx. *Phys. Chem. Chem. Phys.* **2009**, *11* (36), 8040-8047.

96. Lim, Y. B.; Ziemann, P. J., Products and Mechanism of Secondary Organic Aerosol Formation from Reactions of n-Alkanes with OH Radicals in the Presence of NOx. *Environ. Sci. Technol.* **2005**, *39* (23), 9229-9236.

97. Perring, A. E.; Pusede, S. E.; Cohen, R. C., An observational perspective on the atmospheric impacts of alkyl and multifunctional nitrates on ozone and secondary organic aerosol. *Chem. Rev.* **2013**, *113* (8), 5848-5870.

98. O'Brien, J. M.; Shepson, P. B.; Muthuramu, K.; Hao, C.; Niki, H.; Hastie, D. R.; Taylor, R.; Roussel, P. B., Measurements of alkyl and multifunctional organic nitrates at a rural site in Ontario. *J. Geophys. Res. Atmos.* **1995**, *100* (D11), 22795-22804.

99. Fischer, R. G.; Kastler, J.; Ballschmiter, K., Levels and pattern of alkyl nitrates, multifunctional alkyl nitrates, and halocarbons in the air over the Atlantic Ocean. *J. Geophys. Res. Atmos.* **2000**, *105* (D11), 14473-14494.

100. Kastler, J.; Ballschmiter, K., Bifunctional alkyl nitrates – trace constituents of the atmosphere. *Fresenius J. Anal. Chem.* **1998**, *360* (7), 812-816.

101. O'Brien, J. M.; Shepson, P. B.; Wu, Q.; Biesenthal, T.; Bottenheim, J. W.; Wiebe, H. A.; Anlauf, K. G.; Brickell, P., Production and distribution of organic nitrates, and their relationship to carbonyl compounds in an urban environment. *Atmos. Environ.* **1997**, *31* (14), 2059-2069.

102. Kastler, J.; Jarman, W.; Ballschmiter, K., Multifunctional organic nitrates as constituents in European and US urban photo-smog. *Fresenius J. Anal. Chem.* **2000**, *368* (2), 244-249.

103. Fry, J. L.; Draper, D. C.; Zarzana, K. J.; Campuzano-Jost, P.; Day, D. A.; Jimenez, J. L.; Brown, S. S.; Cohen, R. C.; Kaser, L.; Hansel, A.; Cappellin, L.; Karl, T.; Hodzic Roux, A.; Turnipseed, A.; Cantrell, C.; Lefer, B. L.; Grossberg, N., Observations of gas- and aerosol-phase organic nitrates at BEACHON-RoMBAS 2011. *Atmos. Chem. Phys.* **2013**, *13* (17), 8585-8605.

104. Rollins, A. W.; Pusede, S.; Wooldridge, P.; Min, K. E.; Gentner, D. R.; Goldstein, A. H.; Liu, S.; Day, D. A.; Russell, L. M.; Rubitschun, C. L.; Surratt, J. D.; Cohen, R. C., Gas/particle partitioning of total alkyl nitrates observed with TD-LIF in Bakersfield. *J. Geophys. Res. Atmos.* **2013**, *118* (12), 6651-6662.

105. Lee, B. H.; Mohr, C.; Lopez-Hilfiker, F. D.; Lutz, A.; Hallquist, M.; Lee, L.; Romer, P.; Cohen, R. C.; Iyer, S.; Kurten, T.; Hu, W. W.; Day, D. A.; Campuzano-Jost, P.; Jimenez, J. L.; Xu, L.; Ng, N. L.; Guo, H. Y.; Weber, R. J.; Wild, R. J.; Brown, S. S.; Koss, A.; de Gouw, J.; Olson, K.; Goldstein, A. H.; Seco, R.; Kim, S.; McAvey, K.; Shepson, P. B.; Starn, T.; Baumann, K.; Edgerton, E. S.; Liu, J. M.; Shilling, J. E.; Miller, D. O.; Brune, W.; Schobesberger, S.; D'Ambro, E. L.; Thornton, J. A., Highly functionalized organic nitrates in the southeast United States: contribution to secondary organic aerosol and reactive nitrogen budgets. *Proc. Natl. Acad. Sci. U. S. A.* **2016**, *113* (6), 1516-1521.

106. Allen, D. T.; Palen, E. J.; Haimov, M. I.; Hering, S. V.; Young, J. R., Fourier Transform Infrared Spectroscopy of Aerosol Collected in a Low Pressure Impactor (LPI/FTIR): Method Development and Field Calibration. *Aerosol. Sci. Tech.* **1994**, *21* (4), 325-342.

107. Huang, W.; Saathoff, H.; Shen, X.; Ramisetty, R.; Leisner, T.; Mohr, C., Chemical Characterization of Highly Functionalized Organonitrates Contributing to Night-Time Organic Aerosol Mass Loadings and Particle Growth. *Environ. Sci. Technol.* **2019**, *53* (3), 1165-1174.

108. Lee, A. K. Y.; Adam, M. G.; Liggio, J.; Li, S. M.; Li, K.; Willis, M. D.; Abbatt, J. P. D.; Tokarek, T. W.; Odame-Ankrah, C. A.; Osthoff, H. D.; Strawbridge, K.; Brook, J. R., A Large Contribution of Anthropogenic Organo-Nitrates to Secondary Organic Aerosol in the Alberta Oil Sands. *Atmos. Chem. Phys. Discuss.* **2019**, *2019*, 1-25.

109. Drewnick, F.; Schneider, J.; Hings, S. S.; Hock, N.; Noone, K.; Targino, A.; Weimer, S.; Borrmann, S., Measurement of Ambient, Interstitial, and Residual Aerosol Particles on a

Mountaintop Site in Central Sweden using an Aerosol Mass Spectrometer and a CVI. *J. Atmos. Chem.* **2007**, *56* (1), 1-20.

110. Lee, A. K. Y.; Adam, M. G.; Liggio, J.; Li, S. M.; Li, K.; Willis, M. D.; Abbatt, J. P. D.; Tokarek, T. W.; Odame-Ankrah, C. A.; Osthoff, H. D.; Strawbridge, K.; Brook, J. R., A large contribution of anthropogenic organo-nitrates to secondary organic aerosol in the Alberta oil sands. *Atmos. Chem. Phys.* **2019**, *19* (19), 12209-12219.

111. Xu, L.; Suresh, S.; Guo, H.; Weber, R. J.; Ng, N. L., Aerosol characterization over the southeastern United States using high-resolution aerosol mass spectrometry: spatial and seasonal variation of aerosol composition and sources with a focus on organic nitrates. *Atmos. Chem. Phys.* **2015**, *15* (13), 7307-7336.

112. Rollins, A. W.; Browne, E. C.; Min, K. E.; Pusede, S. E.; Wooldridge, P. J.; Gentner, D. R.; Goldstein, A. H.; Liu, S.; Day, D. A.; Russell, L. M.; Cohen, R. C., Evidence for NO_x Control over Nighttime SOA Formation. *Science* **2012**, *337* (6099), 1210.

113. Day, D. A.; Liu, S.; Russell, L. M.; Ziemann, P. J., Organonitrate group concentrations in submicron particles with high nitrate and organic fractions in coastal southern California. *Atmos. Environ.* **2010**, *44* (16), 1970-1979.

114. Zare, A.; Romer, P. S.; Nguyen, T.; Keutsch, F. N.; Skog, K.; Cohen, R. C., A comprehensive organic nitrate chemistry: insights into the lifetime of atmospheric organic nitrates. *Atmos. Chem. Phys.* **2018**, *18* (20), 15419-15436.

115. Lee, A. K. Y.; Abbatt, J. P. D.; Leaitch, W. R.; Li, S. M.; Sjostedt, S. J.; Wentzell, J. J. B.; Liggio, J.; Macdonald, A. M., Substantial secondary organic aerosol formation in a coniferous forest: observations of both day- and nighttime chemistry. *Atmos. Chem. Phys.* **2016**, *16* (11), 6721-6733.

116. Xu, L.; Guo, H.; Boyd, C. M.; Klein, M.; Bougiatioti, A.; Cerully, K. M.; Hite, J. R.; Isaacman-VanWertz, G.; Kreisberg, N. M.; Knote, C.; Olson, K.; Koss, A.; Goldstein, A. H.; Hering, S. V.; de Gouw, J.; Baumann, K.; Lee, S.-H.; Nenes, A.; Weber, R. J.; Ng, N. L., Effects of anthropogenic emissions on aerosol formation from isoprene and monoterpenes in the southeastern United States. *Proc. Natl. Acad. Sci. U. S. A.* **2015**, *112* (1), 37.

117. Ayres, B. R.; Allen, H. M.; Draper, D. C.; Brown, S. S.; Wild, R. J.; Jimenez, J. L.; Day, D. A.; Campuzano-Jost, P.; Hu, W.; de Gouw, J.; Koss, A.; Cohen, R. C.; Duffey, K. C.; Romer, P.; Baumann, K.; Edgerton, E.; Takahama, S.; Thornton, J. A.; Lee, B. H.; Lopez-Hilfiker, F. D.; Mohr, C.; Wennberg, P. O.; Nguyen, T. B.; Teng, A.; Goldstein, A. H.; Olson, K.; Fry, J. L., Organic nitrate aerosol formation via NO₃ + biogenic volatile organic compounds in the southeastern United States. *Atmos. Chem. Phys.* **2015**, *15* (23), 13377-13392.

118. Stockwell, C. E.; Veres, P. R.; Williams, J.; Yokelson, R. J., Characterization of biomass burning emissions from cooking fires, peat, crop residue, and other fuels with high-resolution proton-transfer-reaction time-of-flight mass spectrometry. *Atmos. Chem. Phys.* **2015**, *15* (2), 845-865.

119. Coggon, M. M.; Veres, P. R.; Yuan, B.; Koss, A.; Warneke, C.; Gilman, J. B.; Lerner, B. M.; Peischl, J.; Aikin, K. C.; Stockwell, C. E.; Hatch, L. E.; Ryerson, T. B.; Roberts, J. M.; Yokelson, R. J.; de Gouw, J. A., Emissions of nitrogen-containing organic compounds from the burning of herbaceous and arboraceous biomass: Fuel composition dependence and the variability of commonly used nitrile tracers. *Geophys. Res. Letters* **2016**, *43* (18), 9903-9912.

120. Booyens, W.; Van Zyl, P. G.; Beukes, J. P.; Ruiz-Jimenez, J.; Kopperi, M.; Riekkola, M.-L.; Vakkari, V.; Josipovic, M.; Kulmala, M.; Laakso, L., Characterising Particulate Organic Nitrogen at A Savannah-Grassland Region in South Africa. *Atmosphere* **2019**, *10* (9), 492.

121. Cape, J. N.; Cornell, S. E.; Jickells, T. D.; Nemitz, E., Organic nitrogen in the atmosphere — Where does it come from? A review of sources and methods. *Atmos. Res.* **2011**, *102* (1), 30-48.

122. Simoneit, B. R. T.; Rushdi, A. I.; bin Abas, M. R.; Didyk, B. M., Alkyl Amides and Nitriles as Novel Tracers for Biomass Burning. *Environ. Sci. Technol.* **2003**, *37* (1), 16-21.

123. Cavdar, H.; Saracoglu, N., Synthesis of new β-hydroxy nitrate esters as potential glycomimetics or vasodilators. *Eur. J. Org. Chem.* **2008**, *2008* (27), 4615-4621.

124. Holger, B.; Friedrich, S.; Wolfram, S., Thermal decomposition of 2-ethylhexyl nitrate (2-EHN). *Int. J. Chem. Kinet.* **2002**, *34* (1), 34-38.

125. Day, D. A.; Wooldridge, P. J.; Dillon, M. B.; Thornton, J. A.; Cohen, R. C., A thermal dissociation laser-induced fluorescence instrument for in situ detection of NO_2, peroxy nitrates, alkyl nitrates, and HNO_3. *J. Geophys. Res. Atmos.* **2002**, *107* (D6), DOI: 10.1029/2001jd000779.

126. Pankow, J. F.; Asher, W. E., SIMPOL.1: a simple group contribution method for predicting vapor pressures and enthalpies of vaporization of multifunctional organic compounds. *Atmos. Chem. Phys.* **2008**, *8* (10), 2773-2796.

127. Moller, B.; Rarey, J.; Ramjugernath, D., Estimation of the vapour pressure of non-electrolyte organic compounds via group contributions and group interactions. *J. Mol. Liq.* **2008**, *143* (1), 52-63.

128. Nannoolal, Y.; Rarey, J.; Ramjugernath, D.; Cordes, W., Estimation of pure component properties: Part 1. Estimation of the normal boiling point of non-electrolyte organic compounds via group contributions and group interactions. *Fluid Phase Equil.* **2004**, *226*, 45-63.

129. Sulbaek Andersen, M. P.; Kyte, M.; Andersen, S. T.; Nielsen, C. J.; Nielsen, O. J., Atmospheric Chemistry of (CF3)2CF–C≡N: A Replacement Compound for the Most Potent Industrial Greenhouse Gas, SF6. *Environ. Sci. Technol.* **2017**, *51* (3), 1321-1329.

130. Blázquez, S.; Antiñolo, M.; Nielsen, O. J.; Albaladejo, J.; Jiménez, E., Reaction kinetics of (CF3)2CFCN with OH radicals as a function of temperature (278–358K): A good replacement for greenhouse SF6? *Chem. Phys. Lett.* **2017**, *687*, 297-302.

131. Atkinson, R., Gas-Phase Tropospheric Chemistry of Volatile Organic Compounds: 1. Alkanes and Alkenes. *J. Phys. Chem. Ref. Data* **1997**, *26* (2), 215-290.

132. Li, J. P. H.; Stockenhuber, M., A temperature programmed desorption study of the interaction of ethyl cyanoacetate and benzaldehyde on metal oxide surfaces. *Catal. Today* **2015**, *245*, 108-115.

133. Chorbadjiev, K. G.; Novakov, P. C., Study on the molecular weights of oligomers of α-cyanoacrylates formed by reaction of alkyl cyanoacetates with formaldehyde. *Eur. Polym. J.* **1991**, *27* (4), 439-443.

134. B. Demore, W., Rates and mechanism of alkyne ozonation. *Int. J. Chem. Kinet.* **1971**, *3* (2), 161-173.

135. Kwok, E. S. C.; Atkinson, R., Estimation of hydroxyl radical reaction rate constants for gas-phase organic compounds using a structure-reactivity relationship: An update. *Atmos. Environ.* **1995**, *29* (14), 1685-1695.

136. Atkinson, R.; Arey, J., Atmospheric Degradation of Volatile Organic Compounds. *Chem. Rev.* **2003**, *103* (12), 4605-4638.

137. Ianni, J. C. Kintecus. www.kintecus.com.

138. Zelenyuk, A.; Yang, J.; Song, C.; Zaveri, R. A.; Imre, D., A new real-time method for determining particles' sphericity and density: application to secondary organic aerosol formed by ozonolysis of α-pinene. *Environ. Sci. Technol.* **2008**, *42* (21), 8033-8038.

139. Ezell, M. J.; Johnson, S. N.; Yu, Y.; Perraud, V.; Bruns, E. A.; Alexander, M. L.; Zelenyuk, A.; Dabdub, D.; Finlayson-Pitts, B. J., A new aerosol flow system for photochemical and thermal studies of tropospheric aerosols. *Aerosol. Sci. Tech.* **2010**, *44* (5), 329-338.

140. Zhang, Q.; Worsnop, D. R.; Canagaratna, M. R.; Jimenez, J. L., Hydrocarbon-like and oxygenated organic aerosols in Pittsburgh: insights into sources and processes of organic aerosols. *Atmos. Chem. Phys.* **2005**, *5* (12), 3289-3311.

141. Zhang, X.; Mcvay, R. C.; Huang, D. D.; Dalleska, N. F.; Aumont, B.; Flagan, R. C.; Seinfeld, J. H., Formation and evolution of molecular products in alpha-pinene secondary organic aerosol. *Proc. Natl. Acad. Sci. U. S. A.* **2015**, *112* (46), 14168-14173.

142. Winterhalter, R.; Van Dingenen, R.; Larsen, B. R.; Jensen, N. R.; Hjorth, J., LC-MS analysis of aerosol particles from the oxidation of α-pinene by ozone and OH-radicals. *Atmos. Chem. Phys. Discuss.* **2003**, *2003*, 1-39.

143. Witkowski, B.; Gierczak, T., Early stage composition of SOA produced by α-pinene/ozone reaction: α-acyloxyhydroperoxy aldehydes and acidic dimers. *Atmos. Environ.* **2014**, *95*, 59-70.

144. Kristensen, K.; Cui, T.; Zhang, H.; Gold, A.; Glasius, M.; Surratt, J. D., Dimers in α-pinene secondary organic aerosol: effect of hydroxyl radical, ozone, relative humidity and aerosol acidity. *Atmos. Chem. Phys.* **2014**, *14* (8), 4201-4218.

145. Kristensen, K.; Watne, Å. K.; Hammes, J.; Lutz, A.; Petäjä, T.; Hallquist, M.; Bilde, M.; Glasius, M., High-molecular weight dimer esters are major products in aerosols from α-pinene ozonolysis and the boreal forest. *Environ. Sci. Technol. Letters* **2016**, *3* (8), 280-285.

146. Docherty, K. S.; Wu, W.; Lim, Y. B.; Ziemann, P. J., Contributions of organic peroxides to secondary aerosol formed from reactions of monoterpenes with O_3. *Environ. Sci. Technol.* **2005**, *39* (11), 4049-4059.

147. Harrick, N. J., *Internal Reflection Spectroscopy*. Interscience Publishers: **1967**.

148. Kim, H.; Barkey, B.; Paulson, S. E., Real refractive indices of α- and β-pinene and toluene secondary organic aerosols generated from ozonolysis and photo-oxidation. *J. Geophys. Res. Atmos.* **2010**, *115* (D24), DOI: 10.1029/2010jd014549.

149. Jayne, J. T.; Leard, D. C.; Zhang, X. F.; Davidovits, P.; Smith, K. A.; Kolb, C. E.; Worsnop, D. R., Development of an aerosol mass spectrometer for size and composition analysis of submicron particles. *Aerosol. Sci. Tech.* **2000**, *33* (1-2), 49-70.

150. DeCarlo, P. F.; Kimmel, J. R.; Trimborn, A.; Northway, M. J.; Jayne, J. T.; Aiken, A. C.; Gonin, M.; Fuhrer, K.; Horvath, T.; Docherty, K. S.; Worsnop, D. R.; Jimenez, J. L., Field-deployable, high-resolution, time-of-flight aerosol mass spectrometer. *Anal. Chem.* **2006**, *78* (24), 8281-8289.

151. Canagaratna, M. R.; Jayne, J. T.; Jimenez, J. L.; Allan, J. D.; Alfarra, M. R.; Zhang, Q.; Onasch, T. B.; Drewnick, F.; Coe, H.; Middlebrook, A.; Delia, A.; Williams, L. R.; Trimborn, A. M.; Northway, M. J.; DeCarlo, P. F.; Kolb, C. E.; Davidovits, P.; Worsnop, D. R., Chemical and microphysical characterization of ambient aerosols with the aerodyne aerosol mass spectrometer. *Mass Spectrom. Rev.* **2007**, *26* (2), 185-222.

152. Canagaratna, M. R.; Jimenez, J. L.; Kroll, J. H.; Chen, Q.; Kessler, S. H.; Massoli, P.; Hildebrandt Ruiz, L.; Fortner, E.; Williams, L. R.; Wilson, K. R.; Surratt, J. D.; Donahue, N. M.; Jayne, J. T.; Worsnop, D. R., Elemental ratio measurements of organic compounds using aerosol mass spectrometry: characterization, improved calibration, and implications. *Atmos. Chem. Phys.* **2015**, *15* (1), 253-272.

153. Fraser, R. T. M.; Paul, N. C., The mass spectrometry of nitrate esters and related compounds. Part II. *J. Chem. Soc. B* **1968**, *140* (12), 1407-1410.

154. Bruns, E. A.; Perraud, V.; Zelenyuk, A.; Ezell, M. J.; Johnson, S. N.; Yu, Y.; Imre, D.; Finlayson-Pitts, B. J.; Alexander, M. L., Comparison of FTIR and particle mass spectrometry for the measurement of particulate organic nitrates. *Environ. Sci. Technol.* **2010**, *44* (3), 1056-1061.

155. Rollins, A. W.; Fry, J. L.; Hunter, J. F.; Kroll, J. H.; Worsnop, D. R.; Singaram, S. W.; Cohen, R. C., Elemental analysis of aerosol organic nitrates with electron ionization high-resolution mass spectrometry. *Atmos. Meas. Tech.* **2010**, *3* (1), 301-310.

156. Farmer, D. K.; Matsunaga, A.; Docherty, K. S.; Surratt, J. D.; Seinfeld, J. H.; Ziemann, P. J.; Jimenez, J. L., Response of an aerosol mass spectrometer to organonitrates and organosulfates and implications for atmospheric chemistry. *Proc. Natl. Acad. Sci. U. S. A.* **2010**, *107* (15), 6670-6675.

157. Fraser, R. T. M.; Paul, N. C., The mass spectrometry of nitrate esters and related compounds. Part I. *J. Chem. Soc. B* **1968**, *6*, 659-663.

158. Fry, J. L.; Kiendler-Scharr, A.; Rollins, A. W.; Brauers, T.; Brown, S. S.; Dorn, H. P.; Dube, W. P.; Fuchs, H.; Mensah, A.; Rohrer, F.; Tillmann, R.; Wahner, A.; Wooldridge, P. J.; Cohen, R. C., SOA from limonene: role of NO3 in its generation and degradation. *Atmos. Chem. Phys.* **2011**, *11* (8), 3879-3894.

159. Farmer, D. K.; Matsunaga, A.; Docherty, K. S.; Surratt, J. D.; Seinfeld, J. H.; Ziemann, P. J.; Jimenez, J. L., Response of an aerosol mass spectrometer to organonitrates and organosulfates and implications for atmospheric chemistry. *Proc. Natl. Acad. Sci. U.S.A.* **2010**, *107* (15), 6670-6675.

160. O'Connor, C. S. S.; Jones, N. C.; Price, S. D., Electron-impact ionization of nitric acid. *Int. J. Mass Spectrom. Ion Process.* **1997**, *163* (1), 131-139.

161. Friedel, R. A.; Shultz, J. L.; Sharkey, A. G., Mass Spectrum of Nitric Acid. *Anal. Chem.* **1959**, *31* (6), 1128-1128.

162. Liu, P. S. K.; Deng, R.; Smith, K. A.; Williams, L. R.; Jayne, J. T.; Canagaratna, M. R.; Moore, K.; Onasch, T. B.; Worsnop, D. R.; Deshler, T., Transmission Efficiency of an Aerodynamic Focusing Lens System: Comparison of Model Calculations and Laboratory Measurements for the Aerodyne Aerosol Mass Spectrometer. *Aerosol. Sci. Tech.* **2007**, *41* (8), 721-733.

163. Jenkin, M. E.; Saunders, S. M.; Pilling, M. J., The tropospheric degradation of volatile organic compounds: a protocol for mechanism development. *Atmos. Environ.* **1997**, *31* (1), 81-104.

164. Saunders, S. M.; Jenkin, M. E.; Derwent, R. G.; Pilling, M. J., Protocol for the development of the Master Chemical Mechanism, MCM v3 (Part A): tropospheric degradation of non-aromatic volatile organic compounds. *Atmos. Chem. Phys.* **2003**, *3* (1), 161-180.

165. Jenkin, M. E.; Young, J. C.; Rickard, A. R., The MCM v3.3.1 degradation scheme for isoprene. *Atmos. Chem. Phys.* **2015**, *15* (20), 11433-11459.

166. Sommariva, R.; Cox, S.; Martin, C.; Borońska, K.; Young, J.; Jimack, P. K.; Pilling, M. J.; Matthaios, V. N.; Nelson, B. S.; Newland, M. J.; Panagi, M.; Bloss, W. J.; Monks, P. S.;

Rickard, A. R., AtChem (version 1), an open-source box model for the Master Chemical Mechanism. *Geosci. Model Dev.* **2020**, *13* (1), 169-183.

167. Zhao, Y.; Thornton, J. A.; Pye, H. O. T., Quantitative constraints on autoxidation and dimer formation from direct probing of monoterpene-derived peroxy radical chemistry. *Proc. Natl. Acad. Sci. U. S. A.* **2018**, *115* (48), 12142-12147.

168. Atkinson, R.; Aschmann, S. M.; Arey, J.; Shorees, B., Formation of OH radicals in the gas phase reactions of O3 with a series of terpenes. *J. Geophys. Res. Atmos.* **1992**, *97* (D5), 6065-6073.

169. Paulson, S. E.; Chung, M.; Sen, A. D.; Orzechowska, G., Measurement of OH radical formation from the reaction of ozone with several biogenic alkenes. *J. Geophys. Res. Atmos.* **1998**, *103* (D19), 25533-25539.

170. Forester, C. D.; Wells, J. R., Hydroxyl radical yields from reactions of terpene mixtures with ozone. *Indoor Air* **2011**, *21* (5), 400-409.

171. Becker, K. H.; Wirtz, K., Gas phase reactions of alkyl nitrates with hydroxyl radicals under tropospheric conditions in comparison with photolysis. *J. Atmos. Chem.* **1989**, *9* (4), 419-433.

172. Israelachvili, J., *Intermolecular & Surface Forces*. Second ed.; Academic Press: **1991**.

173. Shiraiwa, M.; Pfrang, C.; Koop, T.; Pöschl, U., Kinetic multi-layer model of gas-particle interactions in aerosols and clouds (KM-GAP): linking condensation, evaporation and chemical reactions of organics, oxidants and water. *Atmos. Chem. Phys.* **2012**, *12* (5), 2777-2794.

174. Fairhurst, M. C.; Ezell, M. J.; Finlayson-Pitts, B. J., Knudsen cell studies of the uptake of gaseous ammonia and amines onto C_3-C_7 solid dicarboxylic acids. *Phys. Chem. Chem. Phys.* **2017**, *19* (38), 26296-26309.

175. Fairhurst, M. C.; Ezell, M. J.; Kidd, C.; Lakey, P. S. J.; Shiraiwa, M.; Finlayson-Pitts, B. J., Kinetics, mechanisms and ionic liquids in the uptake of n-butylamine onto low molecular weight dicarboxylic acids. *Phys. Chem. Chem. Phys.* **2017**, *19* (6), 4827-4839.

176. Donaldson, D. J.; Mmereki, B. T.; Chaudhuri, S. R.; Handley, S.; Oh, M., Uptake and reaction of atmospheric organic vapours on organic films. *Faraday Discuss.* **2005**, *130* (0), 227-239.

177. Vander Wall, A. C.; Lakey, P. S. J.; Rossich Molina, E.; Perraud, V.; Wingen, L. M.; Xu, J.; Soulsby, D.; Gerber, R. B.; Shiraiwa, M.; Finlayson-Pitts, B. J., Understanding interactions of organic nitrates with the surface and bulk of organic films: implications for particle growth in the atmosphere. *Environ. Sci. Proc. Imp.* **2018**, *20* (11), 1593-1610.

178. Vanderhoff, P. A.; Thompson, H. W.; Lalancette, R. A., Structure of (±)-cis-pinonic acid. *Acta Cryst. C* **1986**, *42* (12), 1766-1769.

179. Ouellette, R. J.; Rawn, J. D., 1 - Structure and Bonding in Organic Compounds. In *Organic Chemistry (Second Edition)*, Ouellette, R. J.; Rawn, J. D., Eds. Academic Press: **2018**; pp 1-30.

180. Treves, K.; Shragina, L.; Rudich, Y., Measurement of octanol–air partition coefficients using solid-phase microextraction (SPME)—application to hydroxy alkyl nitrates. *Atmos. Environ.* **2001**, *35* (33), 5843-5854.

181. Shepson, P. B.; Mackay, E.; Muthuramu, K., Henry's Law Constants and Removal Processes for Several Atmospheric β-Hydroxy Alkyl Nitrates. *Environ. Sci. Technol.* **1996**, *30* (12), 3618-3623.

182. Kames, J.; Schurath, U., Alkyl nitrates and bifunctional nitrates of atmospheric interest: Henry's law constants and their temperature dependencies. *J. Atmos. Chem.* **1992**, *15* (1), 79-95.

183. Kroll, J. H.; Donahue, N. M.; Jimenez, J. L.; Kessler, S. H.; Canagaratna, M. R.; Wilson, K. R.; Altieri, K. E.; Mazzoleni, L. R.; Wozniak, A. S.; Bluhm, H.; Mysak, E. R.; Smith, J. D.; Kolb, C. E.; Worsnop, D. R., Carbon oxidation state as a metric for describing the chemistry of atmospheric organic aerosol. *Nat. Chem.* **2011**, *3*, 133-139.

184. Putman, A. L.; Offenberg, J. H.; Fisseha, R.; Kundu, S.; Rahn, T. A.; Mazzoleni, L. R., Ultrahigh-resolution FT-ICR mass spectrometry characterization of α-pinene ozonolysis SOA. *Atmos. Environ.* **2012**, *46*, 164-172.

185. Laskin, A.; Gilles, M. K.; Knopf, D. A.; Wang, B.; China, S., Progress in the Analysis of Complex Atmospheric Particles. *Annu. Rev. Anal. Chem.* **2016**, *9* (1), 117-143.

186. Nozière, B.; Kalberer, M.; Claeys, M.; Allan, J.; D'Anna, B.; Decesari, S.; Finessi, E.; Glasius, M.; Grgić, I.; Hamilton, J. F.; Hoffmann, T.; Iinuma, Y.; Jaoui, M.; Kahnt, A.; Kampf, C. J.; Kourtchev, I.; Maenhaut, W.; Marsden, N.; Saarikoski, S.; Schnelle-Kreis, J.; Surratt, J. D.; Szidat, S.; Szmigielski, R.; Wisthaler, A., The Molecular Identification of Organic Compounds in the Atmosphere: State of the Art and Challenges. *Chem. Rev.* **2015**, *115* (10), 3919-3983.

187. Chew, A. A.; Atkinson, R., OH radical formation yields from the gas-phase reactions of O_3 with alkenes and monoterpenes. *J. Geophys. Res. Atmos.* **1996**, *101* (D22), 28649-28653.

188. Alam, M. S.; Camredon, M.; Rickard, A. R.; Carr, T.; Wyche, K. P.; Hornsby, K. E.; Monks, P. S.; Bloss, W. J., Total radical yields from tropospheric ethene ozonolysis. *Phys. Chem. Chem. Phys.* **2011**, *13* (23), 11002-11015.

189. Aschmann, S. M.; Chew, A. A.; Arey, J.; Atkinson, R., Products of the Gas-Phase Reaction of OH Radicals with Cyclohexane: Reactions of the Cyclohexoxy Radical. *J. Phys. Chem. A* **1997**, *101* (43), 8042-8048.

190. Iinuma, Y.; Böge, O.; Miao, Y.; Sierau, B.; Gnauk, T.; Herrmann, H., Laboratory studies on secondary organic aerosol formation from terpenes. *Faraday Discuss.* **2005**, *130* (0), 279-294.

191. Jonsson, Å. M.; Hallquist, M.; Ljungström, E., Influence of OH Scavenger on the Water Effect on Secondary Organic Aerosol Formation from Ozonolysis of Limonene, Δ^3-Carene, and α-Pinene. *Environ. Sci. Technol.* **2008**, *42* (16), 5938-5944.

192. Berndt, T.; Richters, S.; Jokinen, T.; Hyttinen, N.; Kurtén, T.; Otkjær, R. V.; Kjaergaard, H. G.; Stratmann, F.; Herrmann, H.; Sipilä, M.; Kulmala, M.; Ehn, M., Hydroxyl radical-induced formation of highly oxidized organic compounds. *Nat. Commun.* **2016**, *7*, 13677-13684.

193. Khan, M. A. H.; Percival, C. J.; Caravan, R. L.; Taatjes, C. A.; Shallcross, D. E., Criegee intermediates and their impacts on the troposphere. *Environ. Sci. Proc. Imp.* **2018**, *20* (3), 437-453.

194. Kidd, C.; Perraud, V.; Finlayson-Pitts, B. J., New insights into secondary organic aerosol from the ozonolysis of α-pinene from combined infrared spectroscopy and mass spectrometry measurements. *Phys. Chem. Chem. Phys.* **2014**, *16* (41), 22706-22716.

195. Grayson, J. W.; Zhang, Y.; Mutzel, A.; Renbaum-Wolff, L.; Böge, O.; Kamal, S.; Herrmann, H.; Martin, S. T.; Bertram, A. K., Effect of varying experimental conditions on the viscosity of α-pinene derived secondary organic material. *Atmos. Chem. Phys.* **2016**, *16* (10), 6027-6040.

196. Hinks, M. L.; Brady, M. V.; Lignell, H.; Song, M.; Grayson, J. W.; Bertram, A. K.; Lin, P.; Laskin, A.; Laskin, J.; Nizkorodov, S. A., Effect of viscosity on photodegradation rates in complex secondary organic aerosol materials. *Phys. Chem. Chem. Phys.* **2016**, *18* (13), 8785-8793.

197. Zhang, Y.; Sanchez, M. S.; Douet, C.; Wang, Y.; Bateman, A. P.; Gong, Z.; Kuwata, M.; Renbaum-Wolff, L.; Sato, B. B.; Liu, P. F.; Bertram, A. K.; Geiger, F. M.; Martin, S. T., Changing shapes and implied viscosities of suspended submicron particles. *Atmos. Chem. Phys.* **2015**, *15* (14), 7819-7829.

198. Petters, S. S.; Kreidenweis, S. M.; Grieshop, A. P.; Ziemann, P. J.; Petters, M. D., Temperature- and Humidity-Dependent Phase States of Secondary Organic Aerosols. *Geophys. Res. Letters* **2019**, *46* (2), 1005-1013.

199. Rocklage, J. M.; Marple, V. A.; Olson, B. A., Study of Secondary Deposits in Multiple Round Nozzle Impactors. *Aerosol. Sci. Tech.* **2013**, *47* (10), 1144-1151.

200. Aiken, A. C.; DeCarlo, P. F.; Jimenez, J. L., Elemental Analysis of Organic Species with Electron Ionization High-Resolution Mass Spectrometry. *Anal. Chem.* **2007**, *79* (21), 8350-8358.

201. Duplissy, J.; DeCarlo, P. F.; Dommen, J.; Alfarra, M. R.; Metzger, A.; Barmpadimos, I.; Prevot, A. S. H.; Weingartner, E.; Tritscher, T.; Gysel, M.; Aiken, A. C.; Jimenez, J. L.; Canagaratna, M. R.; Worsnop, D. R.; Collins, D. R.; Tomlinson, J.; Baltensperger, U., Relating hygroscopicity and composition of organic aerosol particulate matter. *Atmos. Chem. Phys.* **2011**, *11* (3), 1155-1165.

202. Zhao, Y.; Kreisberg, N. M.; Worton, D. R.; Isaacman, G.; Weber, R. J.; Liu, S.; Day, D. A.; Russell, L. M.; Markovic, M. Z.; VandenBoer, T. C.; Murphy, J. G.; Hering, S. V.; Goldstein, A. H., Insights into Secondary Organic Aerosol Formation Mechanisms from Measured Gas/Particle Partitioning of Specific Organic Tracer Compounds. *Environ. Sci. Technol.* **2013**, *47* (8), 3781-3787.

203. Shilling, J. E.; Chen, Q.; King, S. M.; Rosenoern, T.; Kroll, J. H.; Worsnop, D. R.; DeCarlo, P. F.; Aiken, A. C.; Sueper, D.; Jimenez, J. L.; Martin, S. T., Loading-dependent elemental composition of α-pinene SOA particles. *Atmos. Chem. Phys.* **2009**, *9* (3), 771-782.

204. Molteni, U.; Simon, M.; Heinritzi, M.; Hoyle, C. R.; Bernhammer, A.-K.; Bianchi, F.; Breitenlechner, M.; Brilke, S.; Dias, A.; Duplissy, J.; Frege, C.; Gordon, H.; Heyn, C.; Jokinen, T.; Kürten, A.; Lehtipalo, K.; Makhmutov, V.; Petäjä, T.; Pieber, S. M.; Praplan, A. P.; Schobesberger, S.; Steiner, G.; Stozhkov, Y.; Tomé, A.; Tröstl, J.; Wagner, A. C.; Wagner, R.; Williamson, C.; Yan, C.; Baltensperger, U.; Curtius, J.; Donahue, N. M.; Hansel, A.; Kirkby, J.; Kulmala, M.; Worsnop, D. R.; Dommen, J., Formation of Highly Oxygenated Organic Molecules from α-Pinene Ozonolysis: Chemical Characteristics, Mechanism, and Kinetic Model Development. *ACS Earth Space Chem.* **2019**, *3* (5), 873-883.

205. Jensen, L. N.; Canagaratna, M. R.; Kristensen, K.; Quéléver, L. L. J.; Rosati, B.; Teiwes, R.; Glasius, M.; Pedersen, H. B.; Ehn, M.; Bilde, M., Temperature and VOC concentration as controlling factors for chemical composition of alpha-pinene derived secondary organic aerosol. *Atmos. Chem. Phys. Discuss.* **2020**, *2020*, 1-21.

206. Gao, Y.; Hall, W. A.; Johnston, M. V., Molecular Composition of Monoterpene Secondary Organic Aerosol at Low Mass Loading. *Environ. Sci. Technol.* **2010**, *44* (20), 7897-7902.

207. Jain, S.; Fischer, K. B.; Petrucci, G. A., The Influence of Absolute Mass Loading of Secondary Organic Aerosols on Their Phase State. *Atmosphere* **2018**, *9* (4), 131.

208. Kourtchev, I.; Giorio, C.; Manninen, A.; Wilson, E.; Mahon, B.; Aalto, J.; Kajos, M.; Venables, D.; Ruuskanen, T.; Levula, J.; Loponen, M.; Connors, S.; Harris, N.; Zhao, D.; Kiendler-Scharr, A.; Mentel, T.; Rudich, Y.; Hallquist, M.; Doussin, J.-F.; Maenhaut, W.; Bäck, J.; Petäjä, T.; Wenger, J.; Kulmala, M.; Kalberer, M., Enhanced Volatile Organic Compounds emissions and organic aerosol mass increase the oligomer content of atmospheric aerosols. *Sci. Rep.* **2016**, *6* (1), 35038.

209. Song, C.; Zaveri, R. A.; Alexander, M. L.; Thornton, J. A.; Madronich, S.; Ortega, J. V.; Zelenyuk, A.; Yu, X.-Y.; Laskin, A.; Maughan, D. A., Effect of hydrophobic primary organic aerosols on secondary organic aerosol formation from ozonolysis of α-pinene. *Geophys. Res. Letters* **2007**, *34* (20).

210. Henry, K. M.; Lohaus, T.; Donahue, N. M., Organic Aerosol Yields from α-Pinene Oxidation: Bridging the Gap between First-Generation Yields and Aging Chemistry. *Environ. Sci. Technol.* **2012**, *46* (22), 12347-12354.

211. Shilling, J. E.; Chen, Q.; King, S. M.; Rosenoern, T.; Kroll, J. H.; Worsnop, D. R.; McKinney, K. A.; Martin, S. T., Particle mass yield in secondary organic aerosol formed by the dark ozonolysis of α-pinene. *Atmos. Chem. Phys.* **2008**, *8* (7), 2073-2088.

212. Ng, N. L.; Kroll, J. H.; Keywood, M. D.; Bahreini, R.; Varutbangkul, V.; Flagan, R. C.; Seinfeld, J. H.; Lee, A.; Goldstein, A. H., Contribution of First- versus Second-Generation Products to Secondary Organic Aerosols Formed in the Oxidation of Biogenic Hydrocarbons. *Environ. Sci. Technol.* **2006**, *40* (7), 2283-2297.

213. Lee, A.; Goldstein, A. H.; Keywood, M. D.; Gao, S.; Varutbangkul, V.; Bahreini, R.; Ng, N. L.; Flagan, R. C.; Seinfeld, J. H., Gas-phase products and secondary aerosol yields from the ozonolysis of ten different terpenes. *J. Geophys. Res. Atmos.* **2006**, *111* (D7).

214. Hoffmann, T.; Odum, J. R.; Bowman, F.; Collins, D.; Klockow, D.; Flagan, R. C.; Seinfeld, J. H., Formation of Organic Aerosols from the Oxidation of Biogenic Hydrocarbons. *J. Atmos. Chem.* **1997**, *26* (2), 189-222.

215. Griffin, R. J.; Cocker III, D. R.; Flagan, R. C.; Seinfeld, J. H., Organic aerosol formation from the oxidation of biogenic hydrocarbons. *J. Geophys. Res. Atmos.* **1999**, *104* (D3), 3555-3567.

216. Cocker III, D. R.; Clegg, S. L.; Flagan, R. C.; Seinfeld, J. H., The effect of water on gas–particle partitioning of secondary organic aerosol. Part I: α-pinene/ozone system. *Atmos. Environ.* **2001**, *35* (35), 6049-6072.

217. Presto, A. A.; Donahue, N. M., Investigation of α-Pinene + Ozone Secondary Organic Aerosol Formation at Low Total Aerosol Mass. *Environ. Sci. Technol.* **2006**, *40* (11), 3536-3543.

218. Docherty, K. S.; Ziemann, P. J., Effects of Stabilized Criegee Intermediate and OH Radical Scavengers on Aerosol Formation from Reactions of β-Pinene with O 3. *Aerosol. Sci. Tech.* **2003**, *37* (11), 877-891.

219. Keywood, M. D.; Kroll, J. H.; Varutbangkul, V.; Bahreini, R.; Flagan, R. C.; Seinfeld, J. H., Secondary Organic Aerosol Formation from Cyclohexene Ozonolysis: Effect of OH Scavenger and the Role of Radical Chemistry. *Environ. Sci. Technol.* **2004**, *38* (12), 3343-3350.

220. Vander Wall, A. C.; Perraud, V.; Wingen, L. M.; Finlayson-Pitts, B. J., Evidence for a kinetically controlled burying mechanism for growth of high viscosity secondary organic aerosol. *Environ. Sci. Proc. Imp.* **2020**, *22* (1), 66-83.

221. Dahneke, B., The capture of aerosol particles by surfaces. *J. Colloid Interf. Sci.* **1971**, *37* (2), 342-353.

222. Claflin, M. S.; Krechmer, J. E.; Hu, W.; Jimenez, J. L.; Ziemann, P. J., Functional Group Composition of Secondary Organic Aerosol Formed from Ozonolysis of α-Pinene Under High VOC and Autoxidation Conditions. *ACS Earth Space Chem.* **2018**, *2* (11), 1196-1210.

223. Kolesar, K. R.; Chen, C.; Johnson, D.; Cappa, C. D., The influences of mass loading and rapid dilution of secondary organic aerosol on particle volatility. *Atmos. Chem. Phys.* **2015**, *15* (16), 9327-9343.